A STUDY OF THE MECHANICAL DESIGN AND GEAR TOOTH ROOT STRAINS IN FLEXIBLE PIN, MULTI-STAGE, PLANETARY WIND TURBINE GEAR TRAINS USING THREE DIMENSIONAL FINITE ELEMENT/CONTACT MECHANICS MODELS AND EXPERIMENTS

A Thesis

Presented in Partial Fulfillment of the Requirements for the Degree Master of Science in the Graduate School of The Ohio State University

By

Phillip E. Prueter, B.S.

Graduate Program in Mechanical Engineering

The Ohio State University

2011

Master's Examination Committee:

Dr. Robert Parker, Advisor

Dr. Sandeep Vijayakar

Abstract

Wind energy has received a great deal of attention in recent years in part due to its minimal environmental impact and improving efficiency. Increasingly complex wind turbine gear train designs, well-known rolling element bearing failures, and the constant push to manufacture more reliable, longer lasting gear trains generate the need for more advanced analysis techniques. The objectives of this thesis are to examine the mechanical design of Orbital2 flexible pin, multi-stage planetary wind turbine gear trains using three dimensional finite element/contact mechanics models. These models are constructed and analyzed using software that specializes in elastic gear tooth contact. Computational results, such as gear tooth root strain, are compared to full system experiments. Root strain is calculated at multiple locations across the facewidth of ring gears from the computational models and compared to experimental data. Computational results for tooth load distribution and planet load sharing factor are compared to experiments. The computational models consider gear misalignment and carrier eccentricity and permit design recommendations for improving tooth load distribution and planet load sharing.

To my parents, Bill and Nancy, and my fiancée, Sara. Thank you for all your love, encouragement, and support.

Acknowledgments

I would like to thank my advisor, Dr. Robert G. Parker, and Dr. Sandeep Vijayakar of Advanced Numerical Solutions Inc. for their guidance, patience, and support. Dr. Vijayakar is also acknowledged for granting access to the Transmission3D software package. I would also like to thank Orbital2 Ltd. for funding the research related to the wind turbine gear trains examined herein. I would like to recognize Dr. Frank Cunliffe, Mr. Remko Gerbenzon, and Mr. Vilem Rosko of Orbital2 for providing the necessary system parameters and for their suggestions pertaining to the finite element modeling and comparisons discussed in this thesis.

Vita

November 08, 1986 ..... Born - Canton, Ohio, U.S.A.

May 2009 ..... B.S. Mechanical Engineering, Summa Cum Laude, The University of Akron

2009-present ..... Graduate Research Fellow, Dynamics and Vibrations Laboratory, The Ohio State University

Fields of Study

Major Field: Mechanical Engineering

Studies in Applied Mechanics, Dynamics, and Vibrations: Prof. Robert Parker

Table of Contents

List of Tables

List of Figures

Figure **Page**

Chapter 1: INTRODUCTION

1.1 Motivation

Gears are critical components used in a variety of mechanical systems in many different industries. Gears can be found in the aerospace, energy, steel, mining, marine, petroleum, and automotive industries among others. In all of the industries that gears are used, there is a constant push to achieve higher reliability and improve existing gear train designs. In fact, in many applications, the cost of one day's lost production due to gear train malfunction far exceeds the initial cost of the unit [1]. The constant drive for improved quality and efficiency of gear trains has generated the need for more sophisticated computational tools, capable of analyzing complex systems while accurately capturing the contact mechanics associated with gears. Such computational techniques will be discussed in herein.

The main function of a gear train is to transmit rotational motion from a driving prime mover to a driven machine. The input and output ends of the gear train may operate at different speeds. If this is the case, a speed-increasing or speed-decreasing gear train unit is required. These configurations allow both machines on either end of the gear train to operate at their most efficient speeds [1]. For a given application, the gear train configuration chosen depends on physical arrangement of machinery, space

and weight limitations, the speed ratio between input and output shafts, efficiency, the physical environment, and torque loading. The geometrical relationship between the input and output shafts plays a key role in determining the physical arrangement of the gear train. Some examples of shaft configurations are concentric, parallel offset, right angle, or skewed. The amount of speed increase or reduction of a gear train can play an important role in overall gear train design. For a simple gear pair, this ratio is simply the ratio of the pitch diameter of the larger gear to the smaller gear or the ratio of the number of teeth on the larger gear to the smaller gear. For high ratios, there can be size, stress, and geometrical limitations, making simple gear pairs impractical.

An efficient way to achieve high reduction ratios and limit the size and weight of a gear train is to use a planetary gear configuration. A planetary gear train transmits power through multiple load paths in a compact space. A typical planetary gear system consists of a sun gear having external teeth, planet gears having external teeth, a ring gear having internal teeth, and a planet carrier. In a planetary system, the carrier rotates about the center of the system. A point on a planet gear not only rotates about the planet axis but also about the center of the system. This type of configuration is also known as an epicyclic gear system [1]. Planetary gear systems can achieve high reduction ratios and offer significant envelope and weight savings. They can provide several other advantages such as load sharing between multiple mesh points, smaller bearing loads, and smaller, stiffer components that can lead to reduced noise and vibration. Planetary gear systems are utilized in helicopters, wind turbines, aircraft engines, automobiles, heavy machinery, and a variety of other applications.

The wind turbine gear trains examined in this thesis are Orbital2 flexible pin, multi-stage, planetary configurations. Multi-stage, planetary gear trains can achieve very large speed ratios in a compact space. In wind turbine applications, the main rotor shaft that is attached to the wind turbine blades is the low-speed end and the output shaft that connects to the generator is the high-speed end. Design considerations and analysis techniques for these wind turbine gear trains will be examined using computational and experimental results.

The use of wind turbines to generate electricity worldwide has become more common in recent years due to the rising costs associated with more traditional methods of power generation such as fossil fuels. Unlike burning fossil fuels to generate electricity, wind turbines emit no greenhouse gases and therefore have a more positive environmental impact. In the United States, every megawatt-hour of wind energy that is not produced by a conventional energy source reduces greenhouse gas emissions by an equivalent of 0.558 tons of carbon dioxide [2]. In terms of cost, wind energy is comparable to fossil fuel based energy, when the cost of greenhouse gas emissions is taken into consideration [2]. Currently, the wind turbines that make up the majority of the generating capacity worldwide fall in the range of 1.5 to 5 MW [3]. The wind turbine gear trains examined herein fall in this range. According to the 2010 World Wind Energy Report [4], the worldwide capacity of wind turbines exceeded 196,000 MW and showed a growth rate of 23.6 percent in 2010. According to the same report, the wind energy industry employed about 670,000 people worldwide in 2010. Due to accelerated development and improved policies, the World Wind Energy Association predicts that global wind energy capacity could reach 1,500,000 MW by 2020 [4]. As

the use of wind energy grows worldwide, there will be a constant push to design more reliable and efficient wind turbine components.

There are a number of challenges associated with the design and successful operation of wind powered generators. One of the main challenges when designing wind turbines is accounting for variable wind velocity which can impose severe cyclic loads on turbine blades and other system components [5]. These cyclic loads can create fatigue problems in moving components such as rolling element bearings and gears, making a reliable design of these components essential. The torque level in a wind turbine gear train will vary between zero and rated torque according to the wind speed. Gear teeth in wind turbine applications must be designed in fatigue to achieve both acceptable contact stresses on the flanks and acceptable bending stresses in the roots [6].

In addition to cyclic loading, another obstacle to overcome when designing wind turbine drive trains is noise. The main source of gear train noise comes from the meshing of individual gear teeth. When a gear tooth meshes with another tooth, it deflects causing unloaded teeth to be misaligned when they come into contact. Even if gear teeth are accurately machined, this bending creates an interference at the first point of contact [7]. One way to compensate for this interference and to reduce gear train noise during operation is to adjust tooth profiles by removing material. Tooth modifications such as tip and lead relief are commonly used to improve tooth contact patterns and bring unloaded teeth back into alignment [6]. For wind turbine applications, tooth modifications must be carefully selected because of variable gear loading. The finite element/contact mechanics software used to examine the wind turbine gear trains studied herein can accurately model tooth micro-geometry such

as tip and lead modifications. Accurately modeling detailed tooth micro-geometry is essential when attempting to correlate tooth root strain to full system experiments.

1.2 Literature Review

Analyzing planetary gear systems using computational models presents a unique challenge. Previous work has utilized computational models to examine stresses, strains, and deformations in planetary gears. One of the first attempts to use a non-linear finite element model to study the behavior of a planetary gear system under static loading was performed by Valco [8]. Kahraman et al. [9] studied the influence of rim thickness of ring gears and compared experimental strain from the roots of ring gear teeth to a two dimensional finite element model. In this comparison, predicted strain shapes matched measured ones closely but the amplitudes differed for certain ring gear thicknesses. It was determined that a two dimensional model can capture ring deflections and hoop stresses while accurate quantification of root strain amplitudes might require a three dimensional model.

Singh et al. [10] examined load sharing in planetary transmissions by comparing root strains from a three dimensional finite element model to experimental results. Strain from the computational model was compared to experiments at multiple circumferential locations on the ring, and the shapes and magnitudes of strain peaks matched well. Root strain, however, was only compared at one location across the facewidth of the ring, making it impossible to detect changes in load distribution due to planet tilting, lead errors, and misalignments. Ligata et al. [11] also used experimental root strain from a ring gear to investigate the influence of manufacturing errors

on planetary gear stresses and planet load sharing. Cheon and Parker [12, 13] examined the influence of manufacturing errors on dynamic characteristics, load sharing, and critical tooth stresses in planetary gears using computational models. James and Harris [14] predicted unequal load sharing in planetary gears due to manufacturing errors using numerical simulations and validated results against experiments.

Several others studies have used finite element models of planetary gears to investigate manufacturing errors, influence of rim thickness, planet load sharing, and dynamic response. Singh [15] used a three dimensional finite element model of a planetary transmission to study load sharing behavior of planets. Kahraman and Vijayakar [16] examined a two dimensional finite element model of a planetary gear set to determine the effect of internal gear flexibility on deflections and tooth bending stresses. Bodas and Kahraman [17] examined the influence of carrier and gear manufacturing errors on planetary gear sets using a two dimensional finite element model. Parker et al. [18] used a two dimensional finite element model of a planetary gear system to investigate dynamic response. All of these studies used the finite element and contact analysis software program Calyx to model the planetary gear systems investigated. In this study, Calyx is used to analyze full, three dimensional gear trains. The modeling capabilities of Calyx will be discussed in more detail in Chapter 2.

Currently, the literature on the design and analysis of wind turbine gear trains is limited, but research in this area has increased in recent years. In 2003, the National Renewable Energy Laboratory's Wind Partnership for Advanced Component Technologies published findings from a study [19] that identified possible drive train technology improvements to make wind energy a more desirable energy source. Smolders et al. [20] examined reliability analysis models of wind turbine gear trains and

estimated failure rates of critical components. Musial et al. [21] investigated design deficiencies in wind turbine gear trains and concluded that more advanced design techniques are required to accelerate the development of more robust gear train designs. Other studies [22–24] have also addressed gear train reliability issues in wind turbines and have proposed possible solutions for implementation of next-generation technology to improve overall gear train design.

In recent years, the push to develop more reliable wind turbine gear train designs has compelled researchers to investigate more advanced drive train analysis techniques and to develop improved capabilities to conduct full system experiments. Peeters and Vandepitte [25] compared different analytical multi-body modeling techniques for a three stage planetary wind turbine gear train. In a recent study, Helsen at al. [26] investigated multi-body modeling techniques for describing modal behavior of wind turbine gear trains. In this study, analytical and experimental results are discussed. Musial and McNiff [27] discussed the capabilities of a 2.5 MW dynamometer facility at the National Wind Technology Center and how this testing tool will contribute to the maturation of wind turbine gear train design. Helsen et al. [28] examined advanced modeling techniques of wind turbine gear trains and validated results using measurements performed on a 13.2 MW test rig. Both full system experiments and advanced computational models are examined and compared for the gear trains discussed in this thesis. As the use of wind energy increases worldwide, there will be increased demand to use advanced experimental and computational techniques to understand and improve the design and reliability of wind turbine gear drive systems.

1.3 Objectives and Scope

The overall objective of this thesis is to compare the behavior of Orbital2 flexible pin, multi-stage, planetary wind turbine gear trains, using complete three dimensional finite element/contact mechanics models and experimental measurements. The complex design of these gear trains provides an excellent opportunity to validate the sophisticated finite element/contact mechanics software utilized in this study by comparing computational results to experimental data. The advantage of complete computational models that can accurately capture the contact mechanics associated with gear problems is that they can be used to study the behavior of complex systems and examine different designs of gear train components. Looking at different designs of components leads to a better understanding of how a gear train deforms under load and provides insight into how to improve load distribution across the ring gear facewidths among other design considerations. Computational models, such as the ones discussed in this thesis, are extremely valuable design tools when attempting to understand and improve complex gear train designs such as the ones examined herein.

The wind turbine gear trains examined in this thesis are a great deal larger than the ones examined in references [8–18]. The finite element/contact mechanics models used incorporate multiple planetary stages, a finite element housing, finite element carriers, and flexible pins at the planet-carrier connections. Root strain from the computational models is compared to experimental root strain at different strain gauge locations across the facewidth of ring gears. The advantage of extracting strain from multiple locations across the ring facewidth is that it can provide information about load distribution across the ring tooth during a planet pass. Experimental root

strain from certain locations indicate an uneven load distribution across the tooth facewidth, with the ring teeth being loaded more towards the constrained end of the ring and loaded less towards the free end of the ring when a planet tooth meshes with the instrumented ring tooth. Root strain from complete, three dimensional finite element/contact mechanics models will be examined and compared to full system experiments for each gear train. Computational results for tooth load distribution and planet load sharing factor are compared to experiments. Methods to improve tooth load distribution across gear facewidths and other design considerations will be discussed.

Chapter 2: FINITE ELEMENT/CONTACT MECHANICS SOFTWARE

2.1 Software Modules

The software analysis package used to analyze the gear trains studied in this thesis is Transmission3D, developed by Advanced Numerical Solutions. This software package consists of the Calyx, Multyx, and Guide programs as shown in Figure 2.1. Calyx is the contact analysis code capable of analyzing a variety of two and three dimensional contact problems. Multyx communicates with Calyx through a menu-based interface and translates user commands into the appropriate programming language statements that Calyx requires. Multyx also has pre and post-processing software called Iglass that extracts analysis results from Calyx. Model deflections, stress contours, and contact patterns can be viewed using Iglass. The Guide program simply provides a graphical user interface to Multyx. Guide is convenient for building large finite element/contact mechanics models and it improves user friendliness, but it is not required to carry out an analysis. A model can be built and analyzed using the Multyx command line interface [29]. The capabilities of Calyx make it well suited to solve the complex systems examined herein.

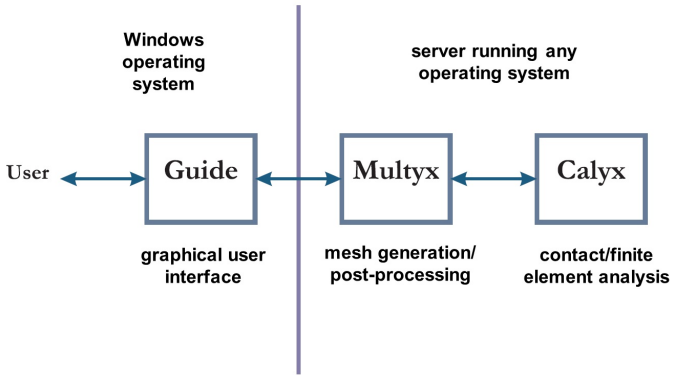

Figure 2.1: Illustration of the software modules in the Transmission3D analysis package [29].

A thorough description of the finite element/contact mechanics model parameters that are defined in Multyx menus in the Guide user interface is given in Appendix E. Navigating these menus is essential in order to efficiently construct large, three dimensional models such as the ones examined in this thesis.

2.2 Contact Solver and Program Methodology

Accurately simulating gear tooth contact is complicated. One of the main reasons is that the contact regions on gear teeth are significantly smaller than the other dimensions of the gear bodies. The width of the contact zones in typical gearing applications is generally two orders of magnitude smaller than the dimensions of the gear teeth themselves [29]. Conventional finite element techniques require highly refined meshes near the contact regions. As the gears move according to their prescribed kinematic motion, the contact location moves along the profile of the tooth. This means that conventional finite element models require a fine mesh over entire tooth

surfaces or the finite element model must be re-meshed for each gear configuration. As discussed in [15], neither of these options present an efficient way to simulate contact in gear systems, especially for planetary configurations with multiple teeth in contact and multiple active meshes. Calyx overcomes this obstacle by making the contact model independent of the finite element model. This unique approach was specifically developed to efficiently analyze the mechanics of precisely machined, contacting elastic bodies such as gears [29]. Figure 2.2(a) shows the instantaneous contact pressure on a planet tooth from the finite element model of the Orbital2 W3600 gear train. The contact grid consists of segments in the profile and facewidth directions (partially visible in the discretized contact pattern in Figure 2.2(a) and depicted in Figure 2.2(b)) that are independent of the finite element mesh. The number of divisions in the profile and facewidth directions is a user input in the finite element software. In the Guide user interface, contact parameters are defined in the pairs menu (shown in Figure E.4 in Appendix E).

What sets this approach apart from conventional finite element packages is that it uses semi-analytical techniques to compute relative deformations and stresses for points near the contact region while the finite element model is used to compute deformations and stresses outside of the contact regions. The semi-analytical solution is the surface integral form of the Bousinesq solution for a point load on an elastic half-space. The finite element solution and semi-analytical solution are combined by using a matching interface embedded in the contacting body [31]. Load distributions and rigid body movements are calculated using the simplex method that is discussed further in [32]. Poor contact convergence at interfaces is a recurring problem when using general non-linear solvers utilized by conventional finite element software. The

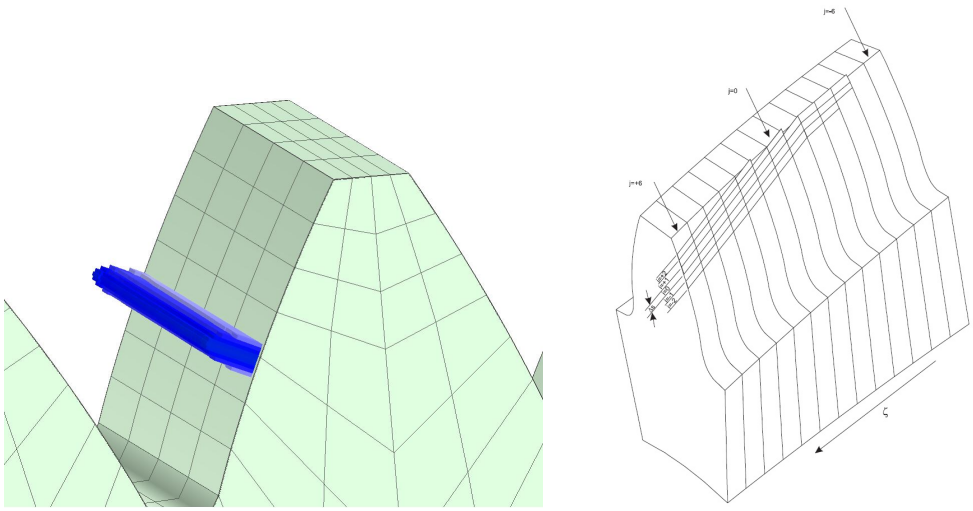

(a) (b)

Figure 2.2: (a) Instantaneous contact pressure on a planet tooth from the Orbital2 W3600 finite element model under constant torque, and (b) Computational contact grid [30].

simplex solver used in Calyx overcomes this by guaranteeing convergence within a predetermined number of iterations and can detect ill-posed contact problems before the contact solver solution process is initiated. Constraints imposed by contact between matching surfaces are treated as linear inequality constraints [29].

When running an analysis, choosing the correct contact parameters such as the number of contact cells in the facewidth (NFACEDIVS) and profile (NPROFDIVS) directions and the dimension of each grid cell in the profile direction (DSPROF) requires careful consideration. These parameters are specified in the pairs menu where two meshing gear bodies are selected. The entire facewidth of the tooth is divided into $2F + 1$ slices, where F is the user selectable quantity NFACEDIVS. ζ is a parameter (not user selectable) that defines the location across the facewidth of a tooth and ranges from -1 on one edge of the tooth to +1 on the other edge.

Therefore, the thickness of each contact grid cell in the ζ parameter space in the facewidth direction ($\Delta\zeta$) is given as [29]

$$\Delta\zeta = \frac{2}{(2F+1)}. \tag{2.1}$$

A cross section of each tooth is taken at the middle of each contact grid cell. A point is located on each cell (using the undeformed tooth geometry) that approaches the surface of the matching tooth (on the second gear body defined in the pairs menu). If the separation between the two gears at this point is larger than the user defined separation tolerance (SEPTOL), the entire contact cell is eliminated from consideration during the contact calculation. The dimension of the contact cell in the profile direction (Δs) is a user defined quantity DSPROF. s is measured along the tooth profile. The entire width of the contact grid in the profile direction (W) is given as [29]

$$W = \Delta s(2P+1), \tag{2.2}$$

where P represents the the number of contact grid cells in the profile direction. This quantity is user selectable in Calyx and is referred to as NPROFDIVS.

The width of the contact grid in the profile direction must be correctly specified to ensure a parabolic pressure distribution as seen in Figure 2.2(a). Figures 2.3(a), 2.3(b), and 2.3(c) show the contact pressure distribution across the width of contact in the profile direction for a contact grid that is too wide, too narrow, and correct, respectively. Contact parameters must be adjusted for each defined contact pair between

meshing gear teeth for a given torque to achieve an appropriate pressure distribution. A grid that is too wide results in loss of resolution because the center grid cell carries all of the load (Figure 2.3(a)). A grid that is too narrow can cause artificially high high contact pressures at the edge of the grid (Figure 2.3(b)). The number of contact cells in the facewidth direction must be carefully considered also, especially when variations in strain characteristics across a tooth are being examined.

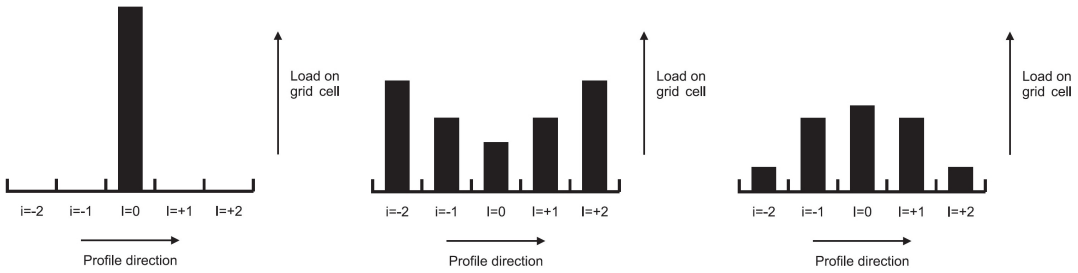

Figure 2.3: Contact pressure distribution across the width of contact in the profile direction when the contact grid is: (a) too wide [30], (b) too narrow [30], and (c) correct [30].

Calyx calculates system displacements by assuming a linear system of equations that represent the motion of each structure. The following summary of the contact analysis utilized by Calyx is outlined by Parker, Vijayakar, and Imajo [33]. Equation (2.3), as discussed in [30, 33], gives this system of equations

$$\mathbf{M}\ddot{\mathbf{x}} + \mathbf{C}\dot{\mathbf{x}} + \mathbf{K}\mathbf{x} = \mathbf{f}, \tag{2.3}$$

where $\mathbf{x}$ is a vector of the system degrees of freedom, $\mathbf{f}$ is a vector of externally applied loads, and $\mathbf{M}$, $\mathbf{C}$, and $\mathbf{K}$ are the structure mass, damping, and stiffness matrix, respectively. All of the analyses discussed herein are static analyses. In this case the terms with time derivatives and inertial loads are ignored and the equations of motion shown in Equation (2.3) take the form given in Equation (2.4), as shown in [30, 33].

$$\mathbf{K}\mathbf{x} = \mathbf{f} \tag{2.4}$$

In order to diagonalize the system given in Equation (2.4) and separate out the non-singular part, a linear coordinate transformation is used as discussed in [33] conforming to

$$\mathbf{x} = \begin{bmatrix}\mathbf{T}_\phi & \mathbf{T}_\theta\end{bmatrix} \begin{Bmatrix}\mathbf{q}_\phi \\ \mathbf{q}_\theta\end{Bmatrix} = \mathbf{T} \begin{Bmatrix}\mathbf{g}_\phi \\ \mathbf{g}_\theta\end{Bmatrix} \tag{2.5}$$

$$\mathbf{T}^\mathbf{T}\mathbf{f} = \begin{bmatrix}\mathbf{T}_\phi^\mathbf{T} \\ \mathbf{T}_\theta^\mathbf{T}\end{bmatrix} \mathbf{f} = \begin{Bmatrix}\mathbf{g}_\phi \\ \mathbf{g}_\theta\end{Bmatrix} \tag{2.6}$$

$$\mathbf{T}^\mathbf{T}\mathbf{K}\mathbf{T} \begin{Bmatrix}\mathbf{q}_\phi \\ \mathbf{q}_\theta\end{Bmatrix} = \begin{pmatrix}\mathbf{K}_{\phi\phi} & \mathbf{0} \\ \mathbf{0} & \mathbf{0}\end{pmatrix} \begin{Bmatrix}\mathbf{q}_\phi \\ \mathbf{q}_\theta\end{Bmatrix} = \begin{Bmatrix}\mathbf{g}_\phi \\ \mathbf{g}_\theta\end{Bmatrix}, \tag{2.7}$$

where the columns of $\mathbf{T}$ consist of the eigenvectors of the stiffness matrix ($\mathbf{K}$), $\mathbf{q}_\phi$ represents elastic modes, and $\mathbf{q}_\theta$ represents rigid-body modes. $\mathbf{K}_{\phi\phi}$ is positive-definite and diagonal.

The contact analysis involves calculating candidate contact pairs with surface normals along a common axis as described in [33]. These pairs are determined using a search algorithm and a defined tolerance. The tooth surface is defined as a continuous curve or a set of surface coordinates with a designated surface normal. The number of points used to define this surface govern the potential candidate contact points. The final separation of candidate contact pairs in the deformed state ($\mathbf{d}$) is calculated along their common normal direction by

$$\mathbf{d} = \hat{\epsilon} + \delta, \tag{2.8}$$

where $\hat{\epsilon}$ is the separation distance of all candidate contact pairs along their common normal direction in the undeformed state and δ represents the changes in separation due to loading. In order to relate the vector of external loads ($\mathbf{f}$) given in Equation (2.4) to the contact force, a compressive contact load vector acting along the normals of the candidate contact pairs is defined as $\mathbf{p}$. $\mathbf{f}$ and $\mathbf{p}$ are related by

$$\mathbf{f} = \mathbf{E}\mathbf{p} + \mathbf{f_o}, \tag{2.9}$$

where $\mathbf{E}$ is a non-square matrix that allocates the contact force ($\mathbf{p}$) at the candidate contact points as nodal forces and the vector $\mathbf{f_o}$ contains externally applied loads acting on the system that are not due to contact. The matrix $\mathbf{E}$ is dependent on tooth geometry and the finite element interpolation functions. The increase in separation due to loading, δ, is defined as

$$\delta = \mathbf{G}\begin{bmatrix}\mathbf{T}_\phi & \mathbf{T}_\theta\end{bmatrix}\begin{Bmatrix}\mathbf{q}_\phi \\ \mathbf{q}_\theta\end{Bmatrix} = \mathbf{G}\mathbf{x}, \tag{2.10}$$

where $\mathbf{G}$ is dependent on tooth geometry and finite element interpolation functions and $\mathbf{x}$ is the displacement vector given in Equation (2.4). δ shown in Equation (2.10) gives the increase in separation at contact points due to the finite element model that is outside of the contact region. Local deformation from within the contact region is determined using the semi-analytical surface integral finite element solution and adds a term ($\mathbf{A_{local}p}$) into Equation (2.10) [18, 31, 33]. From the partitions of Equation (2.7) and Equations (2.8) and (2.9), the final separation of candidate contact points takes the form

$$\begin{aligned}\mathbf{d} &= (\mathbf{G}\mathbf{T}_\phi\mathbf{K}_{\phi\phi}^{-\mathbf{1}}\mathbf{T}_\phi^{\mathbf{T}}\mathbf{E} + \mathbf{A_{local}})\mathbf{p} + (\mathbf{G}\mathbf{T}_\theta)\mathbf{q}_\theta + (\hat{\epsilon} + \mathbf{G}\mathbf{T}_\phi\mathbf{K}_{\phi\phi}^{-\mathbf{1}}\mathbf{T}_\phi^{\mathbf{T}}\mathbf{f_o}) \\ &= \mathbf{A}\mathbf{p} + \mathbf{C}\mathbf{q}_\theta + \epsilon. \end{aligned} \tag{2.11}$$

Furthermore, Equations (2.7) and (2.9) can be combined to yield the equilibrium equation

$$\begin{aligned}\mathbf{T}_\theta^{\mathbf{T}}\mathbf{E}\mathbf{p} &= -\mathbf{T}_\theta^{\mathbf{T}}\mathbf{f_o} \\ \mathbf{B}\mathbf{p} &= \lambda. \end{aligned} \tag{2.12}$$

The contact problem can now be evaluated by solving Equations (2.11) and (2.12) for $\mathbf{d}$, $\mathbf{p}$, and $\mathbf{q}_\theta$ subject to the components d_i and p_i being ≥ 0 and either d_i or p_i

$= 0$ for every i. The requirement that the components of the final separation ($\mathbf{d}$) and compressive load ($\mathbf{p}$) vectors between contact pairs be ≥ 0 infers that separation between teeth must not be negative (implies penetration of one tooth surface into its matching pair is prohibited) and ensures that the contact force never be tension. Furthermore, the requirement that either the components of $\mathbf{d}$ or $\mathbf{p} = 0$ means that if the separation between contact pairs is zero then there is compression or if the compression is zero, then the separation between contact pairs is a positive value.

This posed problem is solved using the simplex method as discussed in [32]. These results are used in Equations (2.5), (2.6), (2.7), and (2.9) to calculate the displacement vector $\mathbf{x}$. The values of $\mathbf{p}$ are used in the surface integral/finite element solution to determine tooth stresses and deflections near the contact region [33]. $\mathbf{A_{local}}$, $\mathbf{E}$, and $\mathbf{G}$ are dependent on prescribed system kinematics and the changing contact conditions as the gears move and are therefore recalculated for each time step. $\mathbf{K}$ and $\mathbf{T}$ are not dependent on system kinematics and are calculated once at the beginning of a simulation.

In gear systems with multiple active tooth meshes such as planetary configurations, there are many rigid body degrees of freedom that are constrained only by the contact conditions. Many conventional finite element programs experience singular stiffness matrices and can break down due to these rigid body motions. Calyx deals with this by attaching a reference frame to individual components. Finite element computations are performed for each component in its reference frame. Stiffness matrices will be well conditioned given that each component is sufficiently constrained to its own reference frame. Nominal component positions are determined by the kinematics of the system. Typical gear train systems also have a large number of

total degrees of freedom which, in general, is approximately proportional to the total number of teeth [29]. A conventional finite element analysis of a system with many degrees of freedom requires a large amount of computer resources and the simulation time could easily become impractical. Calyx uses a hierarchical approach in which a system is constructed using many substructures composed of multiple subsequent substructures. Stiffness matrix decomposition and load vector back-substitution effectively utilizes this substructure hierarchy and ensures that computer requirements remain within practical limits, even for large, multi-mesh systems [29].

In Calyx, each component that is rigidly attached to a reference frame is referred to as a body. Each body is capable of rigid body motion and interacts with other bodies through defined surface contact and bearing connections. For example, in a planetary gear train, the sun gear, the planets, and the ring gear are treated as separate bodies. The ground is considered to be a fixed body. Figure 2.4(a) shows an example of a multi-body system. The reference frame that is rigidly attached to each body has six degrees of freedom. There are three translation components U_x, U_y, and U_z, and three rotational components θ_x, θ_y, and θ_z as shown in Figure 2.4(b). The ground reference frame is fixed and does not move.

2.3 Mesh Generation

When meshing gear bodies in Transmission3D, it is not necessary for the user to define nodal coordinates or element connectivity information. Gear tooth meshes are generated using defined gear geometry and preprogrammed mesh template files. The two mesh template files used in the analyses contained in this thesis are the medium (Figure 2.5(a)) and fine root (Figure 2.5(b)) template files. The fine root template

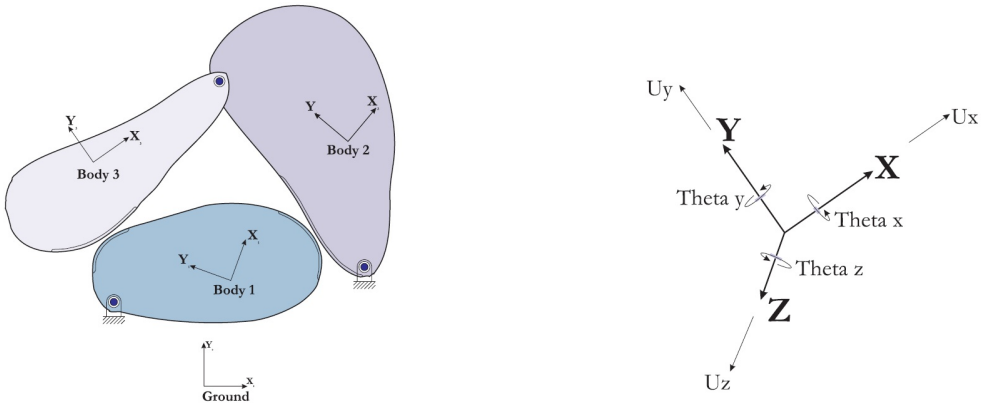

(a) (b)

Figure 2.4: (a) Example of a multi-body system in Calyx [29], and (b) Reference frame with corresponding degrees of freedom [29].

file is used for the ring gear teeth of the planetary stages in each gear train. The medium template file is used for all other teeth. A more refined ring tooth improves the accuracy of the root strain calculation. For all gears, four elements are used across the gear tooth facewidth. The surface profile coordinate, s, ranges from 0 to 48 on each tooth contact surface as shown in Figures 2.5(a) and 2.5(b). The surface facewidth coordinate, ζ, ranges from -1 at the tooth edge to 1 at the other tooth edge. These parameters are used to define the location of tooth strain gauges. The mesh template file used for a given gear is specified at the bottom of the tooth menu in Guide as shown in Appendix E.

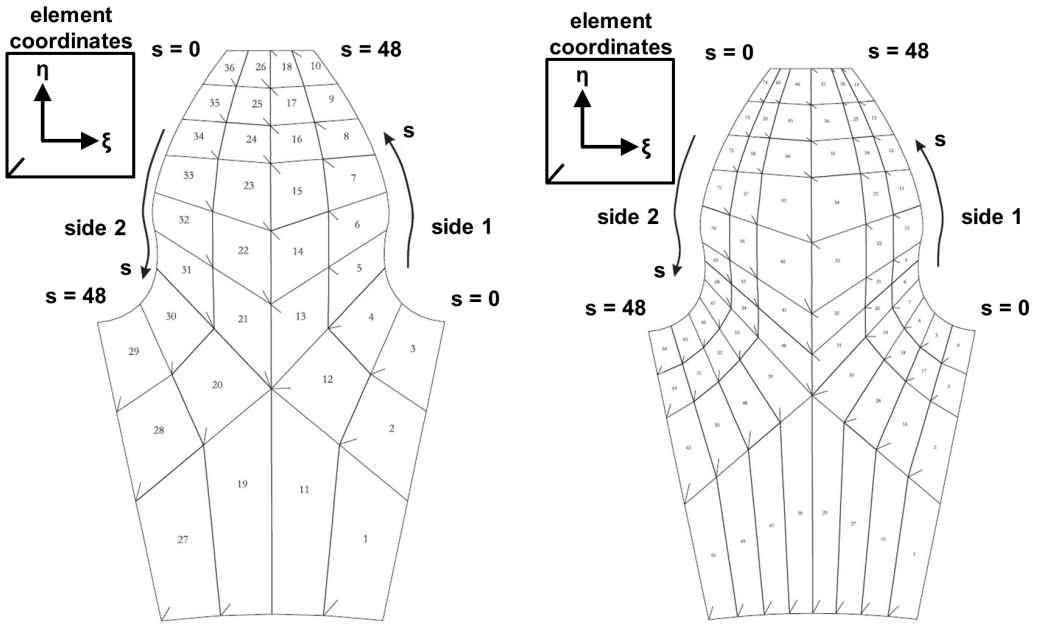

(a) (b)

Figure 2.5: Element numbering scheme, orientation, and contact surface profile coordinates for: (a) medium mesh template file (MEDIUM.TPL) [29], and (b) fine root mesh template file (FINEROOT.TPL) [29].

The location of internally and externally meshed gear bodies relative to their rotor origins is shown in Figures 2.6(a) and 2.6(b), respectively. The defined axial location of a gear corresponds to the center of its facewidth along the rotor axis relative to the rotor origin. Other gear parameters required to construct a gear are the number of teeth, number of face elements, module, pressure angle, tooth thickness, facewidth, helix angle, whether the gear is left or right handed, inner diameter, outer diameter, root diameter, material properties, and root radius or rack tip radius for ring or sun gears, respectively. The base of the teeth are connected to either a rim or a shaft using displacement interpolation. This will be discussed in depth later in this chapter.

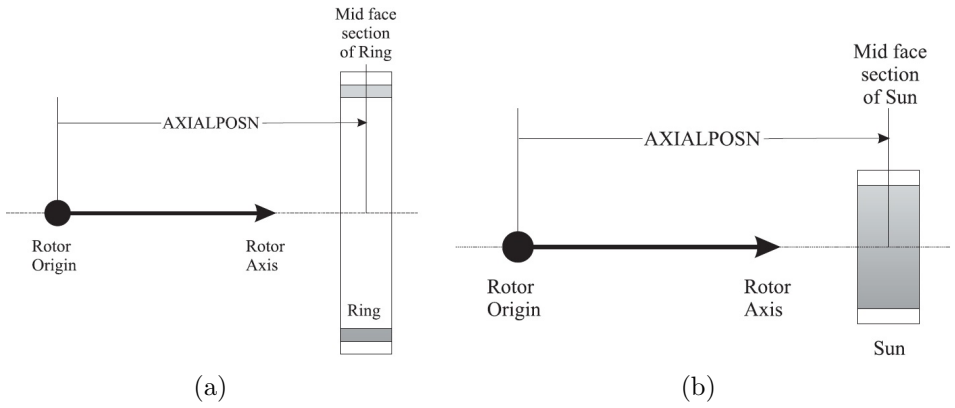

Figure 2.6: (a) Position of a ring gear relative to its rotor origin in Calyx [29], and (b) position of a sun gear relative to its rotor origin in Calyx [29].

Shaft and complex pin meshes are automatically generated in Transmission3D by defining their location relative to the rotor origin and their geometry including number of segments, segment length, and inner and outer diameter surface definitions (cylindrical or conical). An example of a shaft constructed in Calyx is shown in Figure 2.7. The only other user inputs when constructing shafts are Fourier surface definitions or constraints on the inner or outer surfaces of each segment, material properties, and the number of elements in the axial, radial, and circumferential directions. At least one shaft segment in each rotor must have a constrained surface to connect that rotor to its reference frame. Reference frame reaction forces and moments flow to the shaft through the defined constraint. The shaft and shaft segment menus are discussed in Appendix E.

More complicated geometries such as housings, drive flanges, and planet carriers are externally meshed using a conventional finite element software package. The

file generated from a conventional finite element program containing nodal coordinates, material properties, and element connectivity can then be converted to Calyx mesh files and implemented into the Transmission3D model. All externally meshed components included in the gear trains discussed herein were meshed using MSC Patran. These parts were meshed using ten-noded tetrahedral elements and converted to Calyx mesh files using the CVTBDF program.

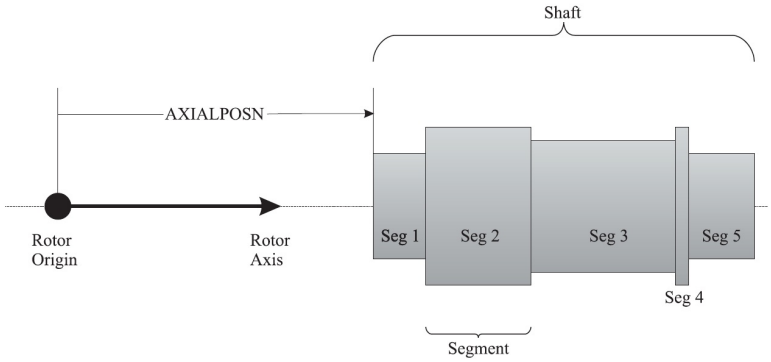

Figure 2.7: Construction of a shaft with five segments and location relative to the rotor origin in Calyx [29].

2.4 Displacement Interpolation and Connectors

Calyx connects finite element parts with dissimilar nodal distributions at their interface using Fourier surfaces. These Fourier surfaces enforce displacement continuity through trigonometric and polynomial series expansions. In the circular direction a Fourier Series (trigonometric series) is used. In the radial and axial directions polynomial series are used. The displacement at an interface is expanded as

$$u(\theta, z) = \sum_{m=0}^{M} z^m \left[u_{m0} + \sum_{n=1}^{N} (u_{cmn} cosn\theta + u_{smn} sinn\theta) \right], \tag{2.13}$$

where θ is the circular direction, z is the axial direction, M is the axial order, and N is the circular order. M and N should not exceed the support provided by the underlying degrees of freedom.

Fourier surfaces are used to attach gear rims to the tooth base and externally meshed parts to shafts and gears. Certain interfaces require higher order interpolations (M,N) to accurately calculate deformations. For example, in the gear trains examined herein, the interface between the outer diameter of the ring tooth and the inner diameter of the ring rim is defined using a Fourier surface. In order to accurately capture ring deflections, each of these surfaces is defined using an axial order of four and a circular order of 64. Using a lower order surface at this interface results in inaccurate shapes of root strain signals (the slow transient in strain related to each passing planet does not fit the experimental strain signals). When converting externally meshed components to Calyx mesh files using the CVTBDF program, Fourier surface definitions are specified at locations where the externally meshed component connects with internally meshed shafts or bearing races.

Fourier surfaces are also defined where inner and outer races of bearings connect to shafts or gear rims. Each race is treated as a rigid body with the six degrees of freedom shown in Figure 2.4(b). In the analyses discussed in this thesis, the six degrees of freedom of the first bearing race interact with the six degrees of freedom of the second bearing race through a defined stiffness matrix. Figure 2.8(a) shows bearing reference frames corresponding to the inner and outer races. Figure 2.8(b) depicts

how bearing deformations are defined in Calyx. Bearing displacements are of race-one relative to race-two, in the race-two reference frame. The location, orientation, length, and diameter of inner and outer bearing races are defined in the connector menu in Multyx (shown in Figure E.5 given in Appendix E). These reference frames become important when applying unloaded bearing deformation. This will be discussed later in this thesis when examining system eccentricities. Approximate stiffness values are used for each bearing in each gear train.

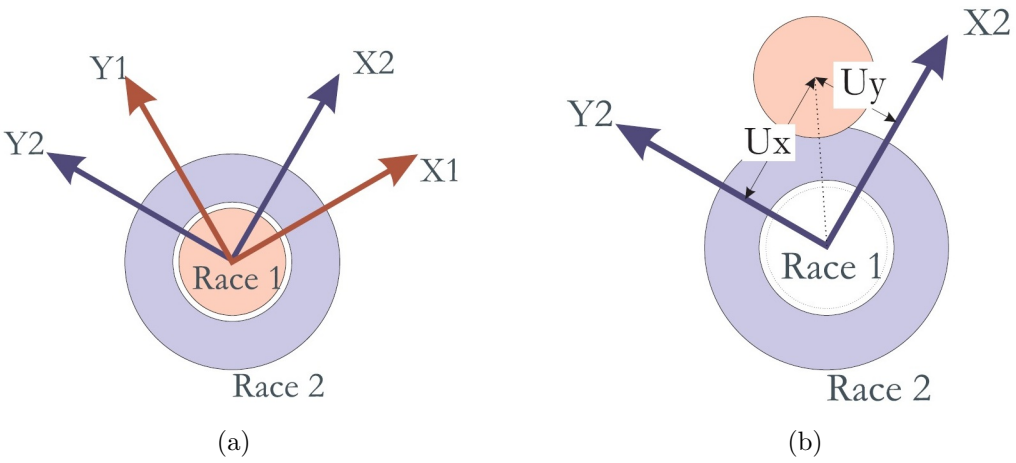

Figure 2.8: (a) Bearing reference frames in Calyx [30], and (b) Bearing deformation in Calyx [30].

Stiffness matrices are a practical way to model bearing connections in large models such as the ones discussed herein, where modeling rolling element bearings with contact at each roller would be computationally intensive. Calyx generates a stiffness matrix using user defined stiffness values. To model a bearing in Calyx, radial stiffness (K_r), axial stiffness (K_z), tilting stiffness ($K_{\theta r}$), and torsional stiffness ($K_{\theta z}$) must be defined. Figure 2.9 illustrates how bearings are defined in Calyx. A bearing

origin and axis orientation must be defined as well as the diameter and axial positions for race 1 and 2. Typically, the bearing origin corresponds to the center of each race in the axial direction.

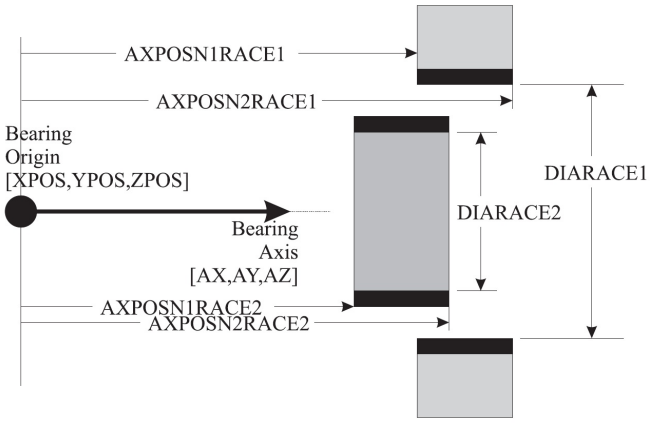

Figure 2.9: Bearing definitions required in Transmission3D [29].

Each bearing race is assigned a reference frame and can be attached to a moving body or the fixed ground. Bearing displacements follow the simple linear relationship given in Equation (2.14) where $\mathbf{K}$ is a 6x6 stiffness matrix, $\mathbf{x}$ is a vector of bearing displacements and rotations, and $\mathbf{f}$ is a vector of bearing reaction forces and moments.

$$\mathbf{Kx} = \mathbf{f} \tag{2.14}$$

In cases where an unloaded bearing deformation is defined, the bearing obeys the relationship given in Equation (2.15), where $\mathbf{x_o}$ represents the imposed unloaded deformation.

$$\mathbf{K}(\mathbf{x} - \mathbf{x_o}) = \mathbf{f} \tag{2.15}$$

2.5 Tooth Micro-Geometry

Gear tooth modifications represent a critical aspect of successfully designing a gear train. Tooth profile modifications refer to the removal of material at either the tooth tip or root in the profile direction. Profile modifications can enable spur or helical gears to run more quietly and carry more load [7]. Proper profile modifications can provide gear teeth with some clearance at the point of first contact in the presence of small spacing errors and misalignments due to bending in loaded teeth. A true involute design provides no clearance at the point of first contact. Lead modifications refer to the removal of material across the facewidth of a tooth. Lead modifications compensate for uneven tooth deflections across the tooth facewidth and can improve contact pressure patterns and load distributions. Both profile and lead modifications can reduce gearbox noise and vibration and improve tooth wear patterns. Profile modifications at the tooth tip and lead modifications are incorporated in the designs of the gear trains discussed herein and are implemented in the finite element/contact mechanics models.

Another distinct advantage of the Transmission3D software package is that gear tooth micro-geometry can be accurately modeled including linear or quadratic tip and root modifications, crown modifications, and tabular lead and profile modifications. In the gear trains modeled in this study tooth tip, root, and lead modifications are used. Accurate tooth surface geometry is essential to correlate computational root

strain to experiments. Figures 2.10(a) and 2.10(b) show schematics of linear and quadratic tip modifications, respectively. The magnitude of the modification and the starting roll angle must be defined. Linear tip modifications are implemented in the same way. Figure 2.10(c) shows lead crowning; the geometry is completely defined by an amplitude of material removed. Figure 2.10(d) shows how tabular lead modifications are implemented. Magnitude and zeta must be defined for points across the tooth facewidth. The distance across the tooth facewidth (zeta) varies from -1 to +1. This feature allows non-symmetric lead modifications and edge relief to be implemented.

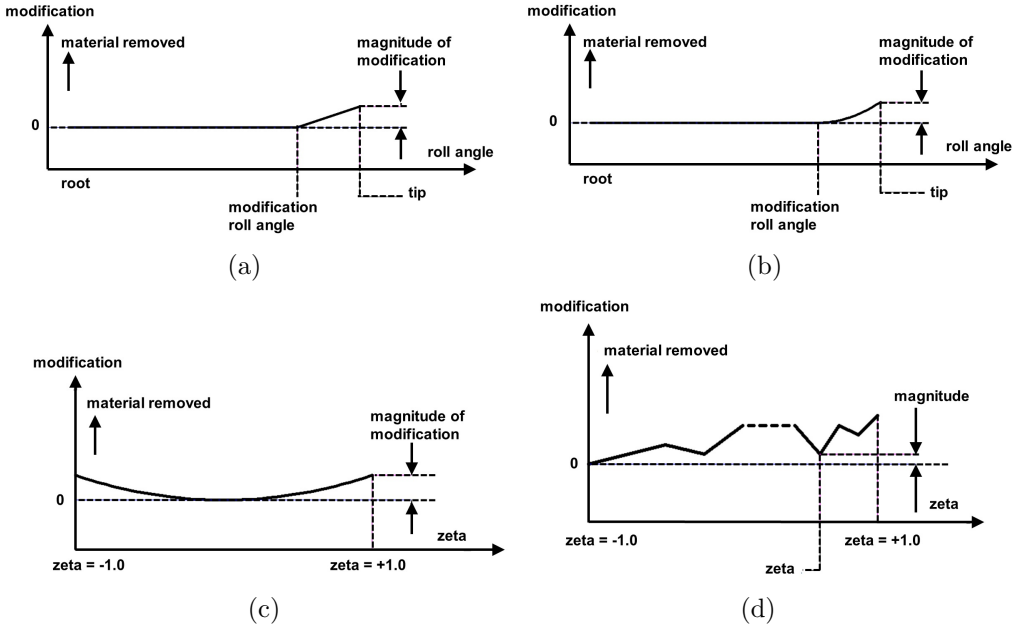

Figure 2.10: Schematic of tooth modification implementation for: (a) linear tip modifications [29], (b) quadratic tip modifications [29], (c) lead crowning [29], and (d) tabular lead modifications [29].

The tooth micro-geometry menu in the Guide user interface is given in Figure E.10 and discussed further in Appendix E.

Chapter 3: GEAR TRAIN MODEL DETAILS

3.1 Gear Train Kinematics

Wind turbine rotors spin at low speeds; whereas the generator spins at high speeds. The drive train converts low-speed rotation of the turbine blades from the wind into high-speed generator rotation to produce electrical energy. The higher the overall gear ratio of the gear train, the larger the difference in rotational speeds at each end of the system. High gear ratios are achievable in the gear trains examined in this thesis due to their multi-stage, planetary configurations. Modern wind turbine rotors typically rotate at 12 to 30 rpm and typical generators require between 1200 and 1800 rpm [34]. Figure 3.1, taken from the Advanced Wind Turbine Drivetrain Concepts Workshop Report [22], illustrates the location of the gearbox in a conventional wind turbine drive train configuration. The rotor blades connect to the hub that is attached to the main rotor shaft. Typically, a large bearing is placed at the front of the main rotor shaft. The gear train is situated inside the gearbox housing shown in the middle of the drive train in Figure 3.1. A mechanical brake is typically situated on the high-speed output shaft that powers the generator. Its purpose is to decelerate the rotor in the event of an overspeed and to hold the shaft stationary during shutdown [6].

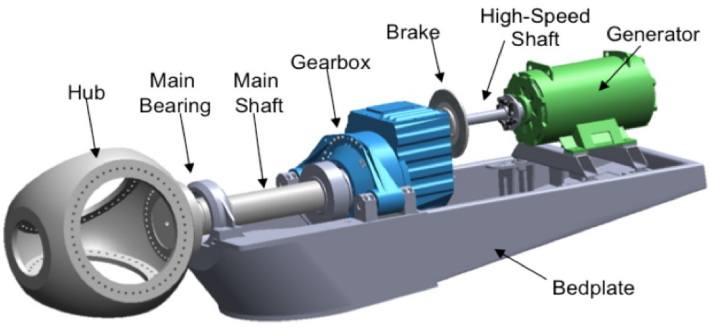

Figure 3.1: Conventional wind turbine drive train configuration [22].

The Orbital2 gear trains examined in this thesis consist of three stages, including a differential planetary, a fixed-carrier epicyclic, and a parallel-axis stage. Each stage operates at a different mesh frequency. In order to conduct a computational analysis for each gear train, system speeds and mesh frequencies are calculated for each stage. Each gear train examined herein operates at different speeds and has different gear ratios. The kinematics of planetary stages 1 and 2 are given as [35]

$$\frac{\omega_{s1} - \omega_{c1}}{\omega_{r1} - \omega_{c1}} = -\frac{Z_{r1}}{Z_{s1}}, \tag{3.1}$$

$$\frac{\omega_{s2} - \omega_{c2}}{\omega_{r2} - \omega_{c2}} = -\frac{Z_{r2}}{Z_{s2}}, \tag{3.2}$$

where ω_s, ω_c, and ω_r represent the speed of the sun, carrier, and ring gear, respectively. Z_r and Z_s are the number of teeth on the ring and sun gear.

In the gear trains examined in this thesis, the parallel axis stage consists of an externally meshed helical wheel that is attached to the stage 2 sun and a helical pinion

that is attached to the high speed output shaft. The relationship between speed ratio and the ratio of number of teeth for stage 3 is given as [35]

$$\frac{Z_p}{Z_w} = \frac{\omega_w}{\omega_p}. \tag{3.3}$$

In order to maintain nomenclature consistency with the actual systems, Equation (3.3) denotes the number of pinion teeth and the speed of the pinion as Z_p and ω_p, respectively. Similarly, Z_w and ω_w represent the number of wheel teeth and the speed of the wheel, respectively.

Using these relationships, gear speeds and mesh frequencies can be determined for each stage and the overall speed ratio of the gear train can be calculated. The speed of the main rotor shaft is known for each gear train and the design of each system is explained further later in this chapter. The speed of the main rotor shaft corresponds to the speed of the stage 1 ring (ω_{r1}) and the speed of the stage 2 carrier (ω_{c2}) in each system. The stage 1 carrier is fixed to the housing, thus ($\omega_{c1} = 0$). (ω_{s1}) = (ω_{r2}) because both gears are connected by a drive flange. Equation (3.4) gives the speed of the stage 1 sun (ω_{s1}) as

$$\omega_{s1} = \frac{-\omega_{r1} Z_{r1}}{Z_{s1}}, \tag{3.4}$$

using the speed of the stage 1 ring (ω_{r1}) and the number of teeth on the stage 1 ring (Z_{r1}) and sun (Z_{s1}).

Substitution of Equation (3.4) into Equation (3.2) and use of the relationship given in Equation (3.3) yields the overall speed ratio for an entire gear train and is given as

$$\frac{\omega_g}{\omega_b} = -\frac{Z_w}{Z_p}\left[\frac{Z_{s1}Z_{s2} + Z_{r1}Z_{r2} + Z_{s1}Z_{r2}}{Z_{s1}Z_{s2}}\right], \tag{3.5}$$

where ω_g denotes the speed of the generator and high-speed output shaft that is connected to the stage 3 pinion and ω_b denotes the speed of the wind turbine blades and main rotor shaft. Given the speed of the blades, the speed of the output shaft can be calculated using Equation (3.5). The speed of the blades corresponds to the speed of the stage 1 ring (ω_{r1}) and the speed of the stage 2 carrier (ω_{c2}).

Mesh frequencies for each stage can be calculated using these kinematic relationships. Equation (3.6) gives the mesh frequency for a simple gear pair as

$$\omega_{mesh} = \omega_p Z_p, \tag{3.6}$$

where ω_p and Z_p represent the speed of the pinion and the number of teeth on the pinion, respectively. Mesh frequency can be calculated for a planetary gear following

$$\omega_{mesh} = (\omega_r - \omega_c)Z_r, \tag{3.7}$$

using the speed of the ring (ω_r), the speed of the carrier (ω_c), and the number of teeth on the ring (Z_r).

3.2 Flexpins

One of the main benefits of planetary gears is the use of multiple load paths. Unequal load sharing results from torsional wind-up of the carrier, machining tolerances, position accuracy of the pin, and bearing clearances. Planetary carriers are often equipped with straddle-mounted planets, having pins supported on either side of the carrier [36]. This type of straddle-mounted pin resists tilting under a planet load and leads to a heavy and complex carrier. Many different designs have been employed to achieve load sharing between planets. This includes introducing more elastic compliance into the system using flexible ring gears. Other designs have implemented floating ring gears, sun gears, and planet carriers. A successful way to achieve load sharing among planets and evenly distribute tooth contact patterns is the flexible pin, also called flexpin, that was invented in 1964 by Ray J. Hicks [37]. This novel method of providing load sharing between planets has been applied to a large variety of industrial, aerospace, marine, and wind turbine gear trains [38].

The flexpin employs a double cantilevered pin design as shown in Figure 3.2(a). The pin is cantilevered to the carrier (shown on the left side of Figure 3.2(a)). The opposite end of the pin is connected to the spindle (shown on the right side of Figure 3.2(a)). The inner race of the planet bearings (typically tapered rolling element bearings) connects to the outer diameter of the spindle as shown in Figure 3.2(b). The outer race of the bearings connects to the inner diameter of the planet.

Not only does the flexpin eliminate the need for straddle mounting, but it allows use of the maximum number of planets subject to tip-to-tip clearance constraints. An important design feature is that the pin that is cantilevered at one end to the carrier and the spindle that is cantilevered to the other end of the pin are co-axial,

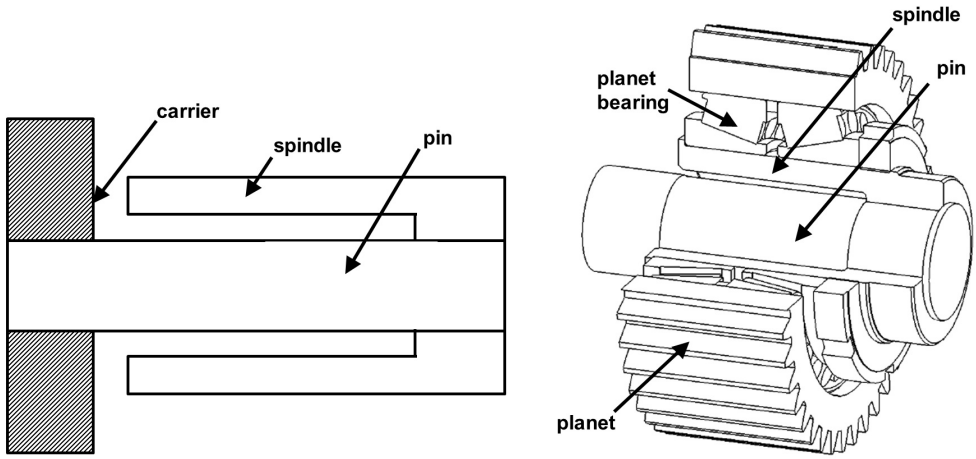

(a) (b)

Figure 3.2: (a) Cross section of a Hicks flexible pin cantilevered to a carrier at the left and (b) cutaway view of a Hicks flexible pin showing tapered rolling element planet bearings and a planet gear.

which enables deflection in two planes. This feature makes the flexpin virtually self aligning [39]. Essentially, the flexpin can deflect independently in a circumferential direction, which helps equalize force distribution among planets. When tooth mesh forces are applied to a planet supported by a flexpin, the angular deflection caused by bending of the pin cantilevered to the carrier can be offset by the angular deflection in the opposite direction caused by the bending of the spindle cantilevered to the opposite end of the pin [36]. This prevents tilting of the planet (Figure 3.3(b)). In a recent study, Montestruc [40] noted that the Hicks flexpin design improves planet load sharing and power to weight ratios in planetary transmissions. The finite element software used in this study accurately models flexpins for both planetary stages of each gearbox. Figure 3.3(a) shows a cutaway view of the finite element model of an undeformed stage 2 flexpin. Figure 3.3(b) shows a cutaway view of the same flexpin

with exaggerated deformation under nominal loading. The flexpin is behaving as expected, with the spindle remaining level and most of the deflection occurring in the pin cantilevered to the carrier.

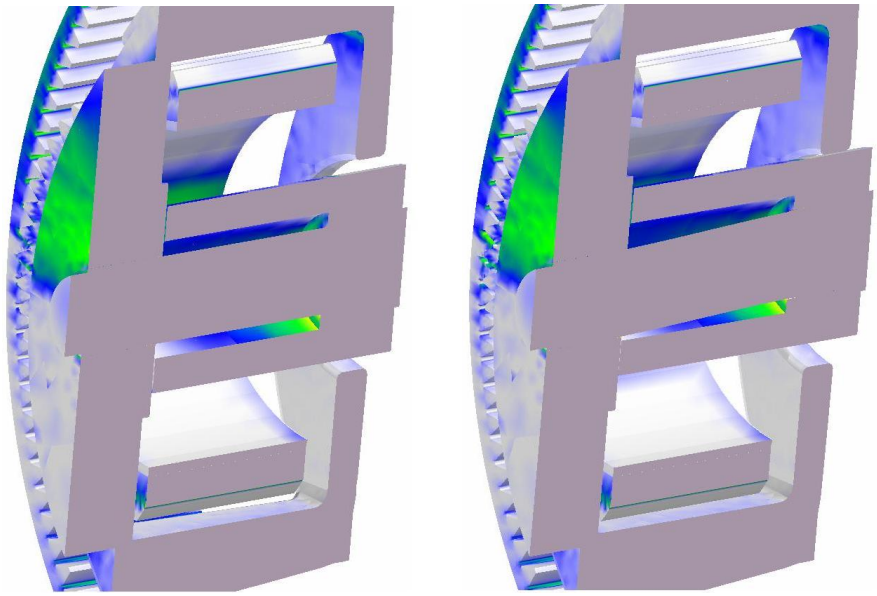

(a) (b)

Figure 3.3: Cutaway view of a stage 2 flexpin on the Orbital2 W3600 finite element model: (a) undeformed pin, and (b) loaded pin with exaggerated deformation.

The flexpin design has proven to be effective throughout the years. Load distribution across planet, sun, and ring tooth facewidths has been observed in gearboxes where flexpins have been utilized. A more even load distribution across tooth facewidths is apparent when compared to earlier gearboxes that used straddle-mounted pin design. Achieving equal loads across tooth facewidths ensures equal loads along the planet bearings which is critical in high torque, low speed planetary configurations such as wind turbine gear trains. Several gearbox designs that use flexpins have

replaced earlier gearboxes that suffered repeated failures. One particular example examined by Hicks [39] is a planetary design for a 300 horsepower gearbox designed for an aircraft fuel pump test rig. The gearbox that it replaced was a conventional wheel and pinion that suffered recurring failures of its high-speed bearings. These failures were attributed to a change in bearing attitude which took place in the pinion when the load was varied. Twenty of these replacement gearboxes were monitored over a span of four years, during which time they provided trouble-free service. The replacement gearboxes are also popular with test rig fitters because they only weigh 40 pounds, compared to the previous gearboxes that weighed 200 pounds [39].

The weight saving advantage of the flexpin design in planetary gearboxes is apparent in the following example of a single-input single-output 6500 horsepower marine propulsion gearbox with an engine speed of 400 rpm and a propeller speed of 100 rpm, as discussed by Hicks in [39]. For this specific application, the gearbox with a flexible pin design would have six planets and weigh 8 tons. A conventional planetary gearbox designed to the same criteria would weigh 14 tons and a parallel shaft gearbox, also designed to the same criteria, would weigh 25 tons [39]. Not only are designs that utilize the flexpin a great deal lighter than their conventional counterparts, flexpin epicyclic gearing components can be made more cheaply and accurately than any other type because smaller machine tools can be used during production. The smaller, lighter components in gearboxes with flexpins ensure lower pitch line velocities and inertias, which reduce dynamic loads due to manufacturing errors. This has proven to be very beneficial in high speed gearboxes. An example of the torque capacity advantage of flexpins in planetary configurations was discused in [38]. Figure 3.4 shows a seven pin planetary gear set built with Hicks flexpins. Compared to

a rigid pin, three planet configuration designed to the same specifications, the flexpin design increases torque capacity by a factor of 2.33 [38].

Figure 3.4: Seven planet Hicks flexible pin planet carrier assembly [38].

Flexpins represent one of the key design features of all of the Orbital2 wind turbine gear trains examined herein. Since its invention, the flexpin has proven to be effective and has led to longer lasting, more reliable gear trains. The finite element software used in this study has the capability to accurately model flexpins. This leads to more complete finite element models that effectively capture planet load sharing and ultimately leads to more accurate comparisons to the actual systems.

Implementing flexpins into finite element models in Calyx requires a finite element carrier. A Fourier surface is defined at each pin hole location in the externally meshed finite element carrier when converting it to Calyx mesh files using the CVTBDF program. As discussed in Chapter 2, a circular and axial order must be defined for the surface as well as its location and length. The flexpin itself consists of two shafts, each consisting of multiple segments. As shown in Figure 3.5, the first shaft is the pin and

is cantilevered to the carrier. The second shaft makes up the spindle and is connected to the end of the pin opposite the carrier by a Fourier surface. Typically, a circular order of eight and an axial order of one is sufficient for displacement interpolation at the pin-carrier and the pin-spindle interface.

A Fourier surface is defined on the outer diameter of the first and last segment of the pin and on the inner diameter of the last segment of the spindle. A Fourier surface also connects the outer diameter of the planet rim to the base of the planet teeth. Planet bearings are modeled as stiffness matrices. The inner race connects to a Fourier surface on the outer diameter of the spindle and the outer race connects to a Fourier surface defined on the inner diameter of the planet rim. These Fourier surfaces are shown in Figure 3.5. The Multyx menus used to construct shafts and flexpins are discussed in Appendix E.

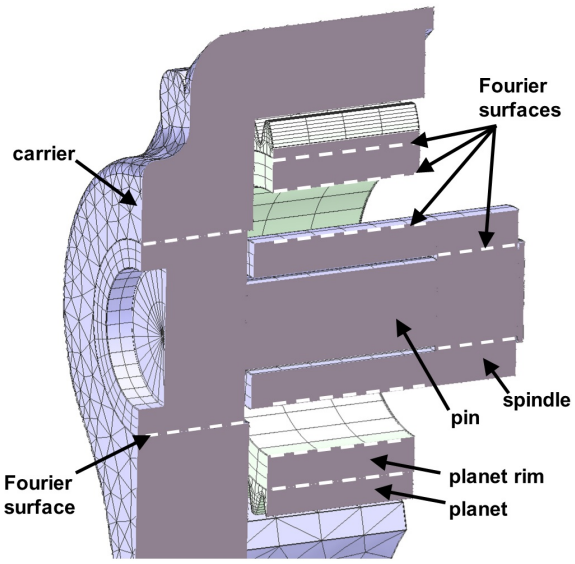

Figure 3.5: Construction of a stage 2 flexpin on the finite element/contact mechanics model of the FC5500 model.

3.2.1 Rotor Definitions in the Finite Element/Contact Mechanics Models

As discussed in Chapter 2, each rotor is assigned its own reference frame. Finite element computations are performed for each individual rotor in its reference frame and each rotor must be sufficiently constrained in its reference frame to ensure that system stiffness matrices are well conditioned. The gear trains discussed in this thesis consist of multiple rotors that contain multiple system components.

In Calyx, a rotor can be defined as an input, output, idler, inactive, or attached to the housing. An input rotor spins at a specified speed and is constrained in the θ_z direction in the rotating reference frame. Furthermore, the rotational displacement about the reference frame of an input rotor is zero unless an initial rotation is specified. A rotor defined as an output is free to rotate in θ_z relative to its rotating reference frame, but an initial rotation cannot be defined. A torque must be specified on an output rotor. An idler is a rotor that is similar to an output rotor but a torque is not specified. An inactive rotor is ignored during an analysis and a rotor that is attached to the hosing is assumed to have zero rotation in the θ_z direction. Table 3.1 defines each rotor in the gear trains examined herein and the components that make up each rotor.

Table 3.1: Rotor definitions and components used in each model

Rotor	Type	Components
1	INPUT	Main rotor shaft, drive flange 1, stage 1 ring, and stage 2 carrier, flexpins, planets, and support plate
2	IDLER	Stage 1 sun, drive flange 2, and stage 2 ring
3	IDLER	Stage 2 sun and shaft
4	IDLER	Stage 3 wheel and shaft
5	OUTPUT	Stage 3 pinion and output shaft
6	ATTACHEDTOHOUSING	Housing, stage 1 carrier, flexpins, and planets

Constraints can be defined for each rotor in the x, y, z, θ_x, θ_y, and θ_z directions. Every component in a rotor must be attached to some part of the rotor that is constrained. These constraints are applied at defined locations on shaft segments or to defined nodes on externally meshed components. Furthermore, a flexible or rigid constraint can be defined on the inner or outer diameter of any given shaft segment. Reference frame reaction forces and moments flow through these locations with constraints. The Multyx rotor menu in the Guide user interface is discussed in Appendix E.

3.3 W3600 System Description

3.3.1 Finite Element/Contact Mechanics Model Overview

The Orbital2 W3600 is a 3.6 MW offshore wind turbine gear train. The complete finite element model of the W3600 gear train examined in this thesis includes a finite

element housing, carriers, drive flanges, and flexible pins in the planetary stages. A cutaway view of the finite element model is shown in Figure 3.6.

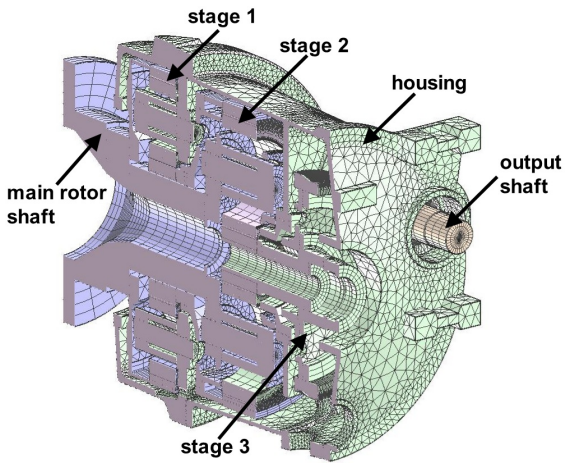

Figure 3.6: Cutaway view of the finite element model of the Orbital2 W3600 gear train.

The W3600 gear train contains one fixed-carrier planetary stage (stage 1), one differential planetary stage (stage 2), as well as a stage with a helical wheel and pinion (stage 3). The main rotor shaft that connects to the wind turbine blades is attached to the stage 1 ring via a drive flange and is also attached to the stage 2 carrier. The stage 1 sun is connected to the stage 2 ring via a second drive flange while the stage 2 sun is connected to the same shaft as the stage 3 wheel that meshes with a helical pinion. The stage 3 helical pinion is attached to the output shaft that powers the generator. The housing has an external reaction arm on either side that is attached to a torque reaction system fixed to the nacelle in actual operation. The purpose of the torque reaction system is to protect the gear train from all types of overloads created by instantaneous wind loads.

The finite element model boundary conditions are shown in Figure 3.7. The model is supported at the front of the main rotor shaft. Furthermore, a constraint is applied on the outer diameter of the flange at the front of the main rotor shaft. The model is constrained here in translation (x, y, and z) and constrained in θ_x and θ_y. The reaction arms on either side of the housing are constrained in the rotational degree of freedom with respect to the main axis of the gear box (θ_z) as shown. That is, the nodes on the flat surface of the reaction arms that is parallel to the main axis of the gearbox are held in rotation. These constraints simulate the boundary conditions of the experimental test rig. Gravity is included in the model; it plays a key role in the overall model deflection and the modulation observed in the stage 2 strain signals. It was determined from simulations of a simpler model that the finite element housing and finite element carriers are necessary to capture all of the effects of gravity. The effects of gravity on model deflections and strain modulation will be discussed further in Chapter 5. All system material properties for the W3600 and the other gear trains discussed in this thesis are given in Appendix C.

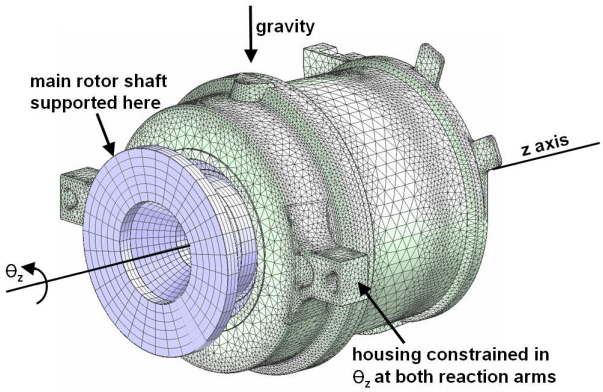

Figure 3.7: Boundary conditions on the W3600 finite element model.

3.3.2 Stage 1 Details

Stage 1 of the W3600 gear train consists of a ring that connects to the main rotor shaft, a sun that connects to the ring of stage 2, and eight planets that are connected to a fixed carrier. The carrier, drive flange and housing were externally meshed and converted to Calyx mesh files. These components are connected to shafts and bearing races through Fourier surfaces. The planets are connected to the carrier through bearings modeled as stiffness matrices that connect the outer diameter of the flexpin spindles to the inner diameter of the planets. The flexpins are cantilevered to the back side of the fixed carrier that is rigidly attached to the housing.

The relative size of the gear train can be observed by looking at the outside diameter of the ring gear and the gear facewidths. The stage 1 ring is connected to the main rotor shaft by drive flange 1. A cutaway view of stage 1 is depicted in Figure 3.8(a). This figure shows the components of stage 1 including the drive flange, carrier, the front segment of the housing, main rotor shaft, gears, and flexpins. Figure 3.8(b) shows a view of stage 1 from the rear of the finite element model of the gear train. The carrier and housing are not included in this figure.

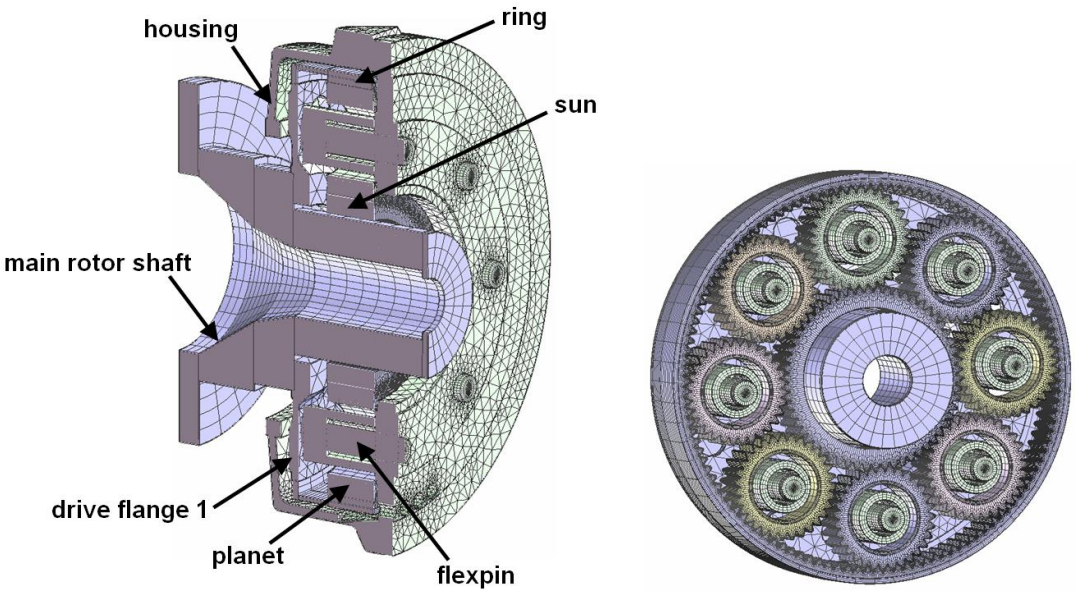

(a) (b)

Figure 3.8: (a) Cutaway view of the finite element model of stage 1 on the W3600 gear train, and (b) View of the finite element model of stage 1 on the W3600 gear train from the rear of the gearbox with the carrier and housing not pictured.

3.3.3 Stage 2 Details

Stage 2 of the W3600 gear train is a differential planetary stage with four planets. The carrier is connected to the main rotor shaft and the ring is connected to the stage 1 sun by drive flange 2. The sun of stage 2 is connected to the same shaft that the stage 3 wheel is attached to. The carrier is also connected to a support plate that is connected via a bearing to the housing. The drive flange (Figure 3.10(b)) and the carrier and support plate (Figure 3.9(b)) were meshed in Patran and converted to Calyx mesh files. Figure 3.9(a) shows the different components of stage 2 including the carrier, drive flange, support plate, gears, and flexpins in the finite element model with the housing not pictured. Figure 3.9(b) shows the carrier and support plate.

The support plate is rigidly attached to the carrier and has holes in the end closest to the back of the gearbox that allow the end of the flexpins to go through. The flexpins are cantilevered to the back side of the carrier and do not attach to the support plate at the opposite end. Figure 3.9(c) shows a view of stage 2 in the finite element model with the housing not shown.

The stage 2 drive flange, annulus, and ring are particularly of interest in this gear train because the experimental root strain from the stage 2 ring indicates that during a planet pass, there is an uneven load distribution across the facewidth of the ring teeth. Figure 3.10(a) shows a cutaway view of the stage 2 ring gear, drive flange, and annulus from the finite element model. This figure depicts the constrained and free ends of the ring, with the constrained end connecting to the stage 2 annulus. This phenomenon will be discussed in more detail in this thesis and ring and annulus deflections will be examined to determine what is causing the variation in strain characteristics across the gear facewidths. Design changes to improve load distributions will be explored. The computational model predicts the measured uneven load and confirms that a modified design rectifies this behavior.

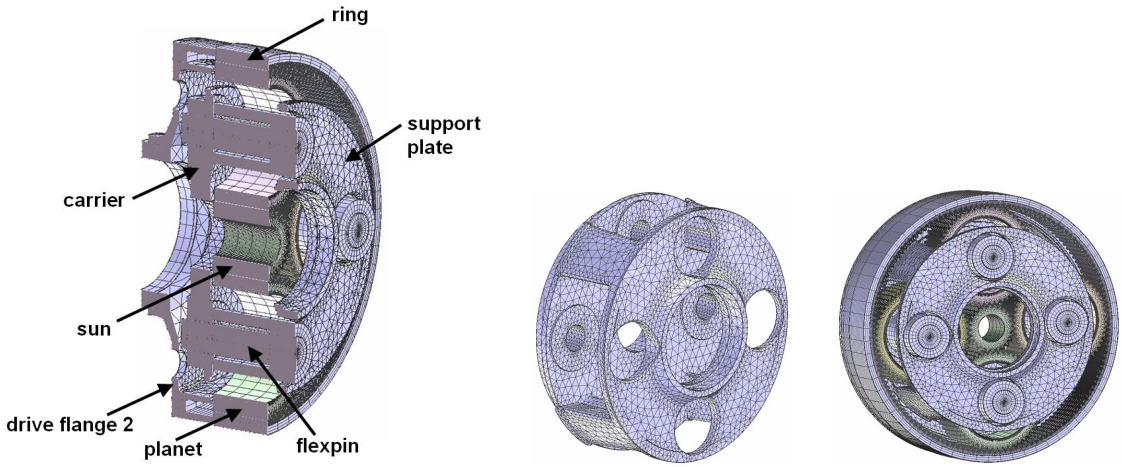

Figure 3.9: (a) Cutaway view of the finite element model of stage 2 on the W3600 gear train, (b) Finite element model of the stage 2 carrier and support plate, and (c) View of the finite element model of stage 2 from the rear of the gearbox.

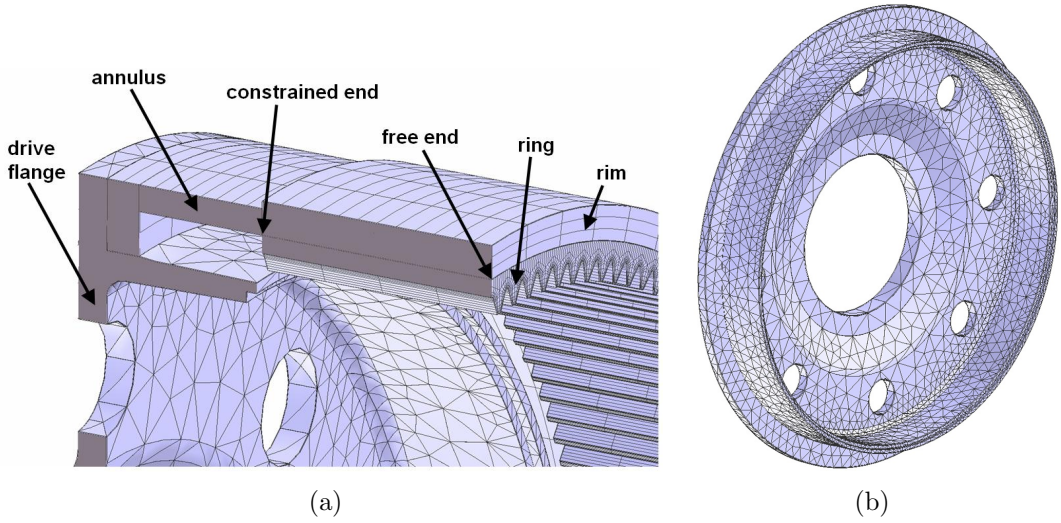

Figure 3.10: (a) Cutaway view of the finite element model of the stage 2 ring gear, drive flange, and annulus, and (b) externally meshed drive flange 2.

The stage 2 annulus and ring rim are constructed as shaft segments in Calyx as shown in Figure 3.11. The axial location of a shaft must be defined and corresponds to the front edge of the first segment. The length, inner diameter, outer diameter, Fourier surfaces, and constraints can be assigned to each segment. The inner and outer surfaces of each segment can be conical or cylindrical. The first segment connects to the externally meshed drive flange at the two Fourier surface locations shown in Figure 3.11. A radial and circular order must be defined for the vertical surface (radial order of one and circular order of eight is used) and a axial and circular order must be defined for the remaining cylindrical surfaces. The inner diameter of the first shaft segment is connected to the drive flange by an axial order of two and a circular order of 32. As discussed in Chapter 2, an axial order of four and a circular order of 64 is used to connect the ring to its rim. This order of displacement interpolation is necessary to accurately capture the deflections of the ring due to the multiple planet meshes. These axial and circular orders are used for all ring-rim interfaces for all of the finite element models discussed herein. The Multyx menus used to construct shafts in Calyx are outlined in Appendix E.

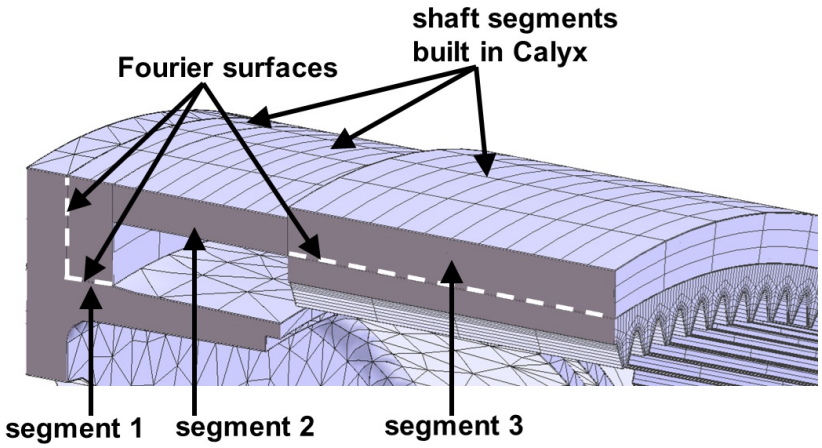

Figure 3.11: Construction of the stage 2 annulus and ring rim using shaft segments in Calyx.

3.3.4 Stage 3 Details

Stage 3 consists of a helical wheel and pinion. The wheel rotates at the same speed as the stage 2 sun. The stage 2 sun shaft connects to the stage 3 wheel shaft through a bearing connection with stiffness properties intended to mimic the behavior of a spline connection. A bearing defined using a stiffness matrix is used to simplify the model and increase computational efficiency. The modeling of a true spline connection would require contact at each spline tooth and would increase simulation time. The implementation of this bearing at the spline connection is discussed further in Appendix A. Figure 3.12(a) shows the stage 3 wheel and pinion. The wheel hub (Figure 3.12(b)) was externally meshed with tetrahedral elements and connects to the wheel rim through Fourier surface displacement interpolation.

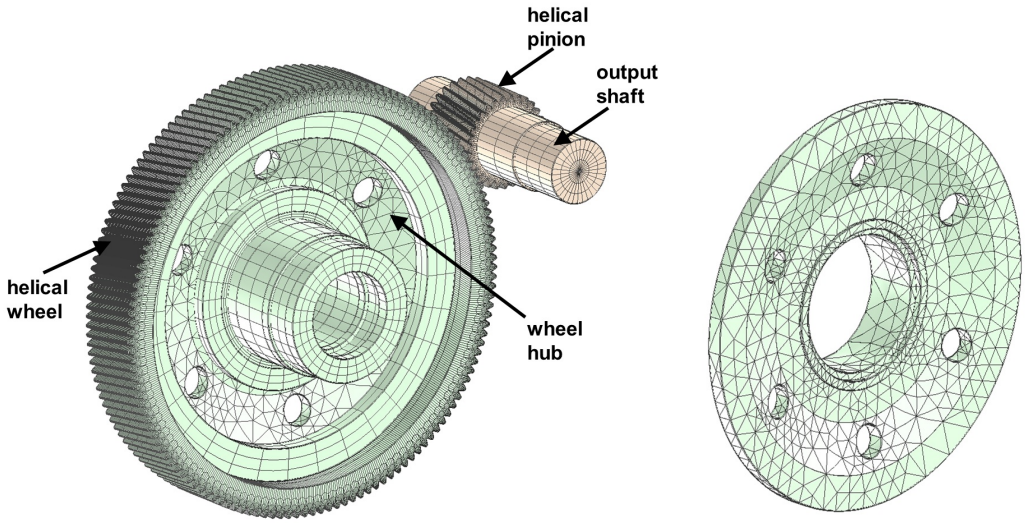

Figure 3.12: (a) W3600 stage 3 helical wheel and pinion, and (b) externally meshed wheel hub.

The high-speed output shaft connected to the helical pinion powers the generator. When setting up the analysis in Calyx, torque was applied to the end of the output shaft (defined as an output rotor) and a speed was specified for the main rotor shaft (defined as an input rotor). A constraint defined on the outer diameter of the output shaft segment closest to the rear of the gear train is where the torque is applied. The motion of the other bodies is a result of the kinematic relationships of the system. Nominal speed and torque values were used that corresponded to the full system experiments (discussed further in Chapter 4). The nominal power is 4,114 kW at an output shaft speed of 1,173 rpm.

In order to compensate for static wind up in the system due to the large torque applied to the output shaft and to ensure correct tooth contact pressure patterns, an initial rotation is applied to the input rotor (main rotor shaft). This initial rotation

is calculated by switching the input and output rotors in the computational model and applying equivalent torque and speeds to each rotor, such that the power flowing through the system is the same. A simulation for one time step yields a rotational displacement of the main rotor shaft in the rotor result file that is an output file in the working directory. This rotational displacement is then used as the initial rotation applied to the main rotor shaft when the input and output rotors are switched back to the main rotor shaft and high-speed output shaft, respectively.

3.4 W2000 System Description

3.4.1 Finite Element/Contact Mechanics Model Overview

The W2000 is a 2 MW offshore wind turbine gear train. While the system kinematics are similar to the W3600, the configuration of the two planetary stages is somewhat different. Stage 2 has four planets and is situated closer to the front of the gearbox than the six planet stage 1. The main rotor shaft is connected to the housing via two bearings along its length before it attaches to the stage 2 carrier and stage 1 drive flange. Finite element carriers, flexpins, drive flanges, and a housing are incorporated in the model. A cutaway view of the W2000 is shown in Figure 3.13.

The W2000 gear train consists of one fixed-carrier planetary stage (stage 1), one differential planetary stage (stage 2), and a helical wheel and pinion (stage 3). The main rotor shaft is attached to the stage 1 ring via a drive flange and is also attached to the stage 2 carrier. The stage 1 sun is connected to the stage 2 ring via a second drive flange while the stage 2 sun is connected to the same shaft as the stage 3 wheel. The stage 3 helical pinion is attached to the high-speed output shaft that powers the generator.

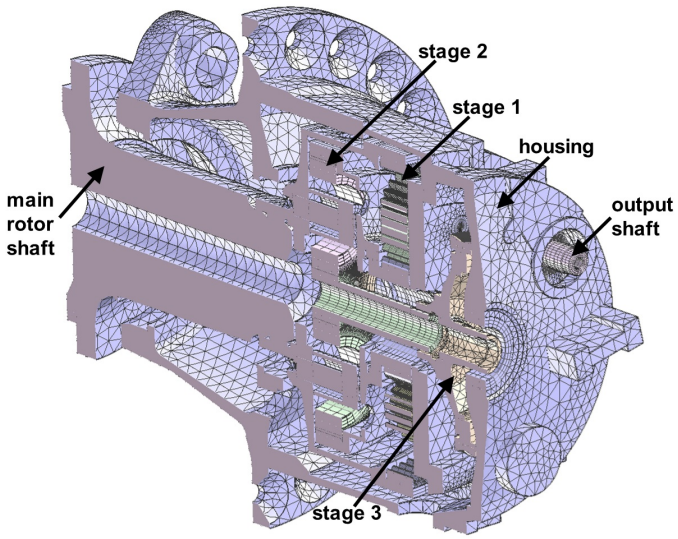

Figure 3.13: Cutaway view of the finite element model of the W2000.

The system boundary conditions are shown in Figure 3.14. Gravity is included in the model. The housing is fixed in translation and rotation along the outer diameter of the large flange in the middle of the housing. That is, all of the nodes along this diameter are fixed in x, y, z, θ_x, θ_y, and θ_z. A mass that corresponds to 300 kN is added to the front of the main rotor shaft as shown in Figure 3.14 to simulate the weight of the second gear train in the back-to-back power circulating test rig configuration. A shaft built in Calyx connects to the front of the main rotor shaft. The length of this shaft is very small compared to its inner and outer diameters. It is given a density such that based on the volume of the shaft segment, its weight corresponds to 300 kN, representing the weight of the second gear train. Details about the experimental test rig will be discussed further in Chapter 4. Root strain from both rings and overall model behavior will be discussed in Chapter 5. In the finite

element model, all bearings connections are made using stiffness matrices. System material properties are shown in Appendix C.

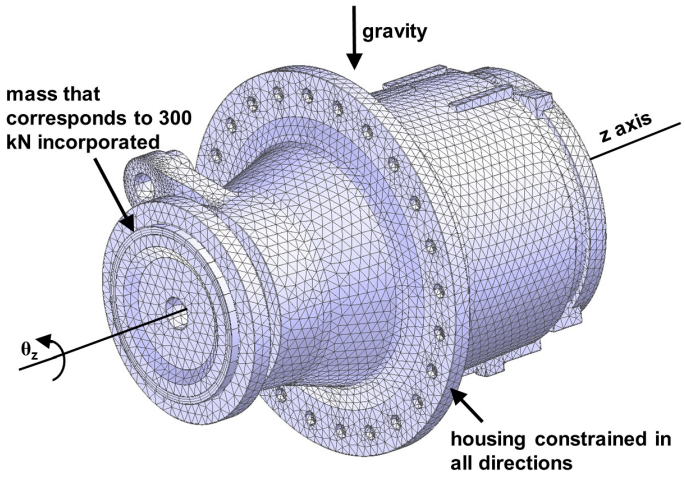

Figure 3.14: W2000 system boundary conditions.

3.4.2 Stage 1 Details

Stage 1 is a planetary stage with six planets and a carrier that is fixed to the housing. The stage 1 ring is attached to the main rotor shaft through the externally meshed drive flange 1. The stage 1 sun is connected to the stage 2 ring through a second externally meshed drive flange. In addition to both drive flanges, the housing, fixed carrier, main rotor shaft, and stage 2 carrier were meshed in Patran using tetrahedral elements and converted to Calyx mesh files. Flexible planet pins are cantilevered to the fixed carrier. Figures 3.15(a) and 3.15(b) show a cutaway view and a view from the front of the gearbox of planetary stage 1, respectively.

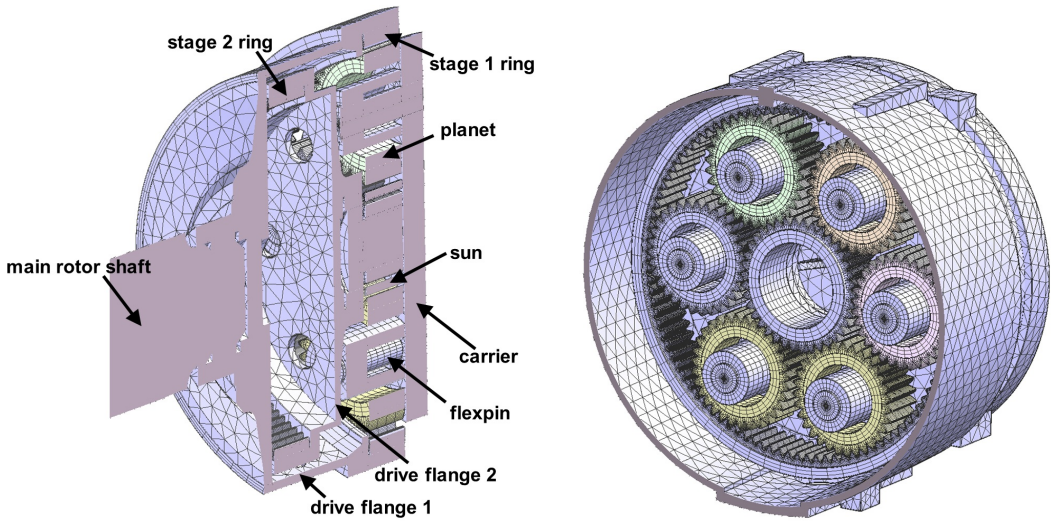

(a) (b)

Figure 3.15: (a) Cutaway view of the finite element model of stage 1 on the W2000, and (b) view of stage 1 from the front of the gearbox.

3.4.3 Stage 2 Details

Stage 2 in the W2000 gear train is a differential planetary stage containing four planets. The carrier is attached to the main rotor shaft. The ring connects to the stage 1 sun via drive flange 2. The sun connects to a shaft that powers the helical wheel in stage 3. Flexible pins are cantilevered to the front of the carrier. Figure 3.16(a) shows a cutaway view of stage 2. Figure 3.16(b) shows a view of stage 2 from the rear of the gearbox with the housing not pictured.

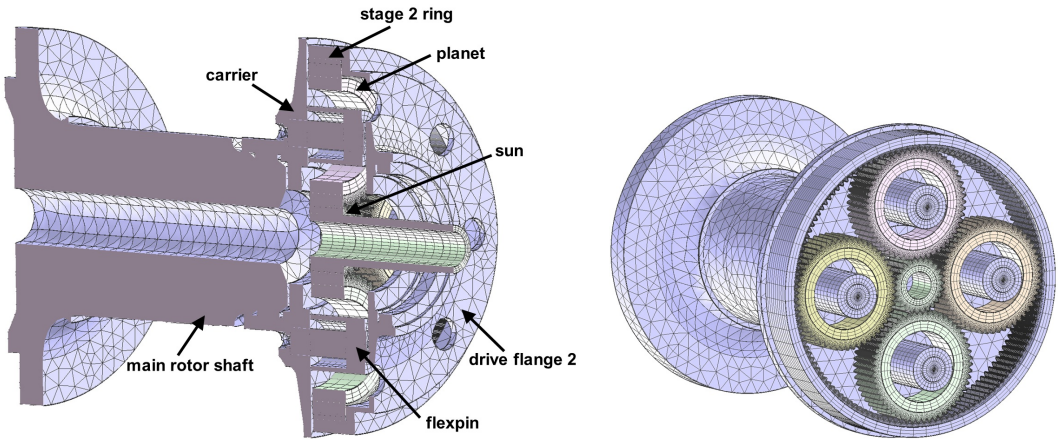

Figure 3.16: (a) Cutaway view of the finite element model of stage 2 on the W2000, and (b) view of stage 2 from the rear of the gearbox with the housing not pictured.

The end of the shaft closest to the back of the gear train that is connected to the stage 2 sun is attached to the stage 3 wheel using a stiffness matrix that is given the appropriate stiffness properties, such as high torsional stiffness and low bending stiffness, to simulate a spline connection at this location. Further details regarding implementation of the spline connection are included in Appendix A.

3.4.4 Stage 3 Details

Stage 3 consist of a large, helical wheel and pinion as shown in Figure 3.17(a). The wheel rotates at the same speed as the stage 2 sun. In order to capture the complex geometry of the wheel hub (Figure 3.17(b)), it was meshed in Patran using ten-noded tetrahedral elements and converted to Calyx mesh files. The pinion is attached to a high-speed shaft that powers the generator. Nominal speed and torque values were used in the model that corresponded to the full system experiments (discussed further in Chapter 4). This nominal loading consists of 2,000 kW power and an output shaft

speed of 1,798 rpm. Similar to the W3600, a torque is applied to the end of the high-speed output shaft and a speed is specified on the main rotor shaft.

Due to the large torque applied to the output shaft, an initial rotation is applied to the input rotor (main rotor shaft) to compensate for static wind up in the system. This initial rotation is calculated as described for the W3600 by switching the input and output rotors and using the rotational displacement of the main rotor shaft as the initial rotation value.

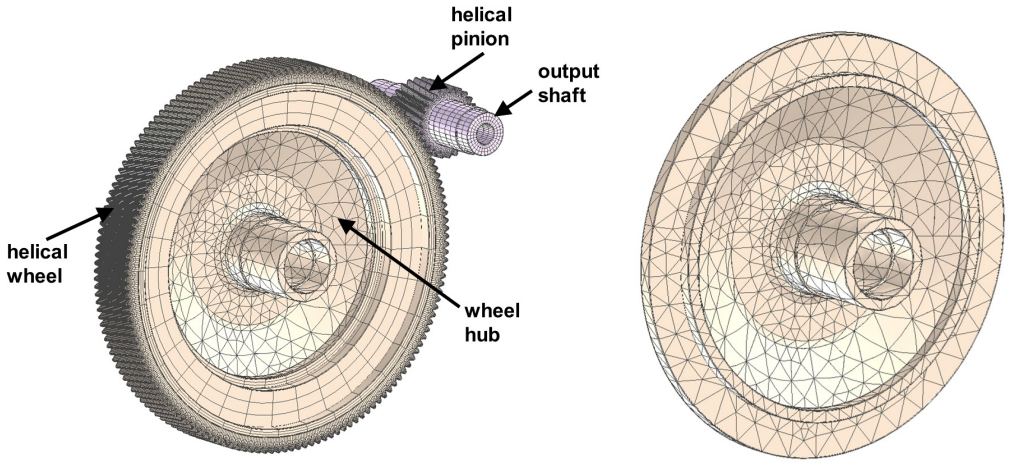

Figure 3.17: (a) W2000 helical wheel and pinion, and (b) externally meshed wheel hub.

3.5 FC5500 System Description

3.5.1 Finite Element/Contact Mechanics Model Overview

The FC5500 is the largest of the three gear trains examined herein. It is a 5.5 MW offshore wind turbine gear train. The configuration of the two planetary stages is very similar to the W3600. Stage 1 is a fixed carrier planetary stage with eight

planets and stage 2 is a differential planetary stage with five planets. Like the other systems discussed hitherto, the complete finite element model includes a finite element housing, carriers, drive flanges, and flexible pins in both planetary stages. A cutaway view of the complete finite element model is shown in Figure 3.18.

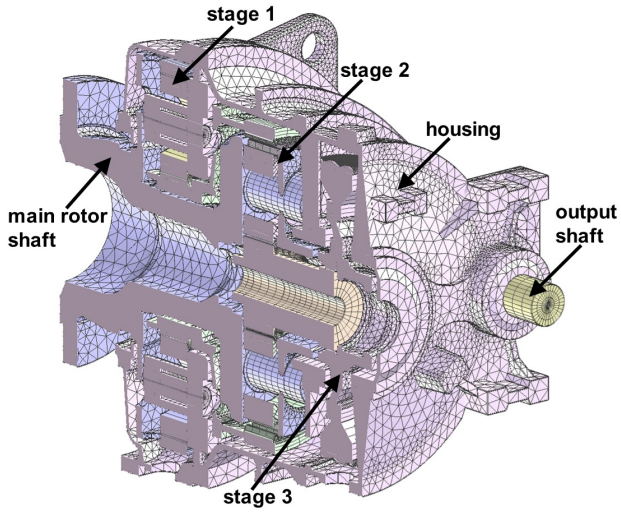

Figure 3.18: Cutaway view of the finite element model of the FC5500 gear train.

The model boundary conditions are shown in Figure 3.19. Like the W3600, the model is supported at the front of the main rotor shaft (the outer diameter of the shaft shown in Figure 3.19 is constrained in x, y, z, θ_x, and θ_y) and the two external reaction arms on either side of the housing are constrained in the rotational degree of freedom only (θ_z) with respect to the main axis of the gear box. These constraints simulate the boundary conditions of the back-to-back power circulating experimental test rig. Gravity is included in the model and like the other gear trains, the effects

of gravity play a key role in understanding model deflections. All system material properties shown in Appendix C.

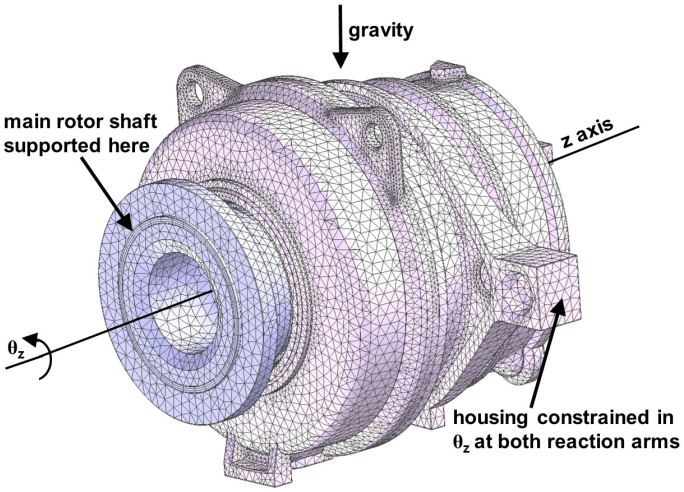

Figure 3.19: FC5500 model boundary conditions.

3.5.2 Stage 1 Details

The stage 1 ring is connected to the main rotor shaft via drive flange 1. The stage 1 carrier is fixed to the housing. Flexpins are cantilevered to the front side of the carrier. The stage 1 sun attached to the stage 2 ring via drive flange 2. The layout of the stage 1 components can be seen in Figure 3.20(a). The main rotor shaft, both drive flanges, both carriers and the housing were meshed in Patran using tetrahedral elements. A view of stage 1 from the front of the gear train can be seen in Figure 3.20(b). The external reaction arms on each side of the housing are attached to hydraulic cylinders in the test rig configuration. This setup simulates the behavior

of a torque reaction system that is installed in the wind turbine nacelle during actual operation that ensures the gearbox undergoes pure torsion.

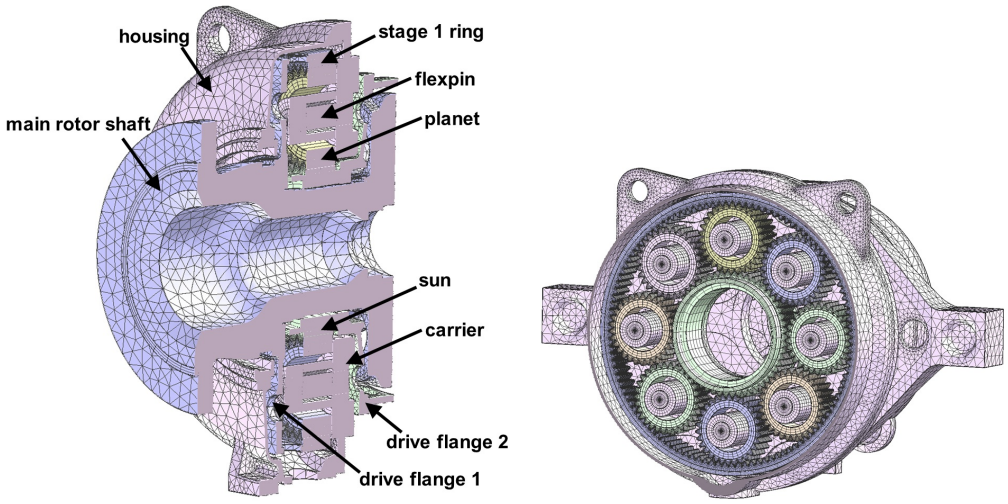

Figure 3.20: (a) Cutaway view of the finite element model of stage 1 on the FC5500, and (b) view of stage 1 from the front of the gear train.

3.5.3 Stage 2 Details

Stage 2 is a differential planetary stage containing five planets and is shown in Figures 3.21(a) and 3.21(b). The carrier is connected to the main rotor shaft by a drive flange. Flexible pins are cantilevered to the back side of the carrier. The stage 2 ring is attached to the stage 1 sun through drive flange 2 (shown in Figure 3.21(c)). The stage 2 carrier is connected to a support plate shown in Figure 3.21(d). In order to mesh the complex geometry, the support plate was meshed in Patran. Fourier surface displacement interpolation is used to connect the carrier to the support plate. The carrier and the arms of the support plate are meshed as one component using tetrahedral elements. Fourier surfaces are defined on the ends of the arms of the

support plate and on the front of the support plate (radial order of one and circular order of eight). These components are connected in this way because the arms of the support plate are hollow and thus, the carrier and support plate could not be meshed as one component. The stage 2 sun is connected to a shaft that attaches to the stage 3 helical wheel through a bearing connection that simulates a spline (discussed further in Appendix A).

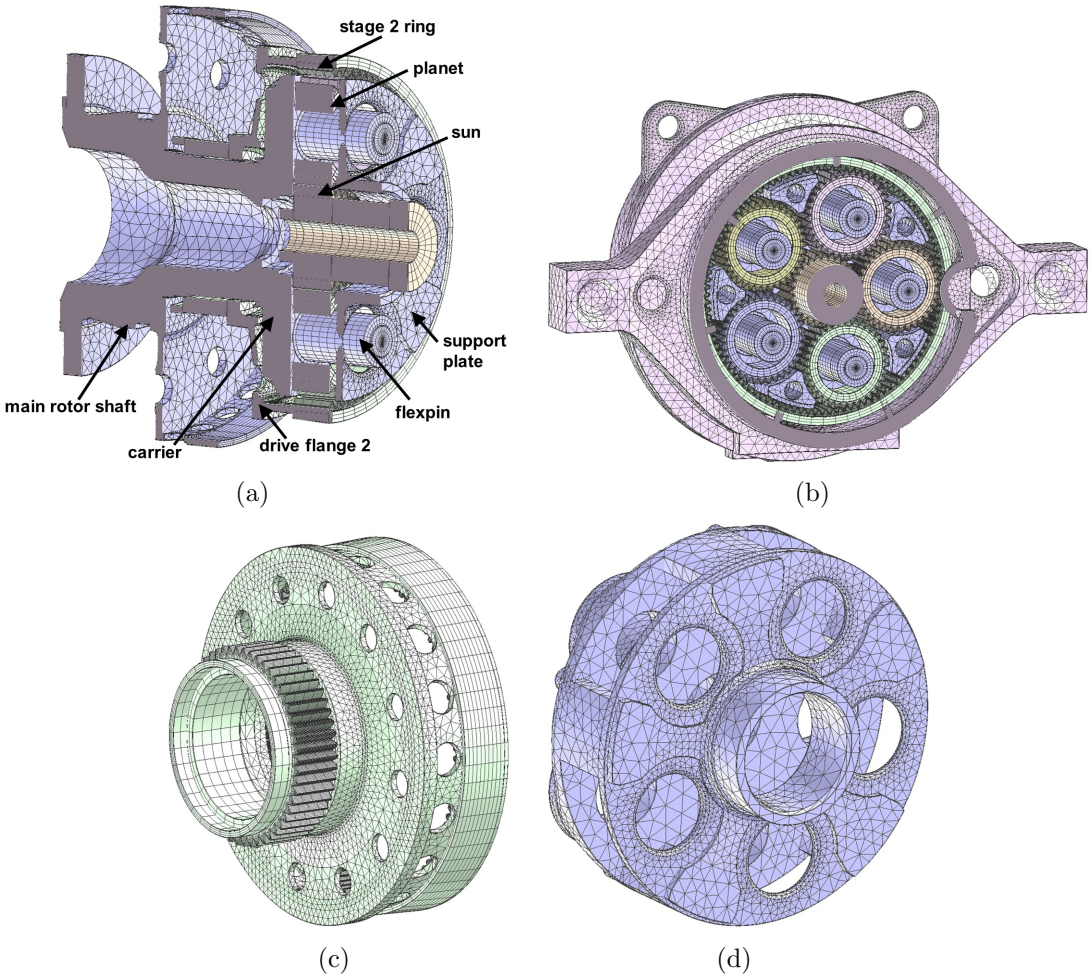

Figure 3.21: (a) Cutaway view of the finite element model of stage 2 on the FC5500, (b) view of stage 2 from the back of the gearbox, (c) drive flange 2, and (d) the stage 2 carrier and support plate.

Root strain will be extracted from both ring gears. The deflections of the stage 2 drive flange and ring will be important when examining load distributions across the facewidth of ring teeth.

3.5.4 Stage 3 Details

Like the other gear trains discussed hitherto, stage 3 (shown in Figure 3.22(a)) of the FC5500 consists of a large helical wheel and a pinion that is attached to the high-speed output shaft that powers the generator. Part of the wheel hub was externally meshed in Patran using tetrahedral elements in order to capture the complex geometric features and is shown in Figure 3.22(b). In the finite element model, torque is applied to the high-speed output shaft and speed is applied to the main rotor shaft. Nominal power is 6,069 kW and nominal output shaft speed is 1,107 rpm. The main rotor shaft is defined as an input rotor in the computational model and a speed of 12.2 rpm is specified.

To compensate for static wind up, an appropriate initial rotation in applied to the main rotor shaft following the procedure given for the previous gear trains. When the input and output rotors are switched, a torque is applied to the main rotor shaft and a speed of 1,107 rpm is specified for the output shaft. The rotational displacement of the main rotor shaft from this simulation is then applied when the input and output rotors are switched back.

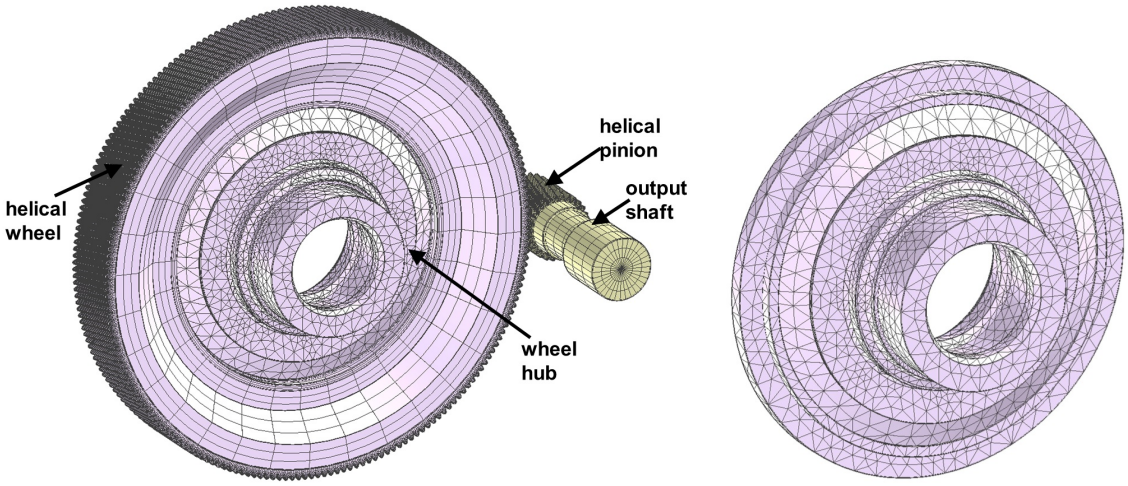

(a) (b)

Figure 3.22: (a) FC5500 helical wheel and pinion, and (b) part of the wheel hub externally meshed in Patran.

3.6 Computational Contact Parameters

Specifying appropriate computational contact parameters is essential in order to accurately capture the contact mechanics associated with moving gear bodies. In Calyx, the computational contact grid and other contact parameters (discussed in Chapter 2) must be defined for each gear pair. The contact parameters must be adjusted for different torque values. The contact parameters used in each gear train model for each defined contact pair are shown in Table 3.2. Each meshing gear pair in the system must be assigned contact parameters in the pairs menu in Multyx. These parameters include the separation tolerance (SEPTOL), the number of divisions in the profile direction (NPROFDIVS), the dimension of each cell in the profile direction (DSPROF), and the number of divisions in the facewidth direction (NFACEDIVS). As discussed in Chapter 2, there are (2F + 1) and (2P + 1) grid cells in the facewidth

and profile directions where F and P represent the user defined NFACEDIVS and NPROFDIVS, respectively.

Table 3.2: Computational contact parameters used in each gear train model

Gear train	Contact Pair	SEPTOL	NPROFDIVS	DSPROF	NFACEDIVS
W3600	Stage 1 ring-planet	2	5	0.29	10
	Stage 1 sun-planet	2	5	0.20	10
	Stage 2 ring-planet	2	5	0.35	10
	Stage 2 sun-planet	2	5	0.20	10
	Stage 3 wheel-pinion	2	5	0.20	8
W2000	Stage 1 ring-planet	2	5	0.27	10
	Stage 1 sun-planet	2	5	0.18	10
	Stage 2 ring-planet	2	5	0.34	10
	Stage 2 sun-planet	2	5	0.20	10
	Stage 3 wheel-pinion	2	5	0.19	8
FC5500	Stage 1 ring-planet	2	5	0.31	10
	Stage 1 sun-planet	2	5	0.22	10
	Stage 2 ring-planet	2	5	0.36	10
	Stage 2 sun-planet	2	5	0.22	10
	Stage 3 wheel-pinion	2	5	0.22	8

The high number of contact grid cells across the tooth facewidths is necessary in order to ensure that the models accurately capture variation in load distribution. This becomes especially important when examining tooth root strain. The number of divisions in the facewidth direction given in Table 3.2 for the gear meshes of the planetary stages represent the values used during simulations run over a mesh cycle for that specific stage. The number of divisions used in the facewidth direction for the other planetary stage are reduced in the interest of computational efficiency. For instance, when investigating tooth root strain on the stage 1 ring by running a simulation over a stage 1 mesh cycle, the NFACEDIVS values used for the stage

1 ring-planet and sun-planet mesh was ten. Furthermore, the NFACEDIVS values used for the stage 2 meshes during this simulation were reduced to four to reduce the number of contact constraints and therefore simulation time. Such high contact grid resolution is not necessary on the planetary stage that root strain is not being extracted from. These NFACEDIVS values were reversed for a simulation run over a stage 2 mesh cycle. The number of divisions in the profile direction for the meshes of both planetary stages is not adjusted for specific simulations.

Proper specifiction of the width of each grid cell in the profile direction (DSPROF) and the number of divisions along the profile of the tooth (NPROFDIVS) yields a parabolic tooth pressure distribution in the profile direction (Figures 2.2(a) and 2.3(c)). These contact parameters are dependent on torque and must be adjusted for different gear train loading.

To illustrate the importance of using the correct number of NFACEDIVS, Figures 3.23(a) and 3.23(b) show an instantaneous contact pressure pattern on a ring tooth from the FC5500 gear train with too few contact grid cells in the facewidth direction and an appropriate number, respectively. It is clear that the instantaneous contact pressure pattern shown in Figure 3.23(a) varies across the facewidth but does not capture the subtle deviations that the contact pressure pattern in Figure 3.23(b) depicts. When extracting tooth root strain from eight gauge locations across the facewidth, a contact grid shown in Figure 3.23(a) would not accurately show deviations in strain between neighboring gauges.

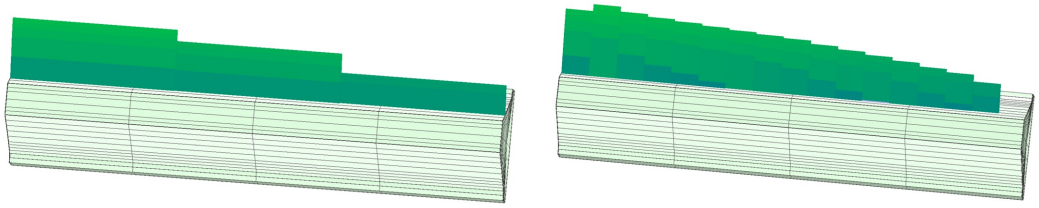

(a) (b)

Figure 3.23: Instantaneous contact pressure pattern on an FC5500 ring tooth with: (a) too few NFACEDIVS and (b) an appropriate number of NFACEDIVS to capture variation in tooth root strain.

Chapter 4: EXPERIMENTAL STRAIN DATA

4.1 Strain Data Acquisition

As part of their development process, Orbital2 conducted full-scale experiments on each of the gear trains examined herein. Voltage from each strain gauge was transferred through a wireless connection between a computer and the Bluetooth transceiver. The relationship between the experimental output voltage and strain is given in Equation (4.1) as

$$V_o = V_{in}\left[\frac{\epsilon G_f}{4 + 0.002\epsilon G_f}\right]G, \tag{4.1}$$

where V_o represents the output voltage, V_{in} is the bridge excitation, G_f is the gauge factor, and G is the electrical gain. The general principal of a strain gaugue is that tension or compression of the mounted gauge causes a change in resistance that will unbalance the bridge and yield a nonzero output voltage. The bridge excitation voltage (V_{in}) is the voltage applied across the bridge and the gauge factor (G_f) is the ratio of the fractional change in resistance to strain [41]. The electrical gain (G) simply amplifies the output voltage. The quarter bridge configuration used consists of

one gauge and three resistors. Equation (4.2) shows how strain (ϵ) can be calculated by manipulating Equation (4.1) following

$$\epsilon = 2000\left[\frac{V_o}{G_f(-V_o + 500GV_{in})}\right], \tag{4.2}$$

with units of μm/m. Experimental strain at each gauge location on both ring gears is given in Appendix D for each gear train. Table 4.1 gives the strain gauge parameters used in Equations (4.1) and (4.2). These parameters are used when converting experimental voltage to microstrain for each gear train.

Table 4.1: System strain gauge parameters

Parameter	Value
Bridge excitation (V_{in})	3.3 V
Gauge factor (G_f)	2.06
Electrical gain (G)	296.9

Using these strain gauge parameters and Equation (4.2), a relationship between measured voltage and strain can be determined. This relationship is given as

$$\epsilon = 1982\frac{\epsilon}{volt}, \tag{4.3}$$

where strain is in μm/m.

4.2 W3600 Test Rig and Experimental Strain Data

Figure 4.1 shows one gear train in the back-to-back, power circulating experimental test rig of the W3600 gear train as described in [42]. The gear train housing has external reaction arms on each side that connect to a hydraulic cylinder, as seen just to the right of center at the bottom of Figure 4.1. This configuration simulates the torque reaction system that connects to these reaction arms when the gear train is in operation. The objectives of these experiments were to obtain ring gear root strain from the ring gears of both planetary stages to evaluate load distribution, measure sound intensity to evaluate radiated sound power, and record noise and vibrations levels at specific locations. The experimental data examined in this thesis is ring gear root strain.

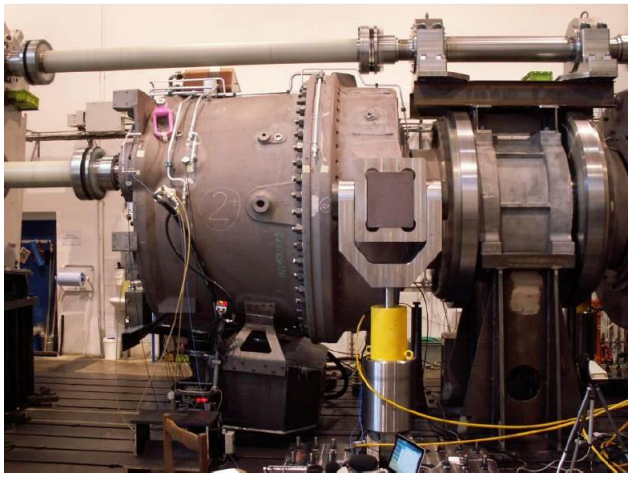

Figure 4.1: One gear train in the W3600 back-to-back, power circulating experimental test rig configuration [42].

There are eight strain gauges across the facewidth of both stage 1 and stage 2 ring gears. Figure 4.2(a) shows the placement of strain gauges in the root of the stage 1 ring gear. The gauges are covered with a protective white coating. The strain gauges were connected to a Bluetooth gear alignment module in quarter bridge configuration. Two independent modules with high capacity lithium thionyl batteries were installed on each ring gear annulus next to a set of strain gauges. These were separated by approximately 131 degrees on the stage 1 annulus and 180 degrees on the stage 2 annulus. The strain signals were acquired at 1,250 Hz for all modules. Figure 4.2(b) shows the entire stage 1 ring with gear alignment modules installed. The modules are visible on the annulus at the bottom of the ring and approximately 131 degrees in the counterclockwise direction.

Figures 4.3(a) and 4.3(b) show the layout of strain gauges across the stage 1 and stage 2 ring gear facewidths, respectively. The position of each strain gauge in the profile and facewidth directions is accurate to within 1 mm. The strain gauge dimensions are 1.5 mm (in the profile direction) by 2 mm (in the facewidth direction). Strain data was collected during operation of the gear train under a range of load conditions. As discussed in Chapter 3, experimental strain data will be correlated to the computational model for the nominal operating input power of 4,114 kW and an output shaft speed of 1,173 rpm. This speed at the high-speed output shaft corresponds to a speed of 14 rpm at the main rotor shaft.

Typical experimental strain data is shown in Figure 4.4. Each strain signal exhibits a rounded hump during a planet pass and a sharp peak when a planet contacts the instrumented tooth. One goal in this study is to examine strain across the facewidth of the stage 2 ring gear. Figure 4.4(a) and 4.4(b) show the experimental root strain

(a) (b)

Figure 4.2: (a) Strain gauges placed across the facewidth of the stage 1 ring gear [42], and (b) Stage 1 ring gear with gear alignment modules installed [42].

signals from the gauge closest to the free (gauge 1) and the constrained (gauge 8) ends of the stage 2 ring, respectively. The data shows a rounded hump yielding a slow transient related to each passing planet gear with a rapid reversal in strain when a passing planet meshes with the instrumented ring gear tooth. Superimposed on this signal are distinct, higher frequency ripples due to tooth contact away from the strain gauges.

The experimental strain results show a variation in strain characteristics across the facewidth with more pronounced strain peaks closer to the constrained end of the ring and less pronounced strain peaks near the free end of the ring gear. The ring gears in both planetary stages are constrained at one end where they connect to a drive flange and are unconstrained at the opposite end. These differing constraints influence the ring deflection and contribute to the variation in strain across the ring facewidth. This will be investigated further using the computational model in Chapter 5. There

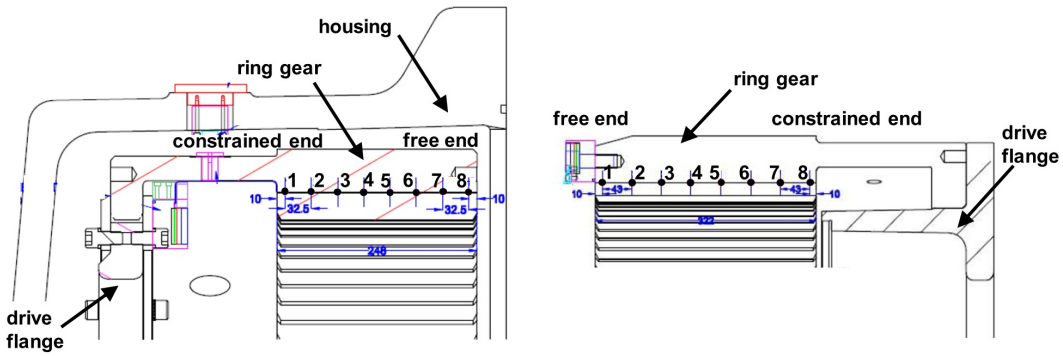

(a) (b)

Figure 4.3: W3600 strain gauge layout across: (a) the stage 1 ring facewidth and (b) the stage 2 ring facewidth.

is a more pronounced strain peak during a planet pass at the constrained end of the ring. The strain gauge data from the constrained end (gauge 8) shows a distinct modulation. This modulation phenomenon will be investigated further in Chapter 5.

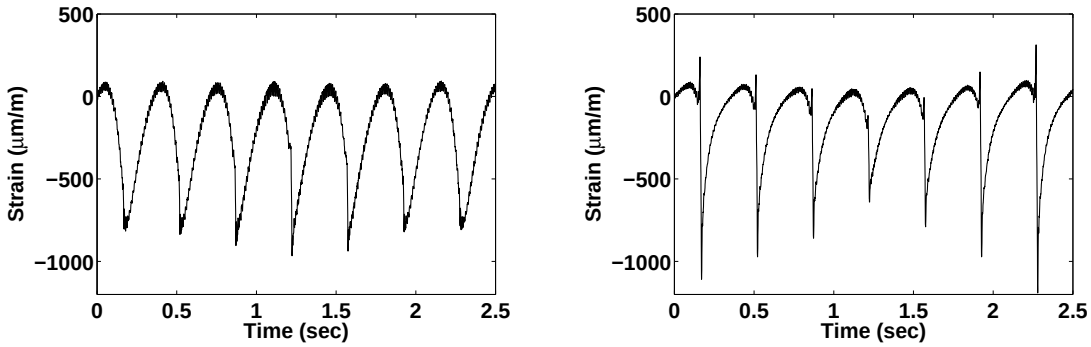

(a) (b)

Figure 4.4: Experimental strain from the stage 2 ring on the W3600 gear train from the gauge: (a) closest to the free end (gauge 1) and (b) closest to the constrained end (gauge 8).

Experimental strain data across the facewidth of the stage 1 ring gear is also compared to the finite element/contact mechanics model. Figure 4.5(a) shows strain from the gauge closest to the free end of the ring, while Figure 4.5(b) shows strain from the gauge closest to the constrained end of the ring. While stage 1 experimental strain results show a slight variation in peak-to-peak strain between the free and constrained ends of the ring, there is no distinct strain peak at the constrained end as observed in the stage 2 data . Furthermore, the strain reversal due to mesh contact on the stage 1 ring teeth is exceeded by a slower transient related to each passing planet gear. The modulation at the constrained end of the stage 2 ring gear (Figure 4.4(b)) is not present in stage 1 (Figure 4.5(b)).

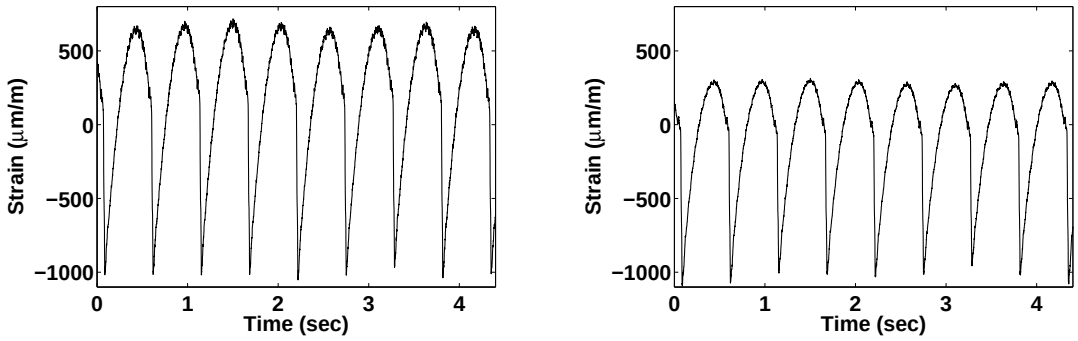

(a) (b)

Figure 4.5: Experimental strain from the stage 1 ring on the W3600 gear train from the gauge: (a) closest to the free end (gauge 8) and (b) closest to the constrained end (gauge 1).

Frequency content of the experimental strain signals is examined. A discrete Fourier transform (DFT) of experimental strain is calculated using the fast Fourier

transform (FFT) algorithm. Figures 4.6(a), and 4.6(b) show the spectra of experimental strain (μm/m) from the free and constrained end of the stage 1 ring. As expected, peaks at multiples of planet pass frequency (ω_{pp}) can be seen in both figures.

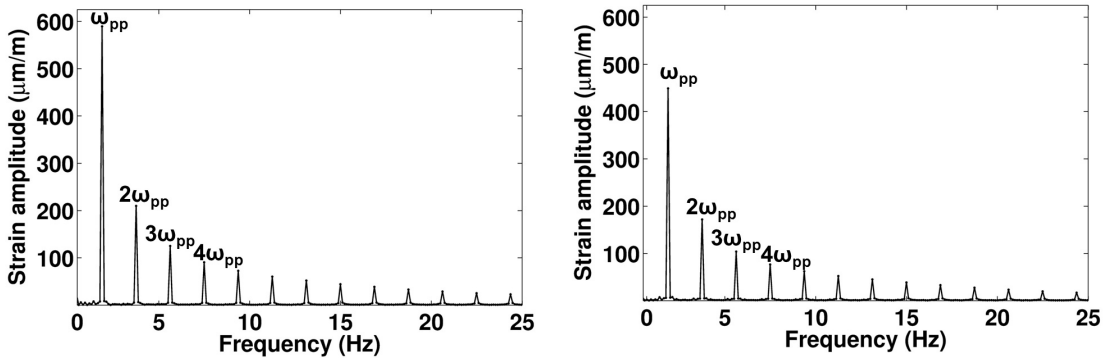

Figure 4.6: Spectra of experimental strain from the stage 1 ring on the W3600 gear train from the gauge: (a) closest to the free end (gauge 8) and (b) closest to the constrained end (gauge 1).

Figures 4.7(a) and 4.7(b) show the spectra of experimental strain (μm/m) from the free and constrained end of the stage 2 ring, respectively. Similar to the spectra for stage 1, peaks at multiples of planet pass frequency (nω_{pp} for n = 1, 2, 3...) can be observed.

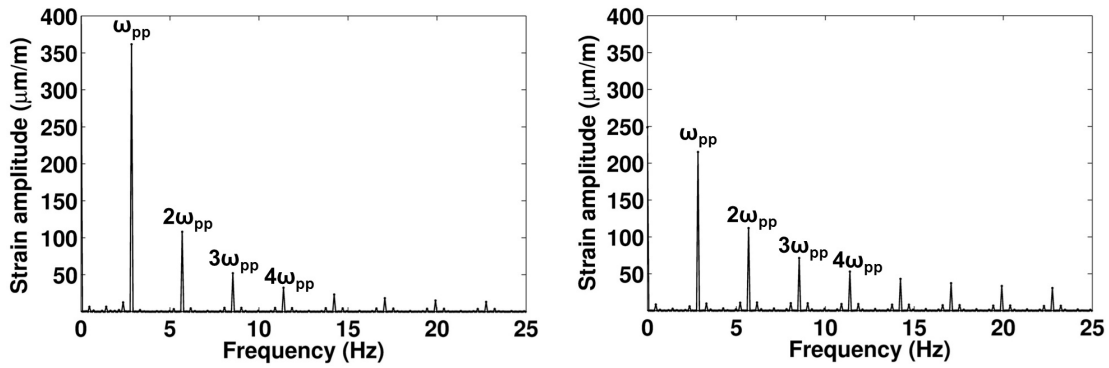

Figure 4.7: Spectra of experimental strain from the stage 2 ring on the W3600 gear train from the gauge: (a) closest to the free end (gauge 1) and (b) closest to the constrained end (gauge 8).

In addition to the peaks at multiples of planet pass frequency, a peak at mesh frequency and sidebands near planet pass frequency at plus or minus the frequency of the ring gear (ω_r) are present in the spectra (sidebands are present at $n\omega_{pp} \pm \omega_r$ where n = 1, 2, 3...). Figure 4.8(a) shows the spectra of experimental strain from the constrained end of the stage 2 ring near mesh frequency. A peak at mesh frequency is present in the spectra of each gauge. Figure 4.8(b) shows the frequency content from the constrained end of the stage 2 ring near planet pass frequency.

The presence of sidebands about the planet pass frequency at plus or minus the frequency of the ring gear indicates that the strain modulation observed at the constrained end of the stage 2 ring relates to a ring revolution. A rigorous discussion of sidebands and modulation observed in epicyclic gearbox vibration can be found in References [43–46].

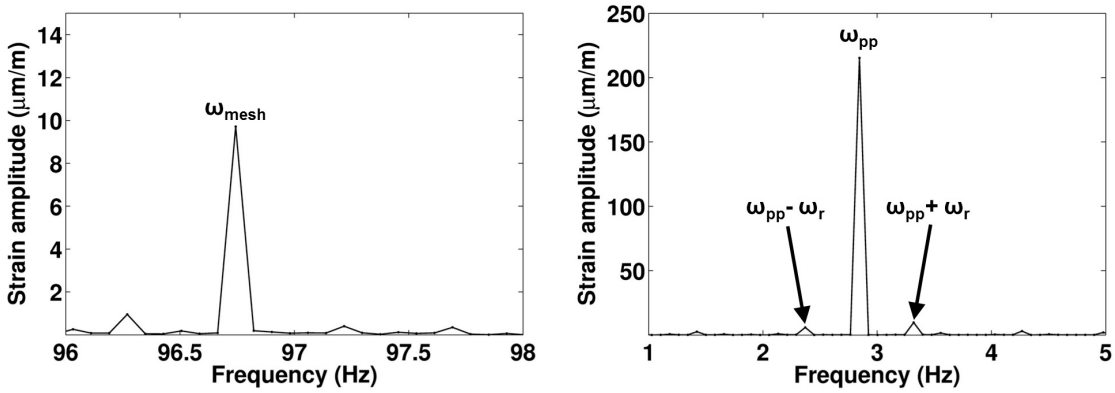

Figure 4.8: Spectra of experimental strain from the constrained end (gauge 8) of the stage 2 ring on the W3600 gear train near: (a) mesh frequency (ω_{mesh}) and (b) planet pass frequency (ω_{pp}).

As the literature suggests, it is believed that the asymmetry of the sidebands is due to the system parameters such as the number of ring teeth and planet spacing. Spectra of computational strain will be investigated in Chapter 5 and compared to the experimental frequency content. The presence of sidebands in the computational spectra will also be discussed.

4.3 W2000 Test Rig and Experimental Strain Data

Similar to the W3600, full scale experiments were conducted for the W2000 using a back-to-back, power circulating test rig configuration (shown in Figure 4.9). As discussed in [47], the main objectives were to install instrumentation on the system and obtain measurements of root strain in both ring gears across the tooth facewidths, sound intensity to evaluate radiated sound power, and noise and vibration levels at certain locations. Root strain across the facewidth of ring teeth will be correlated to

computational strain in this study. The gear train shown in Figure 4.9 is the slave gear train in the back-to-back test rig. The instrumented gear train is attached to this one (seen to the very left in Figure 4.9). The instrumented gear train is constrained along the outer diameter of the housing flange (shown in Figure 3.14) and also experiences the weight of the slave gear train that is attached to the very front of the main rotor shaft.

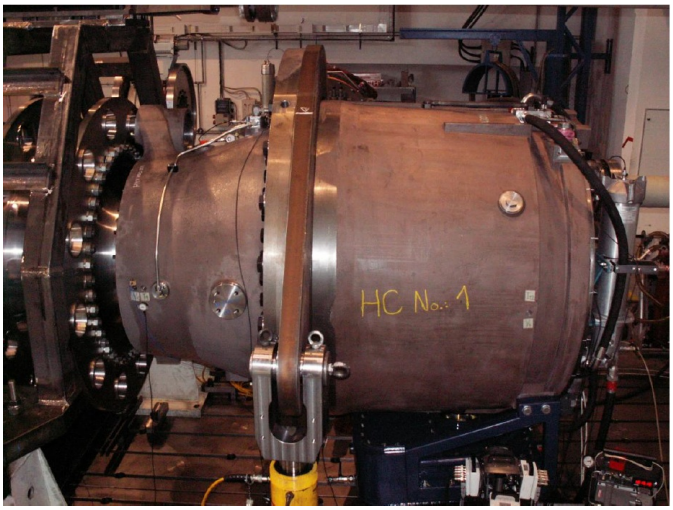

Figure 4.9: One gear train in the W2000 back-to-back, power circulating experimental test rig configuration [47].

Root strain is measured in the root of the ring teeth for each epicyclic stage. Two independent Bluetooth gear alignment modules in quarter bridge configuration were installed on each annulus 120 degrees apart. Balance weights were installed on the second stage ring gear to counterbalance the two gear alignment modules. Each module was mounted in a housing with two high capacity lithium thionyl batteries and attached to each ring gear. Figure 4.10(a) shows a gear alignment module mounted on

the stage 1 ring gear connected to strain gauges in the root covered with a protective white coating. Figure 4.10(b) shows a gear alignment module mounted on the stage 2 ring gear. This figure also shows the stage 1 sun connected to drive flange 2.

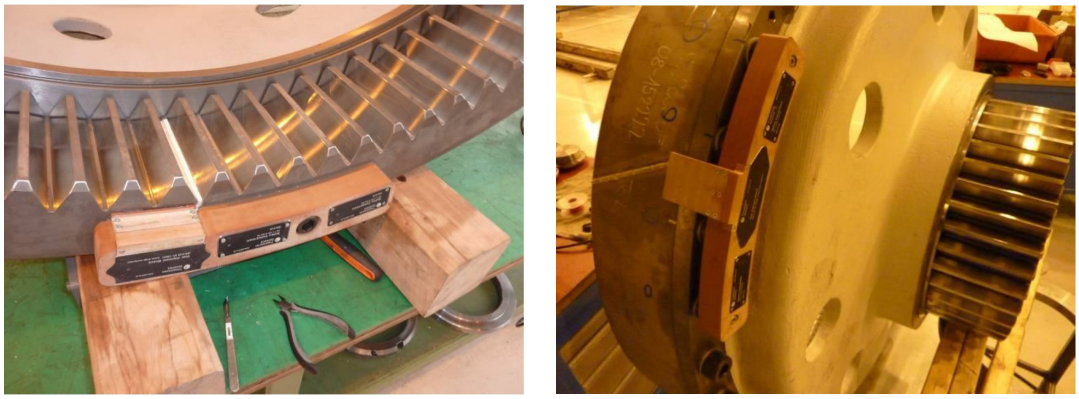

(a) (b)

Figure 4.10: (a) A gear alignment module connected to strain gauges in the root of the stage 1 ring gear covered with a protective white coating, and (b) gear alignment module mounted on the stage 2 ring gear.

Strain was measured at eight locations across the ring facewidths. Figures 4.11(a) and 4.11(b) show the strain gauge locations across the ring facewidth for stages 1 and 2, respectively. The free and constrained ends of the rings are labeled.

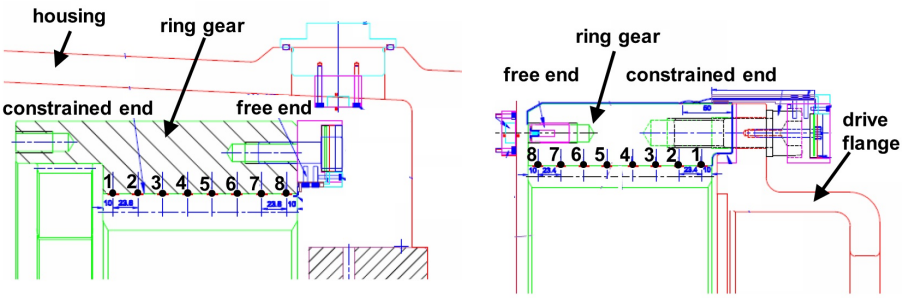

(a) (b)

Figure 4.11: W2000 strain gauge layout across: (a) the stage 1 ring facewidth, and (b) the stage 2 ring facewidth.

Data was collected during gear train operation for a range of different load regimes. As discussed in Chapter 3, comparisons in this study will be made for the nominal load regime that corresponds to 2,000 kW generator power and an output shaft speed of 1,798 rpm. Under this loading and speed regime, the strain signals were acquired at 625 Hz for the stage 1 modules and a sampling frequency of 2,500 Hz was used for the stage 2 modules. An output shaft speed of 1,798 rpm corresponds to a main rotor shaft speed of 15.7 rpm.

Experimental strain data from both rings shows a variation in peak-to-peak strain across the tooth facewidths. Figures 4.12(a) and 4.12(b) show experimental microstrain from the constrained and free end of the stage 1 ring, respectively. During testing, strain data from gauges 2 and 3 on stage 1 was unavailable. Similar to the W3600, stage 2 in particular exhibits a variation in strain across the facewidth. Towards the constrained end of the stage 2 ring, strain peaks show a rapid reversal in strain as a meshing planet passes the instrumented ring tooth. On the contrary, strain reversal due to mesh contact at the free end of the ring was exceeded by a

slower transient related to each passing planet. This phenomenon can be observed by comparing Figures 4.13(a) and 4.13(b) which show experimental microstrain from the constrained and free end of the stage 2 ring gear, respectively. The strain modulation seen at the constrained end of the stage 2 ring will be discussed further in Chapter 5. Experimental strain from all gauge locations is given in Appendix D.

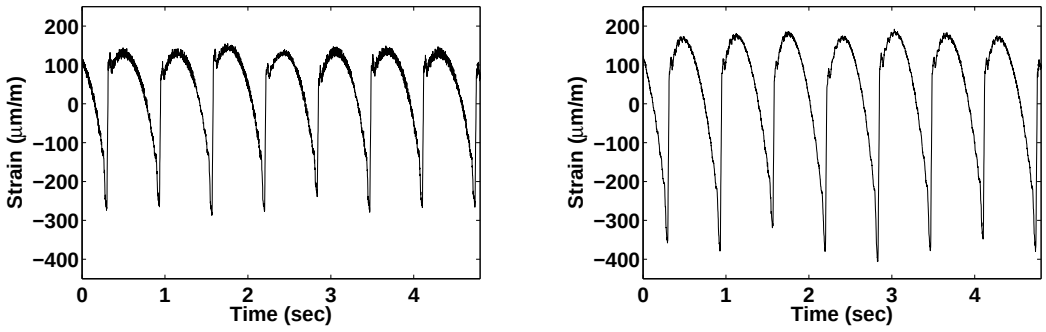

(a) (b)

Figure 4.12: Experimental strain from the stage 1 ring on the W2000 gear train from the gauge: (a) closest to the constrained end (gauge 1), and (b) closest to the free end (gauge 8).

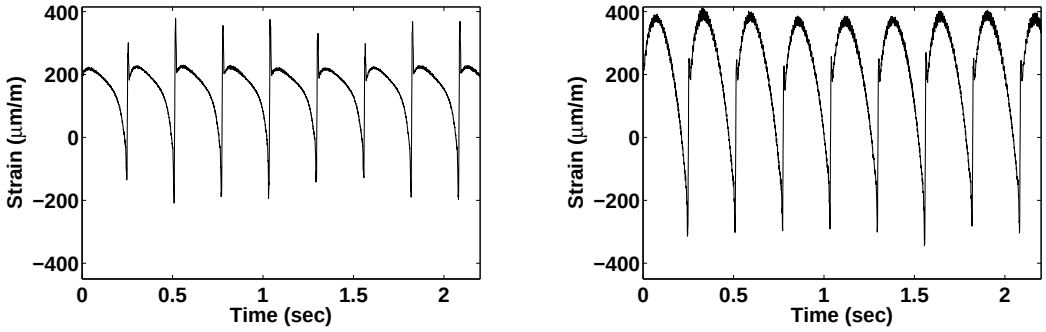

(a) (b)

Figure 4.13: Experimental strain from the stage 2 ring on the W2000 gear train from the gauge: (a) closest to the constrained end (gauge 1), and (b) closest to the free end (gauge 8).

Spectra from the free and constrained ends of both ring gears is investigated. Frequency content is calculated using the fast Fourier transform (FFT) algorithm. Figures 4.14(a)and 4.14(b) show the spectra from the free and constrained ends of the stage 1 ring gear, respectively. Peaks at multiples of planet pass frequency (nω_{pp} for n = 1, 2, 3...) are present.

Similarly, Figures 4.15(a)and 4.15(b) show the spectra from the free and constrained ends of the stage 2 ring gear, respectively. Sidebands are present at plus or minus the speed of the ring gear (ω_r) in the spectra from the constrained end of the stage 2 ring. This indicates that the strain modulation is related to the rotation of the ring gear. This will be investigated further in Chapter 5 using results from the finite element/contact mechanics model.

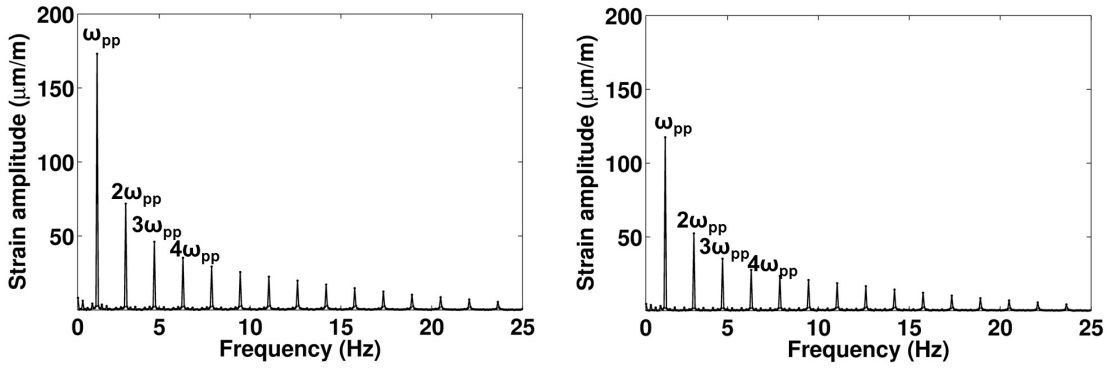

(a) (b)

Figure 4.14: Spectra of experimental strain from the stage 1 ring on the W2000 gear train from the gauge: (a) closest to the free end (gauge 8) and (b) closest to the constrained end (gauge 1).

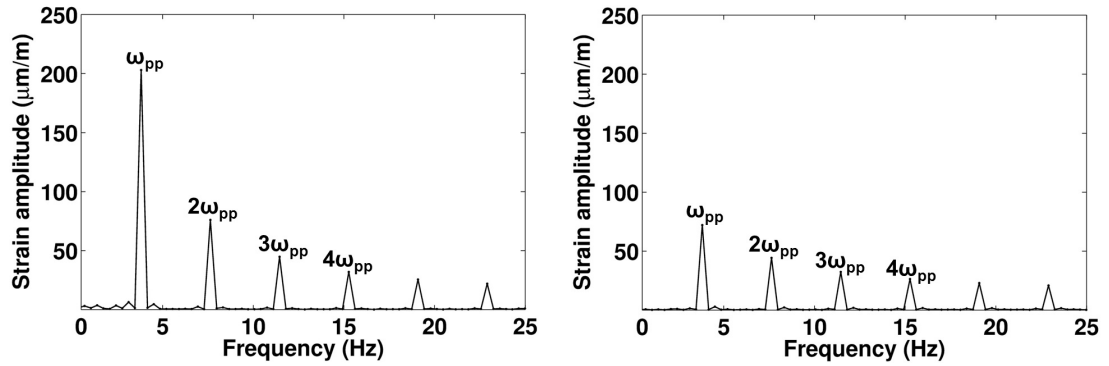

(a) (b)

Figure 4.15: Spectra of experimental strain from the stage 2 ring on the W2000 gear train from the gauge: (a) closest to the free end (gauge 8) and (b) closest to the constrained end (gauge 1).

4.4 FC5500 Test Rig and Experimental Strain Data

Similar to the other Orbital 2 gear trains, full system experiments were conducted on the FC5500 gear train. Eight strain gauges were installed along the roots of the

stage 1 and 2 ring gears and connected to Bluetooth gear alignment modules in quarter bridge configuration at two locations (180 degrees apart on each ring gear). The entire back-to-back, power circulating test rig configuration is shown in Figure 4.16. In this figure, the hydraulic cylinders attached to the external reaction arms on each gear train housing are visible. Like the W3600 gear train, these cylinders replicate the torque reaction system connected to the housing reaction arms during operation of the wind turbine.

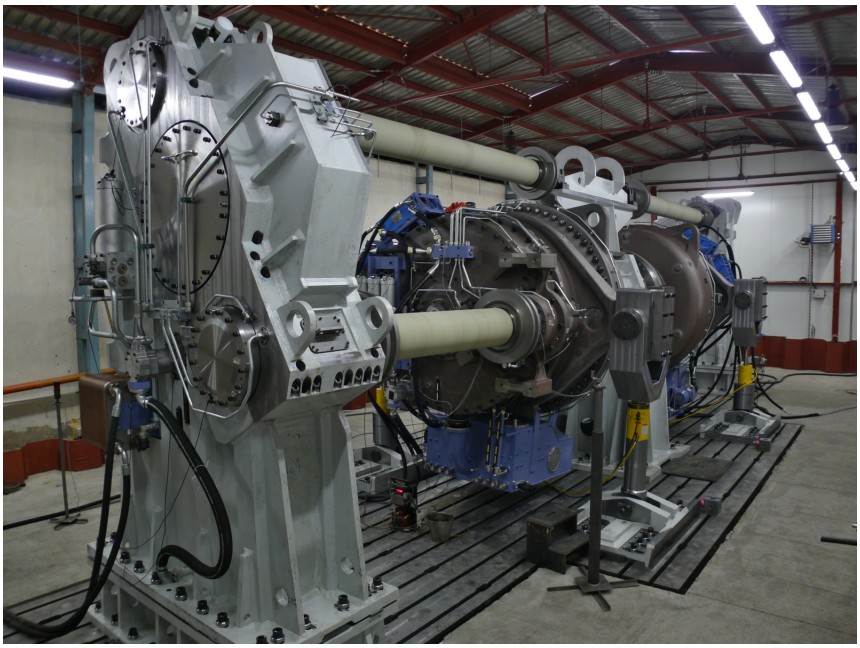

Figure 4.16: FC5500 back-to-back, power circulating experimental test rig configuration [48].

Figures 4.17(a) and 4.17(b) show the stage 2 planets being installed before testing and the hydraulic cylinder attached to an external housing reaction, respectively.

The hydraulic cylinders attached to the housing during testing simulate the torque reaction system that attaches to the gear train during operation.

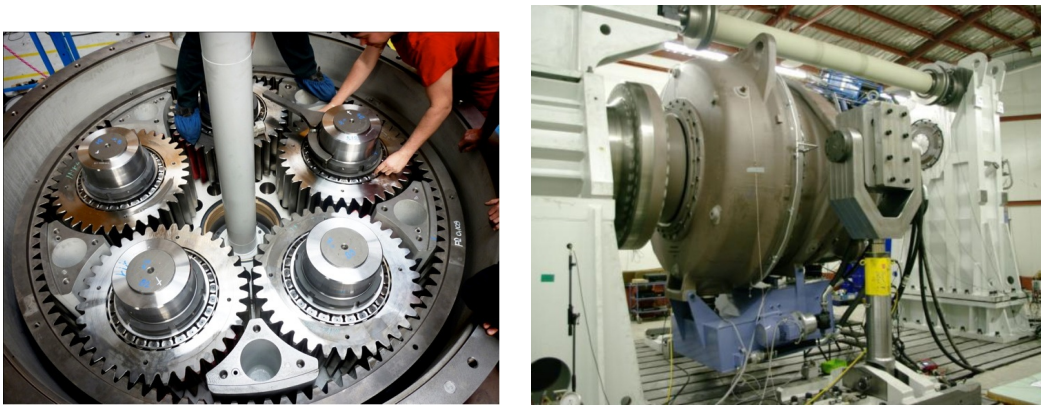

(a) (b)

Figure 4.17: (a) FC5500 stage 2 planets being installed before testing and (b) one gear train with hydraulic cylinder attached to external housing reaction arm.

Figures 4.18(a) and 4.18(b) show the stage 1 ring gear with gear alignment modules mounted on the annulus (installed at six and twelve o'clock) and strain gauges in the root of the stage 1 ring (connected to a gear alignment module), respectively. The gauges are covered with a protective white coating.

The locations of the strain gauges across the facewidth of the stage 1 and 2 ring gear are shown in Figures 4.19(a) and 4.19(b), respectively. On the stage 1 ring, the gauge closest to the constrained end is gauge 1 whereas the gauge closest to the constrained end of the stage 2 ring is gauge 8. The gauges are mounted in the bottom of the root and are 1.5 mm by 2 mm (in the profile and facewidth directions, respectively). Gauge position is accurate to within 1 mm in each direction.

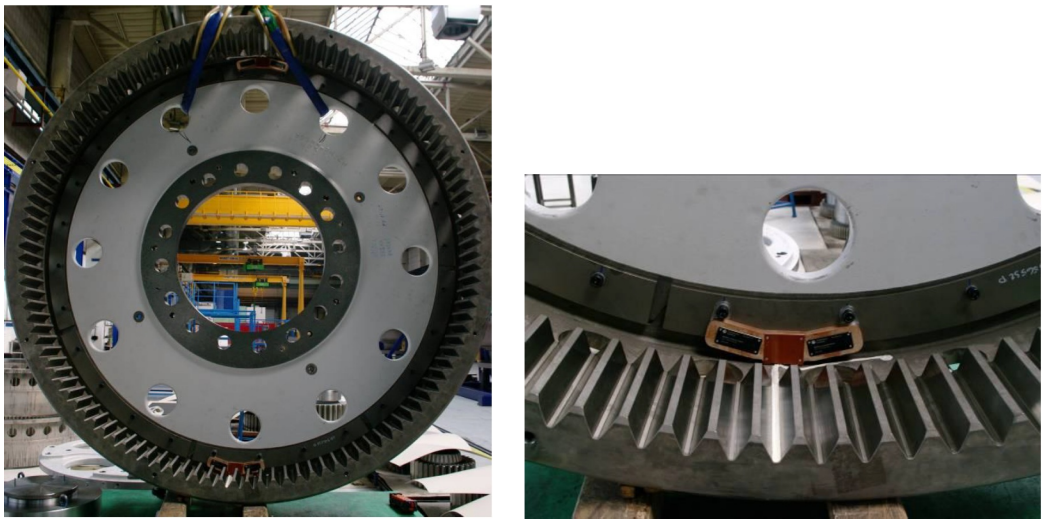

(a) (b)

Figure 4.18: (a) Stage 1 ring gear with gear alignment modules installed at six and twelve o'clock [48] and (b) Strain gauges in the root of the stage 1 ring gear connected to a gear alignment module (gauges covered with a protective white coating) [48].

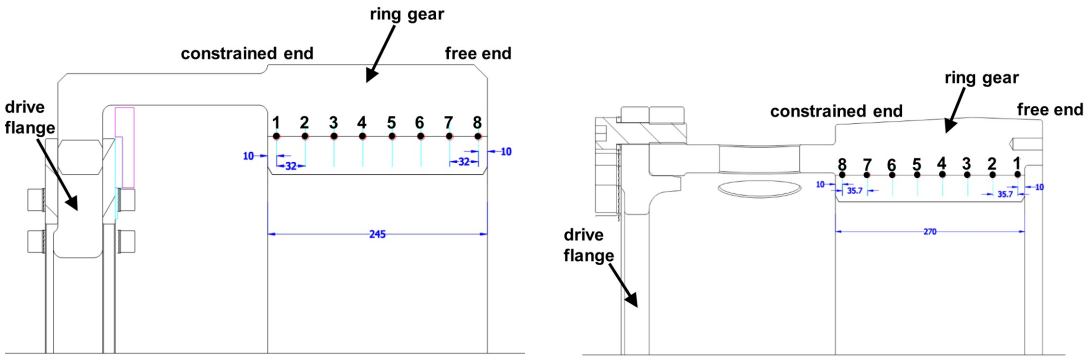

(a) (b)

Figure 4.19: FC5500 strain gauge layout across: (a) the stage 1 ring facewidth, and (b) the stage 2 ring facewidth.

Similar to the other gear trains discussed hitherto, the FC5500 experimental strain data indicates a variation in strain characteristics across the facewidth of the stage

2 ring gear. Rounded humps related to each passing planet are visible with rapid reversal in strain when an instrumented ring tooth meshes with a planet tooth. High frequency content stemming from tooth contact away from the strain gauges is also present in strain signals from both stages. Similar to the W3600, a distinct modulation can be observed in stage 2 strain signals. Figures 4.20(a) and 4.20(b) show strain from the free (gauge 1) and constrained (gauge 8) ends of the stage 2 ring, respectively.

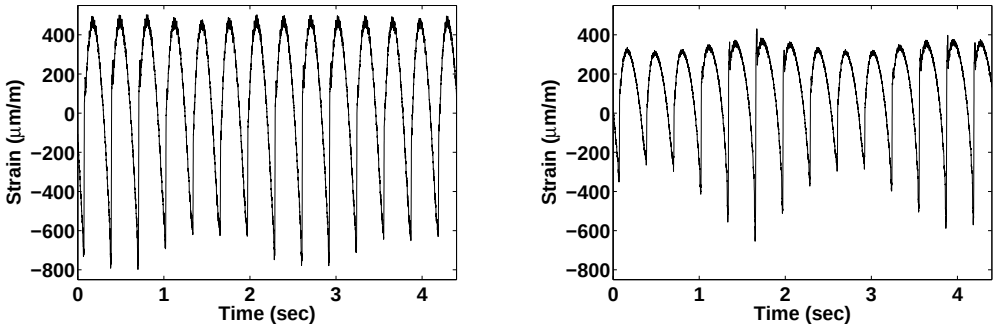

(a) (b)

Figure 4.20: Experimental strain from the stage 2 ring on the FC5500 gear train from the gauge: (a) closest to the free end (gauge 1), and (b) closest to the constrained end (gauge 8).

Similar to the W3600 experiments, the most distinct modulation occurs near the constrained end of the ring. The maximum peak-to-peak strain that occurs near the constrained end of the ring corresponds to the minimum peak-to-peak strain at the free end. This behavior was observed in the W3600 gear train and infers that two extremes of mesh inclination occur. This behavior is captured in the finite element/contact mechanics model and will be discussed further in Chapters 5 and 6.

Figures 4.21(a) and 4.21(b) show experimental strain from the free (gauge 8) and constrained (gauge 1) ends of the stage 1 ring, respectively. A slight modulation is present in the stage 1 strain signal and a variation in peak-to-peak strain is also observable (although not as drastic as the stage 2 strain data). The higher peak-to-peak strain occurs near the constrained end of the ring. The strain signal from gauge 8 seems shifted towards compression when compared to the data from gauge 1. This is likely due to gauge position error in the profile direction. Sensitivity to gauge location in the root will be investigated using computational strain from a finite element/contact mechanics model in Chapter 5.

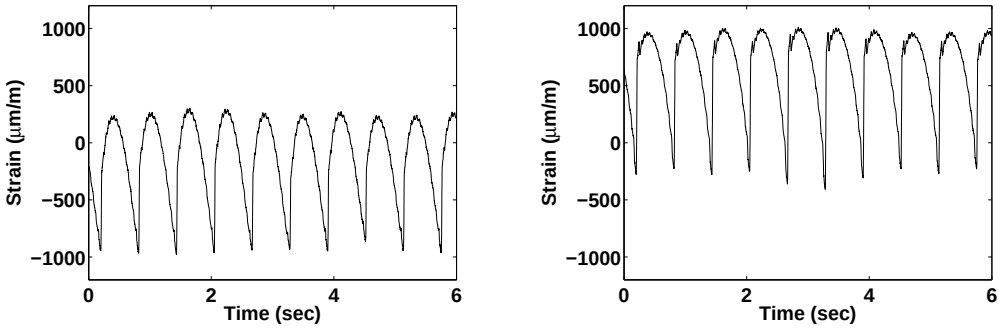

Figure 4.21: Experimental strain from the stage 1 ring on the FC5500 gear train from the gauge: (a) closest to the free end (gauge 8), and (b) closest to the constrained end (gauge 1).

During data acquisition, there was a problem with some of the strain gauges on both of the stage 1 modules. Module X only yielded data for gauges 1, 6, and 8. The strain shown above is from module X. Module D yielded data for gauges 2, 4, 5, 6, and 7. Experimental strain for each stage is given in Appendix D. The strain signals

shown in this appendix from stage 1 consist of data from both modules. Thus, data from gauges 2-7 comes from module D and data at each end comes from module X.

Figures 4.22(a) and 4.22(b) show spectra of experimental strain from the free (gauge 8) and constrained (gauge 1) ends of the stage 1 ring, respectively. Similar to the other gear trains, a distinct peak at the planet pass frequency (ω_{pp}) is present. Figures 4.23(a) and 4.23(b) show spectra of experimental strain from the free (gauge 1) and constrained (gauge 8) ends of the stage 2 ring. Sidebands at plus and minus the ring speed (ω_r) about multiples of planet pass frequency (nω_{pp} for n = 1, 2, 3...) are present near the constrained end of both stages, but particularly in the spectra from the constrained end of the stage 2 ring.

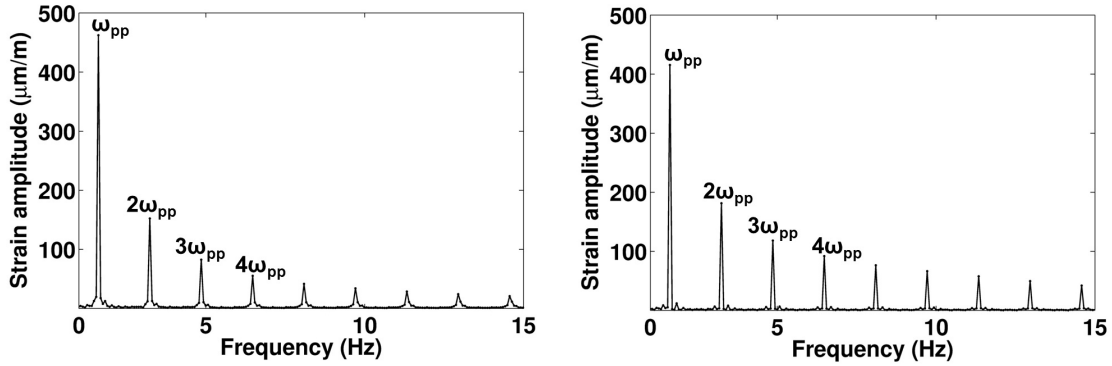

Figure 4.22: Spectra of experimental strain from the stage 1 ring on the FC5500 gear train from the gauge: (a) closest to the free end (gauge 8) and (b) closest to the constrained end (gauge 1).

As previously discussed for the other gear trains, the presence of these sidebands indicates that the modulation associated with the strain signal is related to the revolution of the ring gear. This specific behavior was observed in the stage 2 strain spectra from the W3600 gear train.

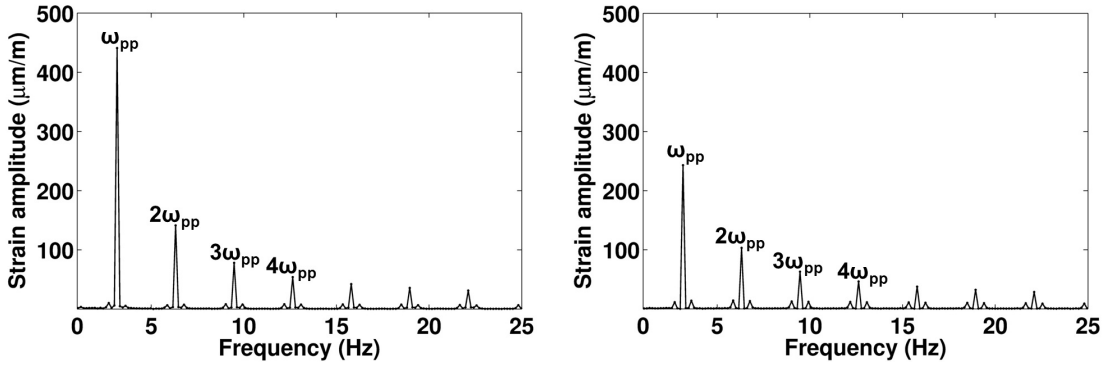

Figure 4.23: Spectra of experimental strain from the stage 2 ring on the FC5500 gear train from the gauge: (a) closest to the free end (gauge 1) and (b) closest to the constrained end (gauge 8).

Chapter 5: CALYX STRAIN DATA EXTRACTION AND CORRELATION TO EXPERIMENTS

5.1 Strain Data Extraction Using a Multyx Script

When analyzing full, three dimensional finite element/contact mechanics models of gear trains, computational efficiency is a concern. While Calyx can efficiently solve problems with elastic contact, the sheer size of the gear train models and the number of active meshes make simulations computationally intensive. A true strain signal (shown using experimental strain in Chapter 4) for a ring tooth on a planetary stage would require running that stage for many mesh cycles in order to get root strain readings for multiple planet passes. This is not practical for a large, three dimensional model. In this thesis, this each planetary stage is statically analyzed at 20 different configurations over one mesh cycle. It was determined that 20 steps were sufficient to capture peak-to-peak strain when a planet tooth meshes with a ring tooth. This was confirmed by running simulations with twice as many steps over a mesh cycle that yielded negligible difference in peak-to-peak strain.

The root strain the entire way around the ring gear is reconstructed using a simulation run over a mesh cycle. A Multyx script is constructed that extracts root strain from each ring tooth for each step. Figure 5.1 shows an example of a Multyx

script. The script consists of lines of text that cycle through Multyx post-processing menus to extract root strain and output it into a specified file.

```
SESFILENAME "session file name"
LOADSESSION
POSTPROC
POSTPROCFILENAME "post-processing file name"
OK
GOTOPOSN "step number"
POINTSTRAIN
OUTPUTTOFILE ON
FILENAME "output file name"
APPEND OFF
BEGINSTEP 1 ENDSTEP 1
COORD_TYPE SURFACE_COORDS
BODY "body name"
SURFACE "surface name"
TOOTHBEGIN 1 TOOTHEND 1
SPROF "location in profile direction (0 to 48)"
TFACE "location in facewidth direction (-1 to +1)"
REFDIRECTION "SPROF or TFACE"
ANGLE "angle in degrees measured clockwise from REFDIRECTION"
START
APPEND ON
TOOTHBEGIN 2 TOOTHEND 2 START
TOOTHBEGIN 3 TOOTHEND 3 START
 .
 .
 .

TOOTHBEGIN n TOOTHEND n START
```

Figure 5.1: Example of a Multyx script used to extract strain from the root of ring gear teeth.

This example of a Multyx script outlines the commands that must be specified in order to extract root strain from one gauge location. At the beginning of the file the session file name must be specified and then loaded. The POSTPROC command loads a menu where the post-processing file name must be specified. The POINTSTRAIN

command loads a menu where a number of parameters must be defined. The OUTPUTTOFILE command enables data to be output to the file given after the FILENAME command. The APPEND command either overwrites (APPEND OFF) or adds (APPEND ON) information to the output file. The starting and ending step are specified using BEGINSTEP and ENDSTEP. The COORD_TYPE command defines the type of coordinate system used. SURFACE_COORDS indicates that strain will be extracted based on definitions relative to the gear tooth surface.

The body, surface, and tooth number must also be defined. The SPROF and TFACE commands are used to define the location where strain is extracted in the profile and facewidth direction, respectively. As discussed in Chapter 2, SPROF ranges from zero to 48 and TFACE ranges from -1 to +1. The REFDIRECTION and ANGLE define the reference direction and angle (measured clockwise from the REFDIRECTION in degrees) along which normal stresses are computed. This POINTSTRAIN calculation is carried out for every tooth on the ring gear and then repeated for every step. The strain data is output to the same file and then reordered and pieced together using Matlab to form a strain signal around the ring gear. This process is repeated for every location where strain is desired on a ring tooth.

By extracting strain from the root of each tooth the entire way around the ring gear a strain signal is reconstructed that shows a strain peak for each strain gauge at each planet location. The result is a strain signal at each gauge location across the facewidth corresponding to a planet pass at each planet location. For instance, the W3600 stage 2 strain peaks correspond to a planet pass at the locations of the four different planets shown in Figure 5.2(a). Figure 5.2(b) shows the W3600 stage 2 ring gear root strain at the free end (gauge 1 from Figure 4.3(b)) at each planet location.

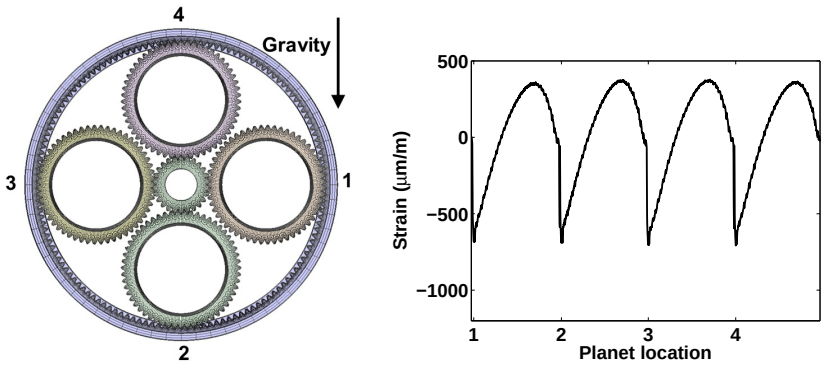

(a) (b)

Figure 5.2: (a) W3600 stage 2 planet locations and (b) strain peaks of gauge 1 corresponding to the planet locations shown in (a).

Strain from the stage 1 ring is extracted as described above for the stage 2 ring gear. A simulation is run that corresponds to one mesh cycle for the stage 1 planetary set, and the strain signal at each gauge location is reconstructed using a Multyx script as described above. Figure 5.3(a) depicts the planet locations, and Figure 5.3(b) shows the corresponding strain peaks for each planet pass for the gauge closest to the free end of the ring (gauge 8).

Sufficient mesh refinement is required on the ring teeth to accurately calculate root strains. As discussed in Chapter 2, the fine root mesh template is used on the ring gear teeth. The contact grid must also contain sufficient divisions in the facewidth direction. As outlined in Chapter 2, using the appropriate contact parameters such as number of face divisions is especially important in this study because variation in strain characteristics across the facewidth is examined. Gravity also becomes important when looking at the strain modulation seen in the W3600 stage 2 experimental data, for instance (shown in Figure 4.4(b)).

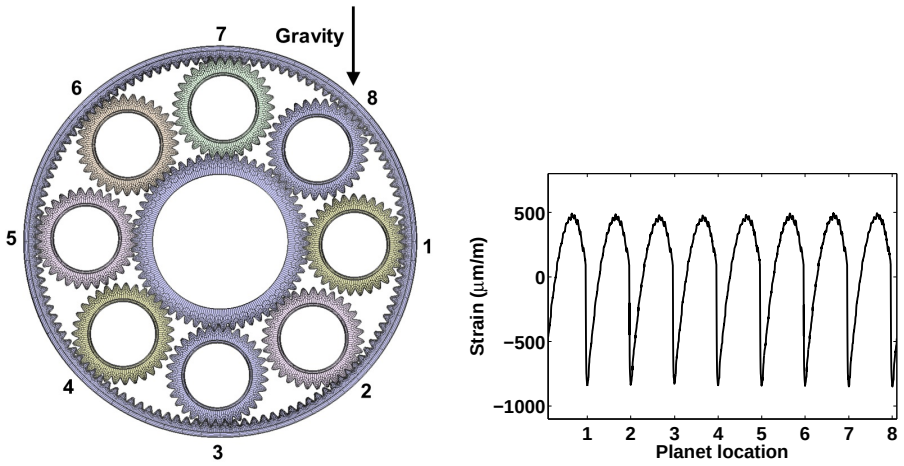

(a) (b)

Figure 5.3: (a) W3600 stage 1 planet locations and (b) strain peaks of gauge 8 corresponding to the planet locations shown in (a).

Root strain was analyzed in the same way for the W2000 and FC5500 models. Figures 5.4(a) and 5.4(b) show the planet locations used in the simulation over a stage 1 mesh cycle and the corresponding strain peaks from the free end of the stage 1 ring, respectively on the W2000 model. These strain peaks were constructed using a Multyx script as described above. Similarly, Figures 5.5(a) and 5.5(b) show the planet locations and corresponding strain peaks from the free end of the stage 2 ring, respectively on the W2000. These planet locations for each planetary stage correspond to the W2000 strain data discussed later in this chapter.

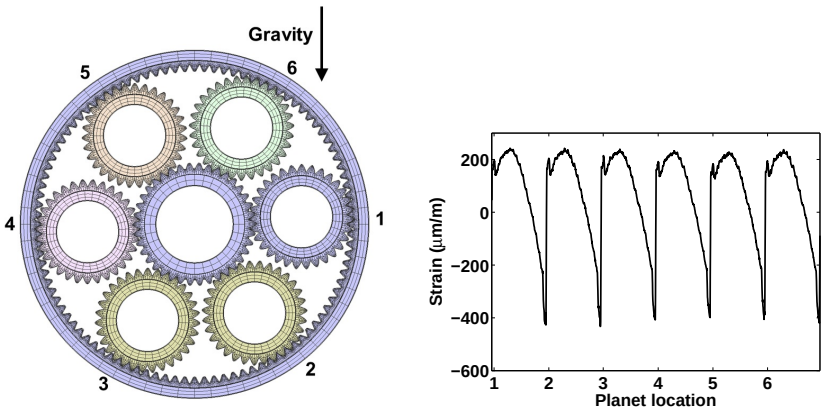

(a) (b)

Figure 5.4: (a) W2000 stage 1 planet locations and (b) strain peaks that correspond to the planet locations from the free end of the ring (gauge 8) shown in (a).

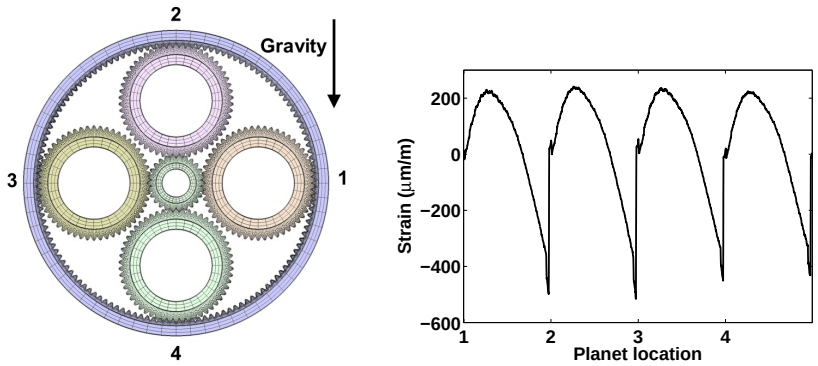

(a) (b)

Figure 5.5: (a) W2000 stage 2 planet locations and (b) strain peaks that correspond to the planet locations from the free end of the ring (gauge 8) shown in (a).

The following figures show the stage 1 and 2 planet locations and corresponding strain from the free end of each ring gear. Figures 5.6 and 5.7 show the planet locations and strain peaks from stage 1 and 2, respectively. Computational strain

peaks discussed later in this chapter were constructed using a Multyx script and correspond to these planet locations.

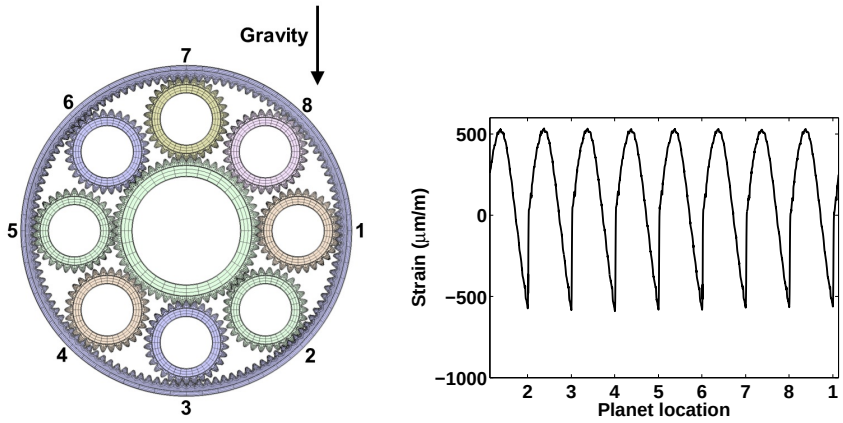

(a) (b)

Figure 5.6: (a) FC5500 stage 1 planet locations and (b) strain peaks of gauge 8 corresponding to the planet locations shown in (a).

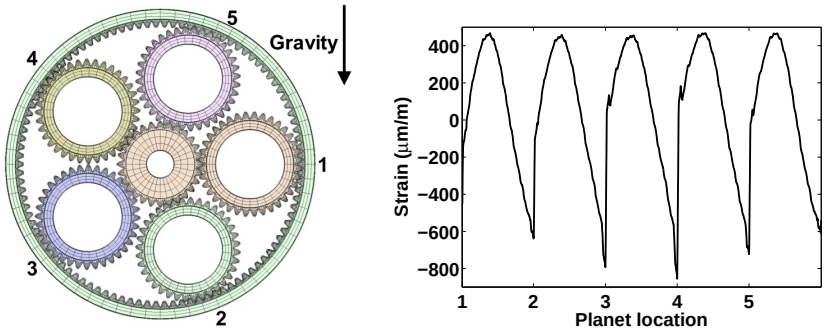

(a) (b)

Figure 5.7: (a) FC5500 stage 2 planet locations and (b) strain peaks of gauge 1 corresponding to the planet locations shown in (a).

5.2 W3600 Computational Strain Results

5.2.1 Strain Sensitivity

Strain sensitivity to gauge location is examined in this section. The strain gauges are 1.5 mm in the profile direction by 2 mm in the facewidth direction and placed in the bottom of the root. In the experiments, strain gauge position is accurate to within 1 mm in both the profile and facewidth directions. Because the strain gauges physically cover a region in the root and because strain is highly sensitive to position in the profile direction, strain from the finite element/contact mechanics model is averaged over three locations in the profile direction for each gauge. The computational strains are taken at the center of the strain gauge and at two other points corresponding to either end of the gauge. That is, strain is averaged over points at the bottom of the root and 3/4 mm each way in the profile direction. Looking at strain from each of these points separately illustrates that strain is highly sensitive to gauge position in the profile direction. Figure 5.8(a) shows the root on a ring gear in the finite element/contact mechanics model of the W3600 model. Figure 5.8(b) shows the three locations in the root of the stage 2 ring where strain is averaged. Gauge location A is 3/4 mm in the profile direction from location B, and gauge location C is 3/4 mm from location B in the opposite direction.

Figures 5.9(a), 5.9(b), and 5.9(c) show the strain peaks for each planet location as described above at gauge locations A, B, and C, respectively. Computational strain is not averaged over multiple positions in the facewidth direction because strain is not overly sensitive to gauge position in the this direction. Figure 5.9 illustrates the significance of the location of the gauge in the root. A gauge that is positioned 3/4 mm either way in the profile direction, still within the tolerance of gauge position,

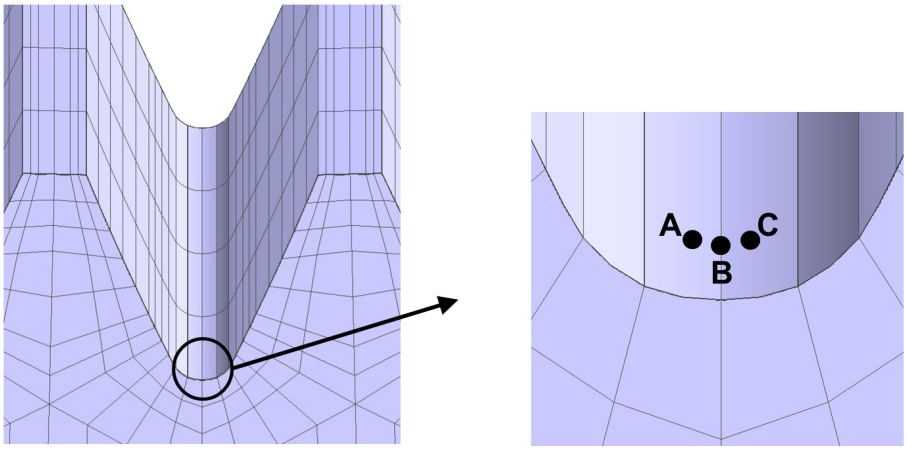

(a) (b)

Figure 5.8: (a) Root on a ring gear in the finite element/contact mechanics model and (b) locations in the root of the stage 2 ring where strain is extracted.

can yield strain curves that are shifted more towards tension or compression. This motivates the need to average strain over three locations in the profile direction and is important when correlating the computational strain results to experiments.

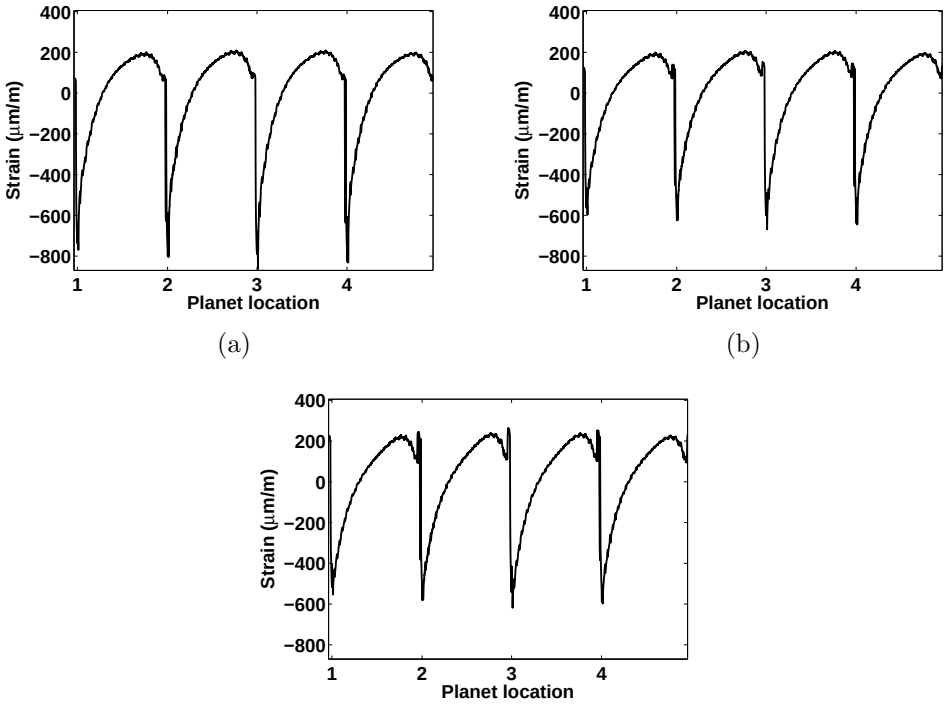

Figure 5.9: (a) Strain from gauge location A, (b) strain from gauge location B, and (c) strain from gauge location C.

5.2.2 Correlation to Experiments

The shape of the strain peaks from the finite element/contact mechanics model (Figures 5.10 and 5.11) and the experiments (Figures 4.4 and 4.5) match well. The experimental strain signal cannot be directly compared to experiments because the finite element model was run for one mesh cycle for each planetary stage. Strain peaks shown in Figures 5.10 and 5.11 correspond to the planet locations shown in Figures 5.3 and 5.2 for stages 1 and 2, respectively. The shapes and amplitudes of strain peaks that correspond to each plant location are analogous to experimental strain peaks at the same planet locations. The computational strain signal does not

resemble the experiments in number of planet passes because strain is not extracted from one instrumented tooth as in the experiments. In order to validate the use of a script to reconstruct root strain and to relate ring tooth location to peak-to-peak root strain, strain was extracted from one stage 2 ring tooth from the finite element/contact mechanics model for simulations run over a complete ring revolution. Strain modulation due to gravity and eccentricity is observed in these simulations and will be discussed further later in this chapter.

The stage 1 computational strain data matches the experiments well in that it lacks modulation in the strain signal and the peak-to-peak strains are comparable. Even though some of the computational strain peaks (Figures 5.10(a) and 5.10(b)) seem shifted toward either tension or compression when compared to experimental data (Figures 4.5(a) and 4.5(b)), this could be due to strain gauge position error in the root of the tooth, as discussed above. Figure 5.10(a) shows strain extracted from the Calyx model at the gauge location closest to the free end of the stage 1 ring, and Figure 5.10(b) shows strain from the gauge location closest to the constrained end of the stage 1 ring. These computational strain peaks indicate that the finite element model is behaving similarly to the gear train used to obtain experimental root strain, and in particular, the variation in strain characteristics across the facewidth of the stage 1 ring is captured. These strain peaks correspond to the planet locations in Figure 5.3.

Figure 5.11(a) shows strain from the finite element model at the gauge location closest to the free end of the stage 2 ring (gauge 1), and Figure 5.11(b) shows strain from the gauge location closest to the constrained end of the stage 2 ring (gauge 8). The stage 2 strain data from the constrained end of the ring (gauge 8) exhibits

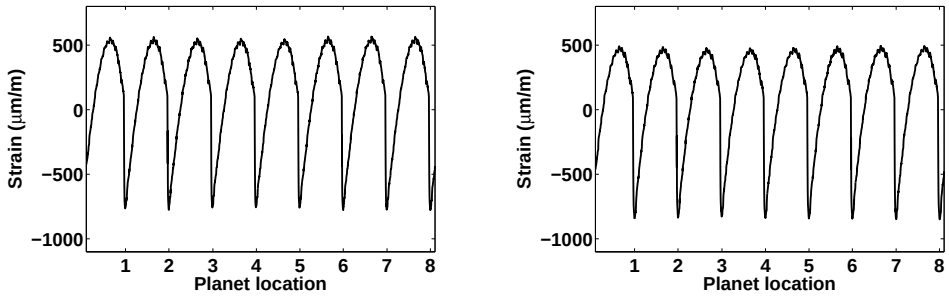

(a) (b)

Figure 5.10: (a) Finite element calculation of strain from the gauge closest to the free end of the W3600 stage 1 ring (gauge 8) and (b) strain from the gauge closest to the constrained end of the stage 1 ring (gauge 1).

a sharp spike and rapid reversal in strain when a passing planet meshes with a ring tooth (Figure 5.11(b)). This spike is not present near the free end of the ring (gauge 1) where the rapid reversal in strain due to mesh contact is exceeded by a slower transient related to the passing planet (Figure 5.11(a)). These strain peaks correspond to the planet locations depicted in Figure 5.2. This variation in strain characteristics across the gear facewidth is mainly attributed to the local deflection of the stage 2 ring and annulus (Figure 3.10(a)). During a planet pass, the free end of the ring deflects more than the constrained end in the radial direction causing an uneven load distribution across the facewidth of the ring. This is expected because of the added stiffness at the constrained end of the ring where the rim connects to the annulus and drive flange (Figure 3.10(a)).

5.2.3 Effects of Gravity and Model Deflections

Even though the finite element model is capturing the uneven load distribution across the facewidth of the stage 2 ring gear, it does not capture the modulation

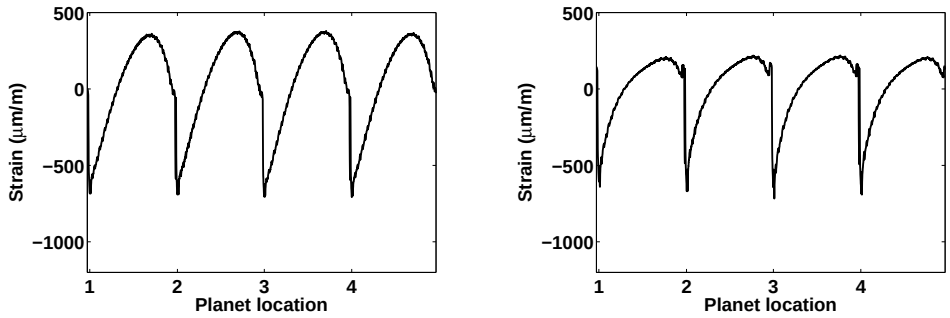

Figure 5.11: (a) Finite element calculation of strain from the gauge closest to the free end of the W3600 stage 2 ring (gauge 1) and (b) strain from the gauge closest to the constrained end of the stage 2 ring (gauge 8).

in strain observed over a carrier rotation near the constrained end of the ring in the experiments as seen in Figure 4.4(b). While a slight modulation exists in the computational strain, it is much less than the modulation in experimental strain. One contributing factor to this modulation is gravity. Because the gear train is cantilevered at the front as seen in Figure 3.7, gravity causes the back end to sag under its own weight. This causes the stage 2 ring and annulus to sag as well. The weight of the ring and annulus adds to the ring-planet mesh force at planet location 3 and subtracts from the ring-planet mesh force at planet location 1. The largest strain peak corresponds to planet location 3 as described in Figure 5.2, and the smallest strain peak occurs at planet location 1. It is for this reason that including gravity in the model is essential in order to accurately capture system deflections.

It is not known what planet pass location corresponds to the minimum and maximum experimental strain peaks for the strain gauge closest to the constrained end of the stage 2 ring. It is reasonable to assume that the maximum occurs at planet

location 3 and the minimum occurs at planet location 1, as shown in Figure 5.2. The location of the planets with respect to gravity is important when trying to understand the modulation. Simulations with and without eccentricity run over a ring revolution will be discussed in later in this chapter and provide insight into the relationship between the instrumented ring tooth location and peak-to-peak strain. The contribution of gravity and eccentricity to strain modulation will be investigated. These simulations confirm that the minimum peak-to-peak strain occurs near planet location 1 and the maximum peak-to-peak strain occurs three planet passes later near planet location 3.

Figure 5.12(a) shows a cutaway view of the stage 1 sun-stage 2 ring subassembly, and Figure 5.12(b) shows the same view with exaggerated deformation. The horizontal lines represent the central axis of the undeformed gearbox. The stage 2 ring and annulus rigidly deflect in the direction of gravity. The stage 2 carrier and planets do not deflect as much in the direction of gravity because the stage 2 carrier is connected to the main rotor shaft that is supported at the front of the gearbox as shown in Figure 3.7. This is significant because it supports the idea that the deflection of the ring increases the strain peak at planet location 3 and decreases the strain peak at planet location 1.

Figure 5.13 explains this further by showing the instantaneous contact pressure patterns at the ring-planet meshes at planet locations 1 and 3. At planet location 1, when the ring deflects in the direction of gravity, it decreases the load at the ring-planet mesh because contact is on the top of the ring tooth (contact force is primarily downward on the ring tooth). At planet location 3, the ring deflection in the direction of gravity increases the load at the ring-planet mesh because the

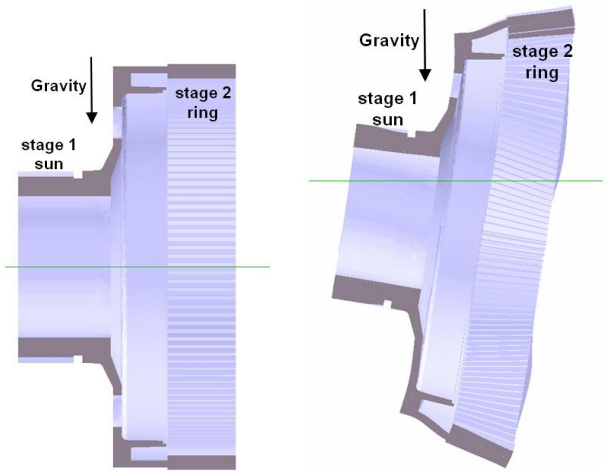

(a) (b)

Figure 5.12: Cutaway view of the stage 1 sun-stage 2 ring subassembly: (a) undeformed, and (b) with exaggerated deformation.

contact is on the bottom of the ring tooth (contact force is primarily upward on the ring tooth). Thus, the maximum peak-to-peak strain when a planet tooth meshes with a ring tooth occurs near planet location 3, and the minimum peak-to-peak strain occurs near planet location 1. The instantaneous contact pressure patterns shown in Figures 5.13(a) and 5.13(b) also illustrate that the stage 2 ring teeth are loaded more towards the constrained end. This is also reflected in the computational strain from each end of the ring during a planet pass as shown in Figure 5.11, with more pronounced spikes in strain occurring at the constrained end.

Examining tangential bearing reaction forces of the stage 2 planets further indicates that gravity contributes to the modulation in strain and influences planet load sharing. Figure 5.14(a) shows the tangential bearing reaction forces of the stage 2 planets for the model without gravity, and Figure 5.14(b) shows the reaction forces for the model with gravity included. For the model without gravity, there is little

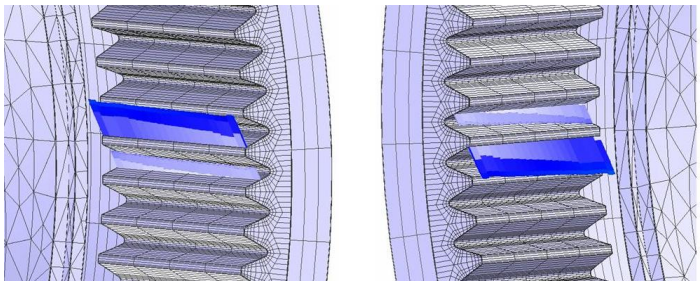

(a) (b)

Figure 5.13: (a) Instantaneous contact pressure forces on the stage 2 ring at (a) planet location 1 and (b) planet location 3.

difference in planet bearing reaction forces. For the model with gravity included, the planet at location 1 yields the lowest bearing reaction force, and the planet at location 3 yields the highest bearing reaction force. These bearing reaction forces are consistent with the minimum and maximum root strain peaks that occur near the constrained end of the stage 2 ring during a planet pass at these planet locations. The model without gravity exhibits negligible modulation in strain at any gauge location across the ring facewidth.

5.2.4 Carrier Eccentricity

The modulation from the finite element/contact mechanics model is not as drastic as the experimental strain at the constrained end of the stage 2 ring. For this reason, stage 2 carrier eccentricity is considered. In Calyx, eccentricity can be applied two ways. Pin position error can be applied in the same direction to the planet pins to simulate eccentricity of the carrier relative to the main rotor shaft to which it is connected. Figure 5.15 shows an example of four planets being translated in the upward direction. This is implemented by defining a magnitude of displacement and

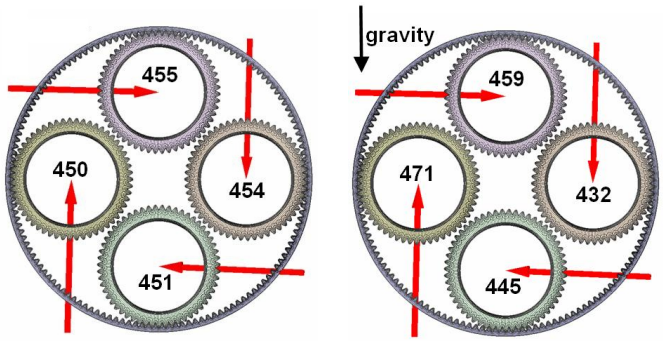

(a) (b)

Figure 5.14: W3600 tangential bearing reaction forces (kN) of the stage 2 planets for: (a) the model without gravity, and (b) the model with gravity.

angle (in degrees) measured counter-clockwise about the z axis of the rotor, relative to the radial direction for each planet group in the Multyx pin position error menu. For example, in order to translate the planet located at six o'clock in this figure in the upward direction, an angle of 180 degrees is specified.

Main rotor shaft and stage 2 carrier eccentricities relative to the housing are modeled using unloaded deformation applied to the bearings that connect the main rotor shaft and the stage 2 support plate to the housing (both bearing connections shown in Figure 5.16). Even though the planets rotate with the carrier, they rotate very little with respect to gravity over one mesh cycle. Hence, planet pin position and main rotor shaft eccentricities yield similar results when running a simulation over one mesh cycle. Looking at peak-to-peak strain over a ring revolution provides some insight into the more likely type of eccentricity and will be discussed further. The most likely type of eccentricity is main rotor shaft eccentricity relative to the housing because it gives a modulation that agrees with the experiments.

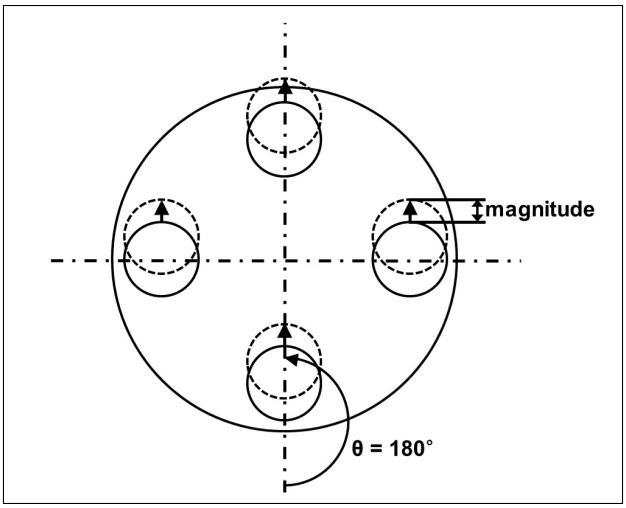

Figure 5.15: Implementation of planet pin position error in the finite element/contact mechanics model.

Eccentricity discussed henceforth for the W3600 refers to eccentricity of the stage 2 carrier and main rotor shaft (applied to the finite element model using unloaded bearing deformation). Different values of main rotor shaft eccentricity are investigated in the direction opposite gravity. This simulates downward deflection of the housing (relative to the main rotor shaft) that could occur in the actual system due to bearing clearances. It was determined that as the carrier eccentricity in this direction increases, the modulation in strain near the constrained end of the stage 2 ring becomes more significant. Eccentricities of 100, 200, 400, 500, and 1000 μm are investigated. These are reasonable values given the size of the gear train. Figures 5.17(a) and 5.17(b) show computational strain from the free and constrained end of the stage 2 ring, respectively, with 200 μm carrier eccentricity in the direction opposite to gravity. Similarly, Figures 5.17(c) and 5.17(d) show strain from the same location but with 500 μm carrier eccentricity in the same direction.

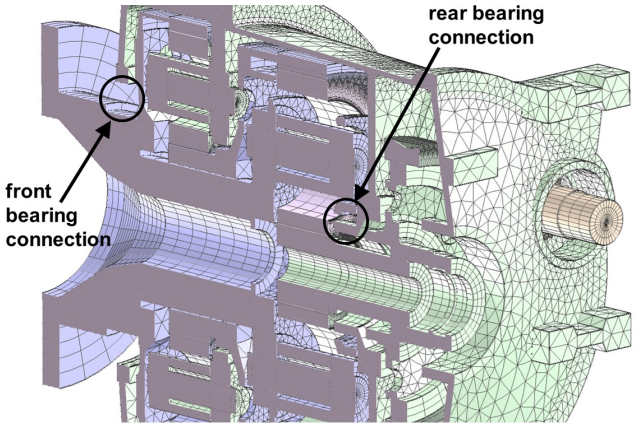

Figure 5.16: Two bearing connections given unloaded deformation to simulate eccentricity that connect the main rotor shaft and the stage 2 carrier to the housing in the W3600 model.

Figure 5.17 indicates that introducing eccentricity in the finite element/contact mechanics model in the direction opposite gravity indeed enhances the strain modulation at the constrained end of the stage 2 ring. The minimum peak-to-peak strain occurs during a planet pass at planet location 1, and the maximum peak-to-peak strain occurs during a planet pass at planet location 3. As eccentricity is increased, modulation increases. Furthermore, the planet location that yields the minimum peak-to-peak strain during a planet pass at the constrained end of the ring corresponds to the planet location that yields a maximum peak-to-peak strain during a planet pass at the free end of the ring and vice versa. This is consistent with the experimental strain data shown in Figure 5.18 (as shown in Chapter 4). Peak-to-peak strain and the general shapes of the computaional strain signals are consistent with the experiments.

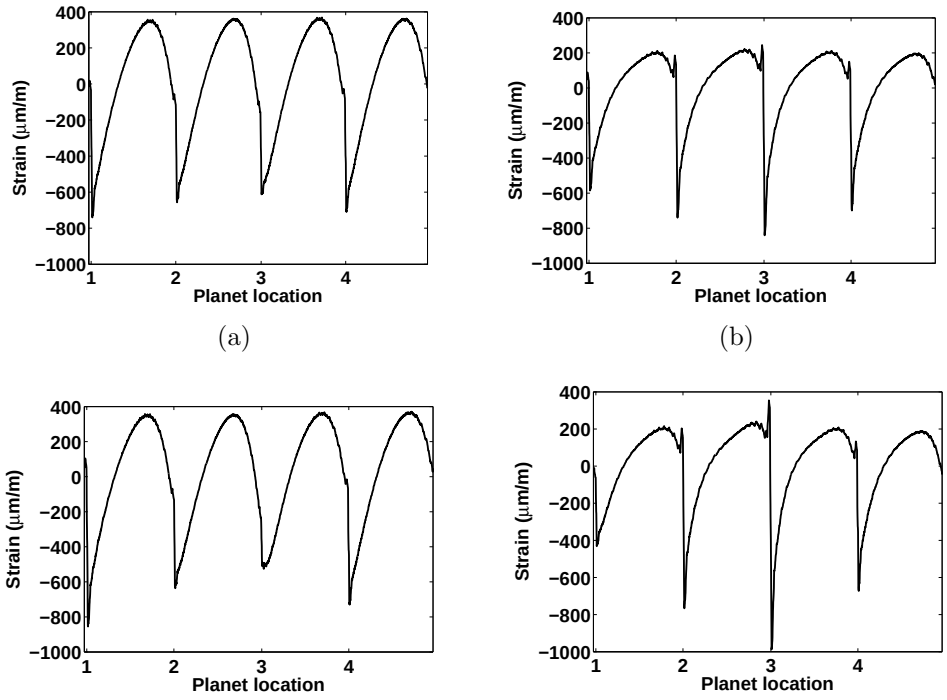

Figure 5.17: Finite element calculation of stage 2 ring tooth root strain with (a) 200 μm eccentricity at the free end (gauge 1) (b) 200 μm eccentricity at the constrained end (gauge 8) (c) 500 μm eccentricity at the free end (gauge 1) (d) 500 μm eccentricity at the constrained end (gauge 8).

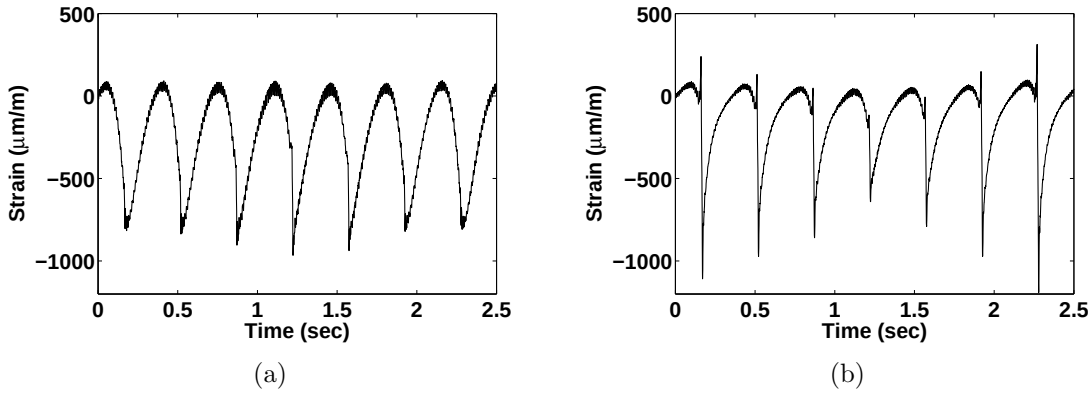

Figure 5.18: Experimental strain from the stage 2 ring on the W3600 gear train from the gauge: (a) closest to the free end (gauge 1) and (b) closest to the constrained end (gauge 8).

As seen in Figure 5.17, during a planet pass, planet location 1 yields the minimum peak-to-peak strain at the constrained end and the maximum peak-to-peak strain at the free end. Planet location 3 yields the maximum peak-to-peak strain at the constrained end and minimum peak-to-peak strain at the free end. This observation is supported further in Figures 5.19(a) and 5.19(b), which show the instantaneous contact force at planet location 1 and 3, respectively on the finite element model with 500 μm eccentricity opposite gravity. It can be seen that the ring tooth at planet location 1 is loaded more towards the free and the ring tooth at planet location 3 is loaded more towards the constrained end. This is consistent with Figures 5.17(c) and 5.17(d).

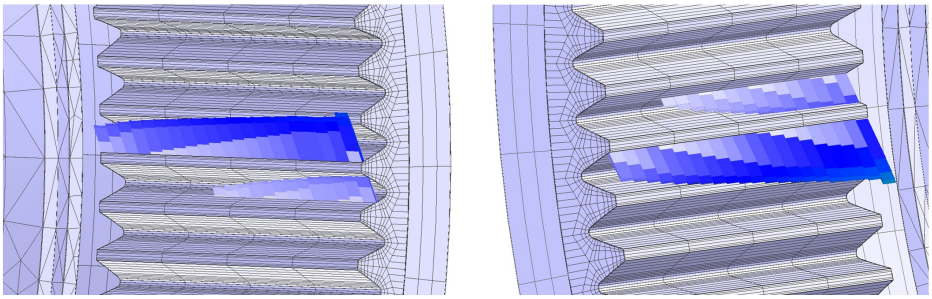

(a) (b)

Figure 5.19: W3600 instantaneous contact pressure forces on the stage 2 ring from the model with 500 μm eccentricity at (a) planet location 1 and (b) planet location 3.

Figures 5.20(a) and 5.20(b) show stage 2 tangential bearing reaction forces for the model with 200 μm and 500 μm carrier eccentricity in the direction opposite to gravity. It can be seen that as eccentricity increases, the difference between the minimum and maximum bearing reaction forces at planet locations 1 and 3 also increases. These

results are consistent with root strain behavior. The larger the difference in the planet bearing reaction forces at locations 1 and 3, the larger the difference in peak-to-peak strain during a planet pass at locations 1 and 3 near the constrained end of the ring.

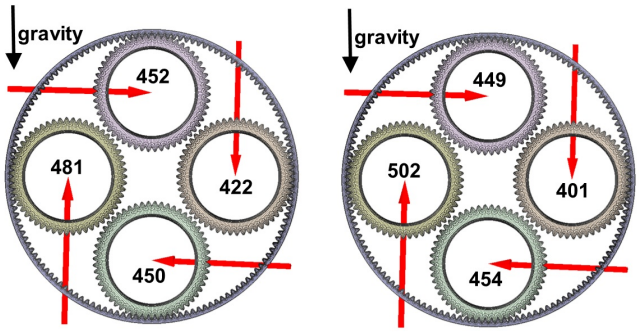

(a) (b)

Figure 5.20: W3600 tangential bearing reaction forces (kN) of the stage 2 planets for: (a) the model with 200 μm eccentricity, and (b) the model with 500 μm eccentricity.

In order to relate carrier eccentricity in the direction opposite to gravity and strain modulation at the constrained end of the ring, eccentricity versus the difference in maximum and minimum peak-to-peak strain during a planet pass is plotted in Figure 5.21. As seen in Figure 5.21, carrier eccentricity definitely contributes to modulation.

In order to better understand the strain modulation observed in both the experiments and the finite element model and to verify the use of a script to extract root strain, two simulations were run over a stage 2 ring revolution (one with no eccentricity and one with 500 μm eccentricity in the direction opposite gravity). In the interest of computational efficiency, 20 time steps were used in between each planet pass. Strain was extracted from one ring tooth to replicate the instrumented tooth

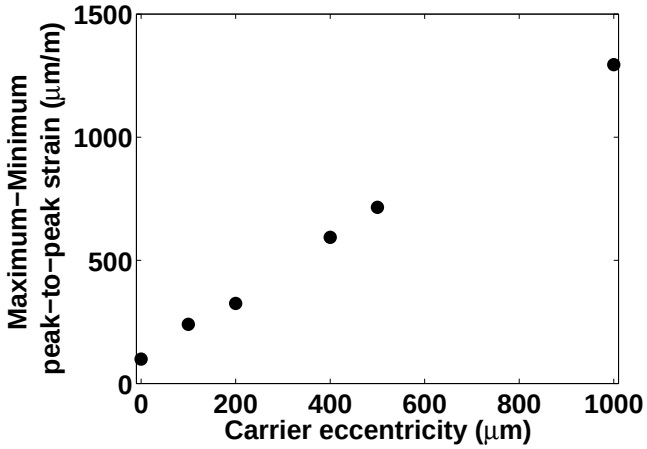

Figure 5.21: Finite element calculation of maximum-minimum peak-to-peak strain at the constrained end of the stage 2 ring during a planet pass for varying carrier eccentricity.

in the experimental setup. Even this relatively low number of time steps over a ring revolution illustrates the modulation in strain near the constrained end of the stage 2 ring for both cases. Figures 5.22(a) and 5.22(c) show the computational root strain from the constrained end of the stage 2 ring over a ring revolution with no eccentricity and 500 μm eccentricity in the direction opposite gravity, respectively. The peaks corresponding to planet locations 1 and 3 (as shown in Figure 5.2(a)) are labeled. These figures support the idea that gravity contributes to strain modulation and that carrier eccentricity enhances it. These simulations verify that the minimum and maximum strain peaks occur near planet locations 1 and 3, respectively and confirm that the finite element model is capturing strain modulation similar to what was observed in the experiments. As seen in the experiments, the modulation repeats every six planet

passes which corresponds to the number of planets that mesh with the instrumented ring tooth over a ring revolution.

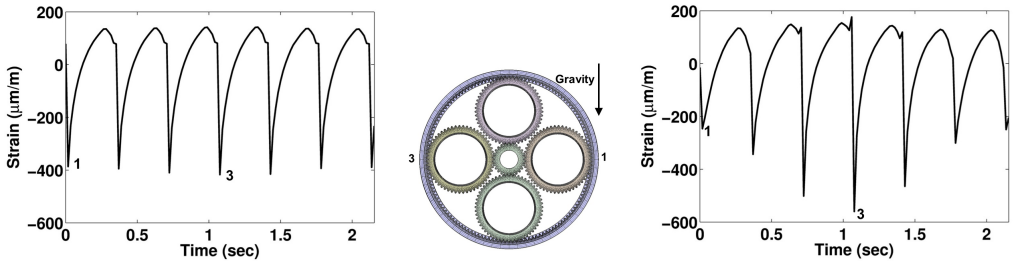

(a) (b) (c)

Figure 5.22: (a) Finite element calculation of strain from the constrained end of one tooth on the stage 2 ring over a ring revolution in the W3600 model with no eccentricity, (b) plant locations 1 and 3, and (c) finite element calculation of strain from the constrained end of one tooth on the stage 2 ring over a ring revolution with 500 μm eccentricity.

A discrete Fourier transform (DFT) of computational strain ($\mu m/m$) from the constrained end of the stage 2 ring was calculated using the fast Fourier transform (FFT) algorithm for the simulation over a ring revolution with 500 μm eccentricity. As noted in Chapter 4, sidebands are present in the spectra of experimental strain from the constrained end of the stage 2 ring. Similar to the experimental spectra, the computational spectra also exhibits sidebands about multiples of planet pass frequency (ω_{pp}) at plus or minus the ring frequency (ω_r).

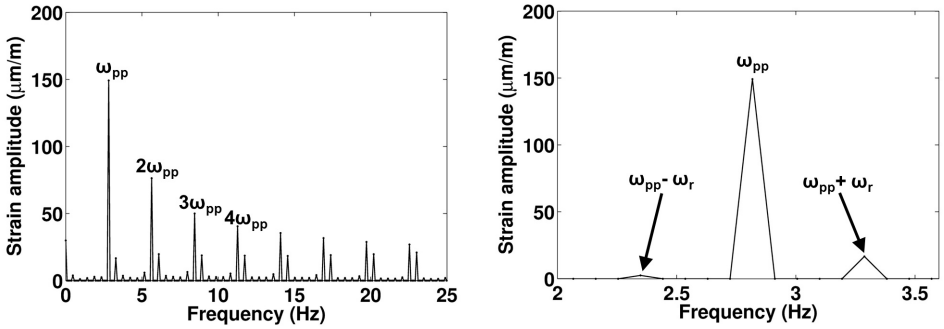

(a) (b)

Figure 5.23: Spectra of computational strain from the constrained end of the W3600 stage 2 ring showing (a) peaks at multiples of planet pass frequency (ω_{pp}) and (b) peak at planet pass frequency with sidebands at ± ring speed (ω_r).

These sidebands about planet pass frequency are present in both the experimental and computational results, confirming that strain modulation relates to the revolution of the instrumented ring tooth relative to the planets, gravity and carrier eccentricity and that the finite element/contact mechanics model is capturing the strain modulation observed in the experimental strain data at the constrained end of the stage 2 ring.

5.3 W2000 Computational Strain Results

The root strain data extraction from the finite element/contact mechanics model of the W2000 system was performed in the same manner as described for the W3600 system. Simulations for each planetary stage were run for one mesh cycle and root strain was then extracted using a script from each ring tooth the entire way around the ring. Strain at each gauge location was averaged over three locations in the profile direction representing the middle and each end of the gauge itself. This strain data

gives peak-to-peak strain at the specific planet locations that will be described in the next section. These peak-to-peak values can be compared to experiments because a sufficient number of steps (twenty) was used over the mesh cycle. In order to examine strain variation across the ring facewidth, a sufficient number of contact grid cells was used in the facewidth direction in both epicyclic stages.

5.3.1 Correlation to Experiments

In general, root strain from stages 1 and 2 matches experimental values well. The finite element/contact mechanics model captures variation in strain across ring facewidths. The overall shape of strain curves during a planet pass and peak-to-peak values correlate with experiments well. The constrained ends of both rings exhibit a sharper peak than at the free end when a planet meshes with a ring tooth. Similar to the W3600, this can be attributed mainly to the differing constraints at each end. Similar to the ring gears in the W3600 system, the constrained end is stiffer than the free end due to the connection to the annulus. This causes non-uniform deflection in the radial direction and leads to variation in strain characteristics across the ring facewidths.

Figures 5.24(a) and 5.24(b) show stage 1 computational strain from the free (gauge 8) and constrained (gauge 1) end of the ring, respectively. Strain peaks correspond to the planet locations given in Figure 5.4. These strain values can be compared to experimental strain shown in Figures 4.12(b) and 4.12(a) (from the free and constrained end of the ring, respectively) given in Chapter 4.

It can be seen that strain from the constrained end of the stage 1 ring exhibits more pronounced peaks when a planet tooth meshes with a ring tooth. Moving across the

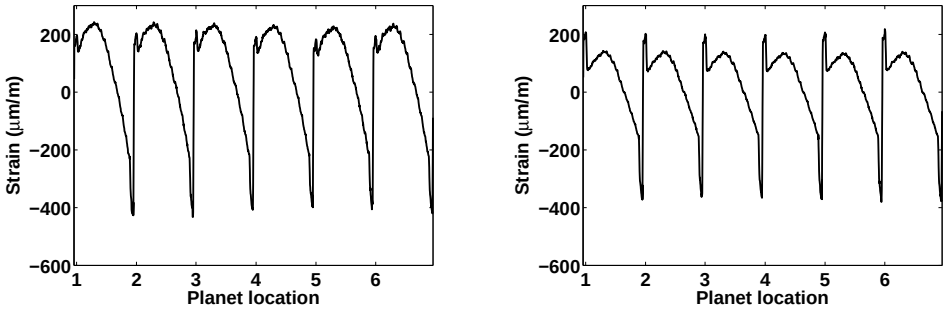

(a) (b)

Figure 5.24: (a) Strain from the gauge closest to the free end of the W2000 stage 1 ring, and (b) Strain from the gauge closest to the constrained end of the stage 1 ring.

facewidth towards the free end yields gradually less pronounced peaks. This behavior is consistent with the experimental data.

Figures 5.25(a) and 5.25(b) show strain from the free (gauge 8) and constrained (gauge 1) ends of the stage 2 ring, respectively. The strain peaks correspond to the planet locations described in Figure 5.5. Figures 5.25(a) and 5.25(b) can be compared to experimental strain shown in Figures 4.12(b) and 4.12(a), respectively.

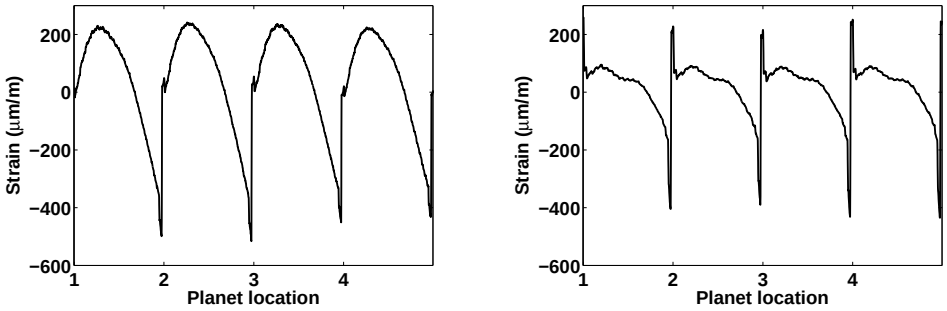

(a) (b)

Figure 5.25: (a) Strain from the gauge closest to the free end of the W2000 stage 2 ring, and (b) Strain from the gauge closest to the constrained end of the stage 2 ring.

The variation in strain characteristics across the stage 2 ring facewidth is consistent with the experiments and is slightly more drastic than the variations observed in stage 1. Again, strain from the constrained end of the ring exhibits more pronounced peaks when a planet tooth contacts a ring tooth. This sharp spike and rapid reversal in strain at the constrained end of the ring becomes less pronounced near the free end of the ring. A slight modulation can be observed near the constrained end of the stage 2 ring in both the experiments (Figure 5.26(b) as shown in Chapter 4) and the computational results (Figure 5.25(b)). This phenomenon can be attributed to model deflections and will be examined in the next section. When comparing the stage 2 computational strain (Figure 5.25) to the experimental strain (Figure 5.26), it is clear that the shapes and peak-to-eak strain values are similar.

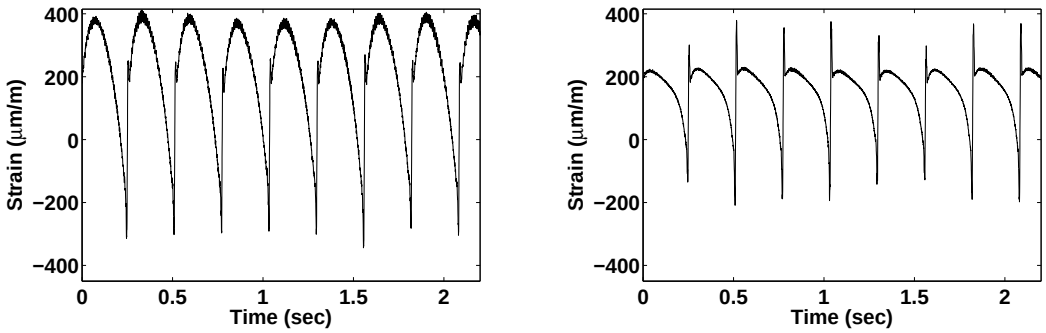

(a) (b)

Figure 5.26: Experimental strain from the stage 2 ring on the W2000 gear train from the gauge: (a) closest to the free end (gauge 8), and (b) closest to the constrained end (gauge 1).

5.3.2 Effects of Gravity and Model Deflections

Similar to the W3600, the inclusion of gravity in the W2000 finite element/contact mechanics model is important when correlating results to experiments and accurately capturing system deflections. The weight of the second gear train that is attached to the front of the main rotor shaft in the back-to-back power circulating test rig configuration causes the main rotor shaft to deflect in the direction of gravity. The front of the main rotor shaft deflects more in the downward direction than the end that is attached to the stage 2 carrier. This induces a tilting in the main rotor shaft and also causes the stage 2 ring and drive flange 2 to tilt. It is believed that the tilting of the stage 2 ring and drive flange contributes to the slight modulation in strain observed near the constrained end of the ring. Figures 5.27(a) and 5.27(b) depict the exaggerated deflection of the main rotor shaft and stage 2 carrier and the exaggerated deflection of the stage 2 ring-drive flange 2 subassembly, respectively. The horizontal line in both figures represents the fixed central axis of the gearbox. The overall tilting of the main rotor shaft can be observed in Figure 5.27(a), with the front deflecting in the downward direction.

The differing constraints at each end of the stage 2 ring cause nonuniform radial deflection when a planet tooth contacts a ring tooth, leading to the constrained end carrying more load. The maximum peak-to-peak strain at the constrained end of the ring occurs near planet location 1 and the minimum peak-to-peak strain occurs near planet location 3 (evident in Figure 5.25(b)). This is likely an artifact of the tilting of the stage 2 ring and drive flange. Near planet location 1, a meshing planet tooth contacts the constrained end of the ring first because the contact is downward on the top side of the ring tooth. On the contrary, near planet location 3 the contact force

is shifted more towards the free end of the ring because the planet tooth contact is upward on the bottom side of the ring tooth.

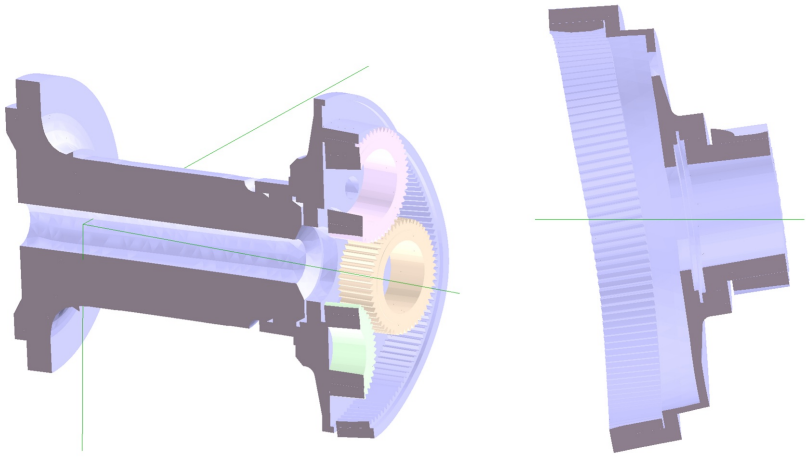

(a) (b)

Figure 5.27: W2000 components shown with exaggerated deformation: (a) main rotor shaft-stage 2 carrier subassembly, and (b) stage 2 ring-drive flange 2 subassembly.

Figures 5.28(a) and 5.28(b) show the stage 2 instantaneous ring tooth contact forces. The load distribution at planet location 1 is more concentrated near the constrained end of the ring than at planet location 3 (slightly steeper gradient in contact pressure moving from the free to constrained end of the ring tooth). This observation is consistent with the strain peaks from the finite element model shown in Figures 5.25(a) and 5.25(b). This behavior contributes to the slight strain modulation and will be investigated further.

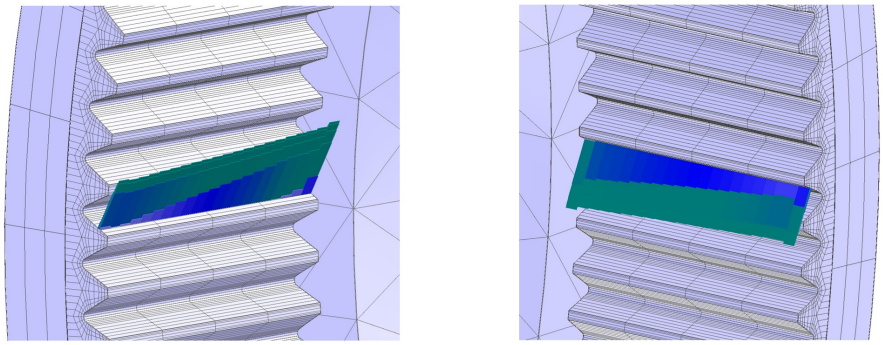

(a) (b)

Figure 5.28: W2000 instantaneous contact pressure forces on the stage 2 ring at (a) planet location 1 and (b) planet location 3.

In order to gain a better understanding of modulation observed near the constrained end of the stage 2 ring, a simulation was run over two ring revolutions with twenty steps in between each planet pass. Two ring revolutions were considered because the system kinematics dictate that there are roughly five and a half planet passes per ring revolution. Running a simulation for two ring revolutions ensures an integer of planet passes and that the starting and ending position of the instrumented ring tooth occur during a planet pass at the same location. Similar to the W3600 system, modulation can be observed using results from this simulation and spectra can be compared to the experiments.

Figures 5.29(a) and 5.29(b) show the root strain from the constrained end of the stage 2 ring over two ring revolutions and the corresponding planet pass locations, respectively. Strain was extracted from one ring tooth (similar to the instrumented tooth in the experiments) so the planet passes occur in real time. 20 time steps were used between each planet pass so peak-to-peak strain values cannot be compared

directly to experiments. The modulation in the signal can still be observed, with maximum peak-to-peak values occurring near plane planet location 1 and minimum peak-to-peak values occurring near planet location 3. This is consistent with strain shown in Figure 5.25(b).

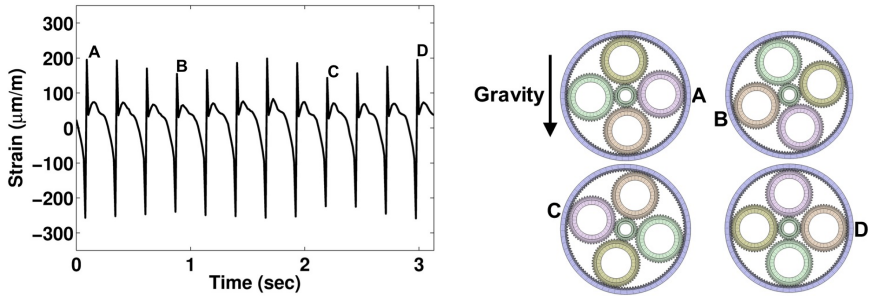

(a) (b)

Figure 5.29: (a) Finite element calculation of stage 2 ring gear root strain from the constrained end of the W2000 gear train over two ring revolutions and (b) corresponding planet pass locations.

Figure 4.15(b) (from Chapter 4) shows spectra of experimental strain from the constrained end of the stage 2 ring. Peaks at multiples of planet pass frequency and sidebands about the planet pass frequency at plus or minus the ring gear speed can be seen in these figures, respectively (sidebands are present at $n\omega_{pp} \pm \omega_r$ where n = 1, 2, 3...). Figure 5.30(a) shows similar sidebands in the spectra of computational strain data (available by taking a DFT of the data shown in Figure 5.29(a)). This confirms that the slight modulation observed near the constrained end of the stage 2 ring in both the experiments and the finite element model is related to the rotation of the ring gear. This infers that the finite element/contact mechanics model is capturing a modulation similar to what was observed in the test data.

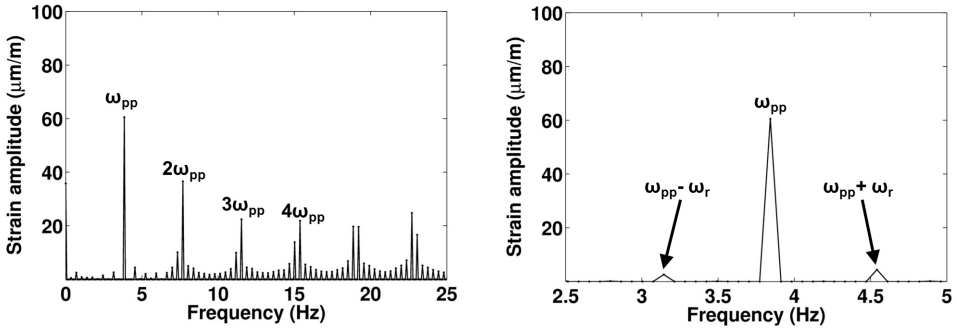

(a) (b)

Figure 5.30: Spectra of computational strain from the constrained end of the W2000 stage 2 ring showing (a) peaks at multiples of planet pass frequency (ω_{pp}) and (b) peak at planet pass frequency with sidebands at $\pm$ the ring gear speed (ω_r).

5.3.3 Carrier Eccentricity

A large modulation in strain (similar to what was observed near the constrained end of the W3600 stage 2 ring) was not apparent in the W2000 system. Nevertheless, the effects of eccentricity were investigated. Eccentricity was applied to the finite element model using unloaded bearing deformations at the two bearing connections between the main rotor shaft and the housing. Figure 5.31 shows the locations of these two connectors. Eccentricity can be simulated by applying an unloaded deformation to the inner race (connected to the main rotor shaft) of these connectors relative to the outer race (connected to the housing).

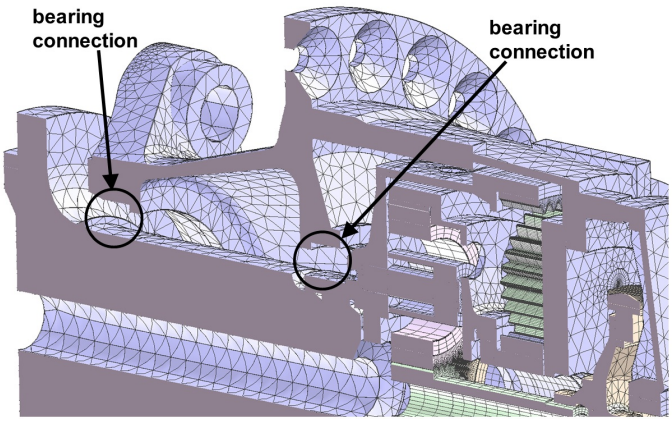

Figure 5.31: Two bearing connections given unloaded deformation to simulate eccentricity that connect the main rotor shaft and the stage 2 carrier to the housing in the W2000 model.

Figures 5.32(a), 5.32(b), and 5.32(c) show the tangential bearing reaction forces observed in stage 2 of the finite element model with no eccentricity, 400 μm eccentricity, and 1 mm eccentricity in the direction of gravity, respectively. In the system with no eccentricity, the largest bearing reaction force occurs at planet location 3. This is because of the slight upward deflection of the stage 2 carrier (induced by the overall tilting of the main rotor shaft shown in Figure 5.27(a)). When eccentricity in the downward direction is introduced, the largest bearing reaction force occurs at planet location 1. This is because the downward deflection of the main rotor shaft increases the mesh contact force at planet location 1 and decreases the mesh contact force at planet location 3.

Figures 5.33(a) and 5.33(b) show peak-to-peak strain at the constrained end of the stage 2 ring from the finite element model with 400 μm and 1 mm eccentricity in the direction of gravity, respectively. Strain changes only slightly with different values

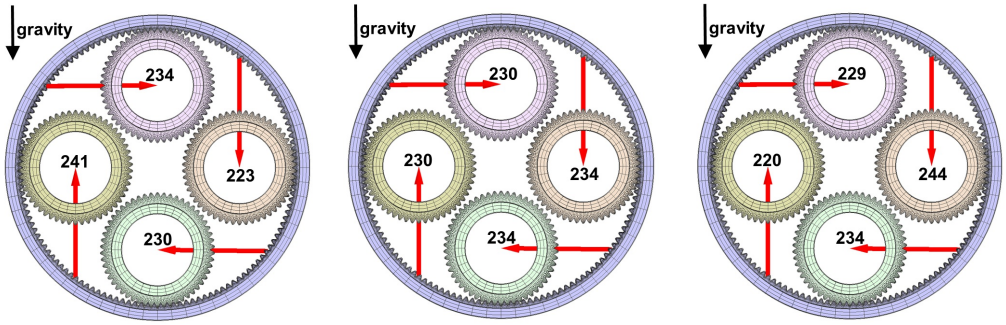

(a) (b) (c)

Figure 5.32: W2000 tangential bearing reaction forces (kN) of the stage 2 planets for the model with: (a) no eccentricity, (b) 400 μm eccentricity in the direction of gravity, and (c) 1 mm eccentricity in the direction of gravity.

of eccentricity. When compared to the W3600 system, eccentricity seems to have minimal effect on the bearing reaction forces and peak-to-peak strain. Eccentricity was also investigated in the upward direction but showed even less of an effect on the system. This is likely due to the main rotor shaft being free to move whereas in the W3600, the main rotor shaft was constrained. This added compliance in the main rotor shaft seems to make the W2000 less sensitive to this type of eccentricity.

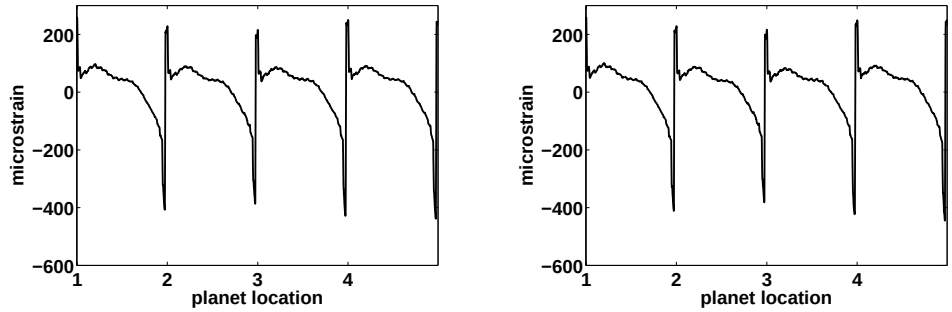

(a) (b)

Figure 5.33: Computational strain from the constrained end of the W2000 stage 2 ring with (a) 400 *mum* eccentricity in the direction of gravity and (b) 1 mm eccentricity in the direction of gravity.

5.4 FC5500 Computational Strain Results

5.4.1 Pin Tilting Error and Eccentricity

Unlike the other gear trains discussed hitherto, flexpin tilting errors were implemented into the finite element/contact mechanics model of the FC5500 gear train. Pin tilting was observed in the gear train when it was assembled. It is believed that the cause of this is the pressfit at the pin-carrier connection. Uneven expansion at this location causes the front of the pin to expand radially. This tilting contributes to the uneven tooth load distribution observed in the experiments and is captured by the finite element/contact mechanics model. Figure 5.34 shows how pin tilting error is implemented using Calyx.

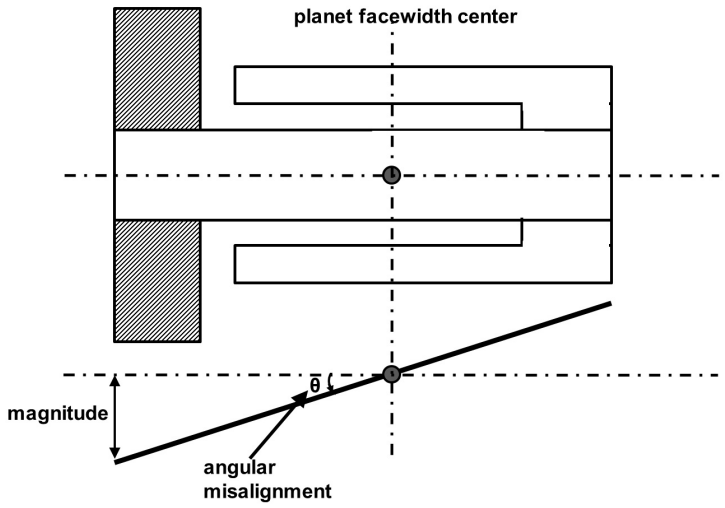

Figure 5.34: Implementation of pin tilting errors in the finite element/contact mechanics model of the FC5500 gear train.

An angular misalignment (in degrees) must be defined about the tangential axis of the planet (MISALNMT_TANG in Calyx). This rotation is applied about the center of the planet facewidth. Because this rotation moves each end of the pin a certain distance in opposite directions, a radial pin position error must also be applied to compensate for the angular misalignment. In Figure 5.34, the magnitude of the radial pin position error is shown. Translating the pin in the radial direction by this magnitude will simulate tilting of the pin. Pin position error (translation) applied at zero degrees about the z axis of the planets moves the pins radially. The Multyx menu used to implement pin position error is discussed in Appendix E.

The tilting of the stage 1 pins shifts the tooth load distribution towards the constrained end of the ring and the tilting of the stage 2 pins shifts the load towards the free end of the ring. This is because the stage 1 pins are cantilevered to the front of

the stage 1 carrier and extend towards the front of the gear train and the stage 2 pins are cantilevered to the stage 2 carrier and extent towards the rear of the gear train. This will be discussed later in this chapter. The stage 1 pins were given an angular misalignment (applied at the center of the planet facewidth) and then translated in the radial direction. The stage 2 pins were given an angular misalignment to induce tilting in the other direction and also translated in the radial direction.

Based on the results with the inclusion of eccentricity in the W3600 model and using known bearing clearance values for the FC5500 gear train, eccentricity was applied to the three bearing locations shown in Figure 5.35. Using unloaded deformation values near the maximum bearing clearance value for each connector yields reasonable results and compares well to experiments.

Unloaded deformation is applied to the front bearing that connects the housing to the main rotor shaft and to the rear bearing that connects the housing and the support plate. Unloaded deformation for both of these bearings is applied to the outer race (attached to the housing) in the direction of gravity. An unloaded deformation is also applied to the inner race of stage 3 wheel bearing (the connector furthest to the left in Figure 5.35) in the direction of gravity. In addition, a slight unloaded deformation was applied to this bearing in the horizontal direction away from the high-speed output shaft.

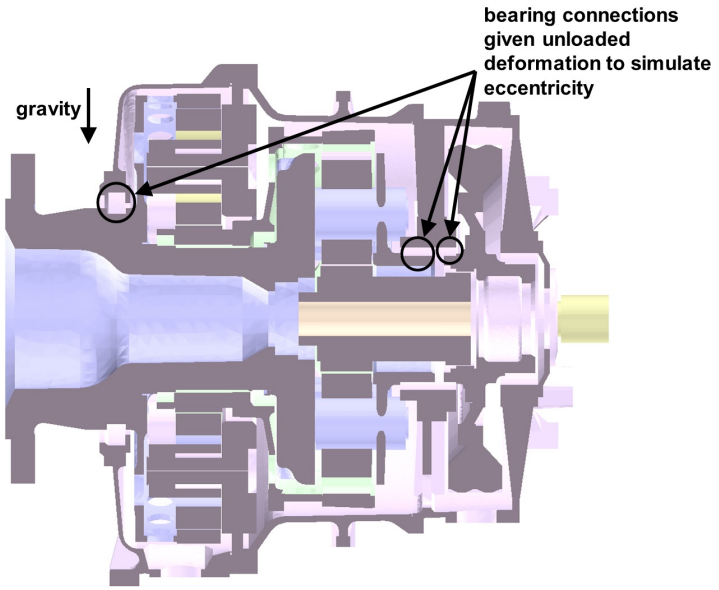

Figure 5.35: Location of bearings given an unloaded deformation to simulate eccentricity in the finite element/contact mechanics model of the FC5500 gear train.

Figure 5.36 shows the deformation of the FC5500 gear train (scaled by 300) with these specific unloaded bearing deformations and pin tilting errors. It can be seen that the housing is deflecting in the direction of gravity and the stage 3 wheel is deflecting in the direction of gravity relative to housing. This behavior also induces tilting in the stage 2 sun and shaft that connects to the stage 3 wheel via a stiffness matrix that replicates a spline connection. These model deflections contribute to the modulation observed in the stage 2 strain data and will be discussed in the next section.

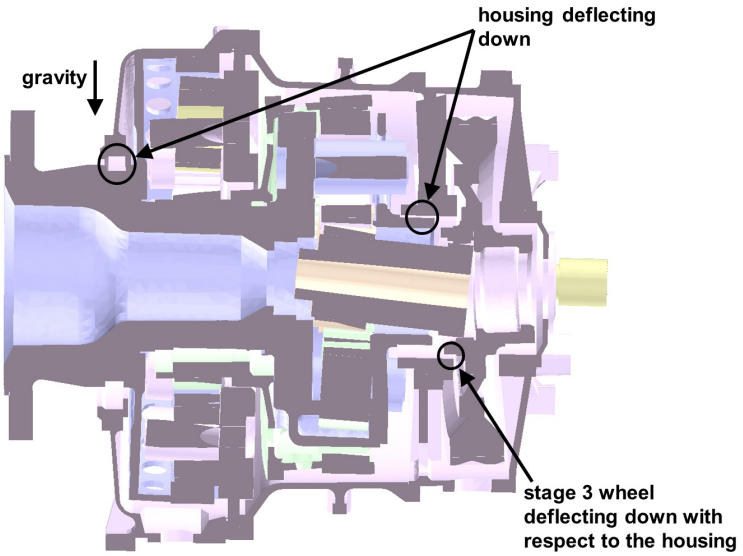

Figure 5.36: Model deflections (scaled by 300) with applied unloaded bearing deformations and pin tilting errors for the finite element/contact mechanics model of the FC5500 gear train.

5.4.2 Correlation to Experiments

Computational strain results are examined using the eccentricity and pin tilting error values given above and in general, peak-to-peak strain values for both stages are in agreement with the experiments. Figures 5.37(a) and 5.37(b) show computational strain from the free end (gauge 1) and constrained end (gauge 8) of the stage 2 ring, respectively. Similar to the experimental strain for the same gauge locations (Figures 4.20(a) and 4.20(b) given in Chapter 4) a modulation in strain is present in both signals. The most distinct occurs at the constrained end of the ring in both experimental and computational strain.

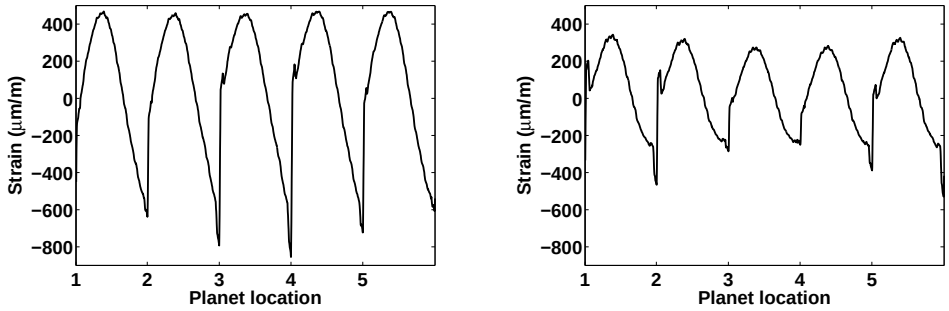

(a) (b)

Figure 5.37: (a) Finite element calculation of strain from the gauge closest to the free end of the FC5500 stage 2 ring (gauge 1) and (b) strain from the gauge closest to the constrained end of the stage 2 ring (gauge 8) with eccentricity and pin tilting error.

Another similarity between the experimental and computational strain is that the maximum peak-to-peak strain that occurs at a given planet location at the constrained end of the ring corresponds to the minimum peak-to-peak strain at the free end of the ring and vise versa. This indicates that the maximum peak-to-peak strain at the constrained end of the ring occurs when a ring tooth meshes with a planet tooth at planet location 1 (as shown in Figure 5.7(a)). Furthermore, the maximum peak-to-peak strain at the free end of the ring occurs when a ring tooth meshes with a planet tooth near planet location 4. The stage 2 shapes and peak-to-peak strain values from the finite element/contact mechanics model (Figure 5.37) are consistent with the experimental strain signals (Figure 5.38 as shown in Chapter 4), with the maximum strain peak at the constrained end of the ring corresponding to the minimum strain peak at the free end.

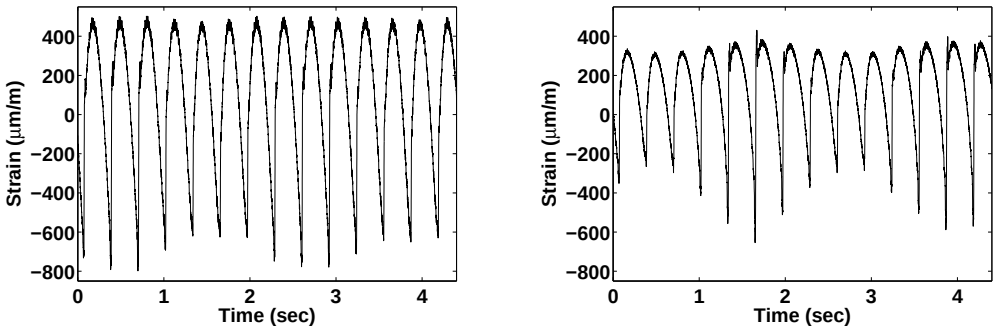

(a) (b)

Figure 5.38: Experimental strain from the stage 2 ring on the FC5500 gear train from the gauge: (a) closest to the free end (gauge 1), and (b) closest to the constrained end (gauge 8).

This type of root strain behavior was observed in the W3600 gear train and indicates that two different mesh inclinations are present on either side of the ring. This behavior is supported in Figures 5.39(a) and 5.39(b) that show the instantaneous contact pressure on the stage 2 ring at planet locations 1 and 4, respectively.

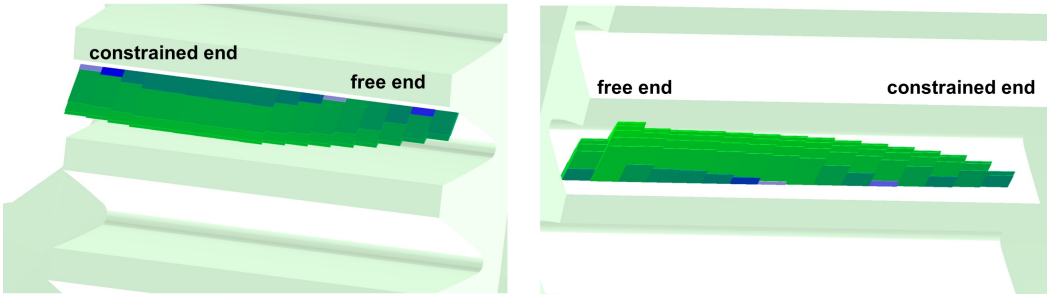

(a) (b)

Figure 5.39: Instantaneous contact pressure on the stage 2 ring with eccentricity and pin tilting errors at (a) planet location 1 and (b) planet location 4.

At planet location 1, the tooth load distribution is slightly shifted towards the constrained end of the ring. At planet location 4, the tooth load distribution is shifted towards the the free end of the ring. The eccentricity of the main rotor shaft in the upward direction relative to the housing increases the mesh force at planet location 1 because the contact is in the upward direction on the bottom of the ring tooth and decreases the mesh force near planet location 4 because the contact is in the downward direction on the top of the ring tooth. These extremes of mesh inclination are examined further in Chapter 6.

The added pin tilting error increases the load distribution towards the free end of the ring as seen in Figure 5.39(b). Furthermore, the modulation observed in the strain is related to the revolution of the instrumented ring tooth. As discussed for the other gear trains, the maximum and minimum peak-to-peak strain at the free or constrained end of the ring occur on opposite sides of the ring (near three and nine o'clock).

Figures 5.40(a) and 5.40(b) show computational strain from the free end (gauge 8) and constrained end (gauge 1) of the stage 1 ring, respectively. As seen in experimental strain from the same gauge locations (Figures 4.21(a) and 4.21(b), respectively), a more distinct peak in strain is visible during a planet pass near the constrained end of the ring. Also similar to the experiments, a slight modulation is present near the constrained end of the ring.

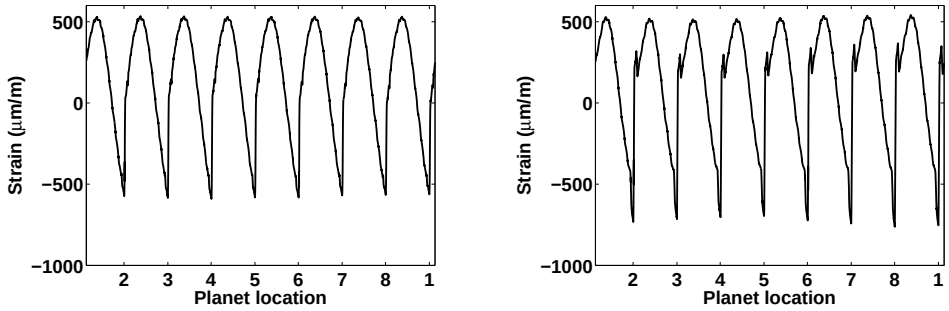

(a) (b)

Figure 5.40: (a) Finite element calculation of strain from the gauge closest to the free end of the FC5500 stage 1 ring (gauge 8) and (b) strain from the gauge closest to the constrained end of the stage 2 ring (gauge 1) with eccentricity and pin tilting error.

The tooth load distribution is shifted towards the constrained end of the stage 1 ring at all planet locations. Figure 5.41 shows the instantaneous contact pressure at planet location 1 (as shown in Figure 5.6(a)). The pin tilting error is responsible for the uneven load distribution on the stage 1 ring teeth.

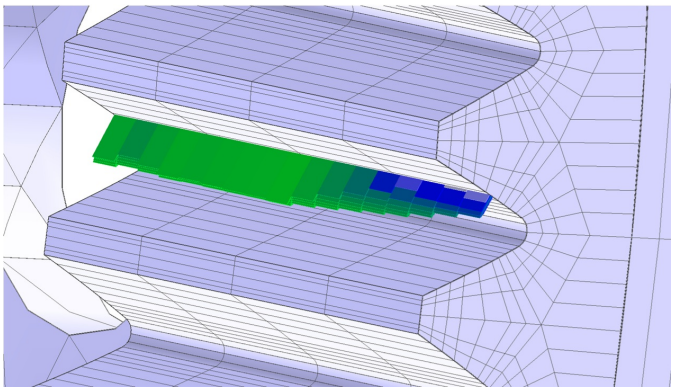

Figure 5.41: Instantaneous contact pressure on the stage 1 ring at planet location 1 with eccentricity and pin tilting errors.

Chapter 6: MEASURES OF SYSTEM PERFORMANCE

6.1 Tooth Load Distribution Factor ($K_{H\beta}$)

Gear misalignment is one of the key contributors to gear fatigue. Uneven load distribution along gear tooth facewidths is caused by mesh misalignment in the plane of action consisting of load-induced elastic deformation of gear bodies and gear train housings, bearing displacements, manufacturing errors, and thermal distortions [49]. Gear meshes generally have high stiffnesses so a relatively small misalignment can result in a significant increase of loading towards one side of a tooth. This can cause premature failures in gears due to uneven contact and wear patterns. The most direct approach to experimentally quantify tooth face distribution is to measure root strain at multiple locations across the gear facewidth, as done in the experimental analyses for the gear trains discussed in Chapter 4. A term used to quantify tooth load distribution across gear tooth facewidths is $K_{H\beta}$. This term is calculated in accordance with ISO Standard 6336-1 Method A [49]. By this method, the load distribution over the facewidth is determined by assessing measured values of tooth root strain.

$K_{H\beta}$ is defined as the maximum load intensity (local load per unit length increment of facewidth) compared to the mean load and is given as [49]

$$K_{H\beta} = \frac{maximum\,load\,per\,unit\,facewidth}{average\,load\,per\,unit\,facewidth} = \frac{(\frac{F}{b})_{max}}{\frac{F_m}{b}}, \tag{6.1}$$

where tangential loads at the reference cylinder are used for an approximate calculation using the transverse specific loading following [49]

$$\frac{F_m}{b} = \frac{F_t K_A K_v}{b}. \tag{6.2}$$

F_m in the mean transverse tangential load at the reference circle and depends on the nominal transverse tangential load at the reference circle (F_t), the application factor (K_A), and the dynamic factor (K_v). In practice, the tooth contact and bending stresses depend on these factors. The term, b refers to the gear tooth facewidth.

$K_{H\beta}$ is calculated using experimental strain by taking the largest relative root stress intensity at any of the strain gauges across the ring facewidth (when a planet tooth meshes with the instrumented ring tooth) and dividing it by the average relative root stress intensity for all eight strain gauges across the facewidth. The relative root stress intensity simply refers to peak-to-peak strain gauge voltage during the rapid reversal in strain when a planet tooth meshes with a ring tooth. A perfectly even load distribution would yield a $K_{H\beta}$ value of 1.0. Plotting the relative root stress intensity across the facewidth of a ring gear is an effective way to visually show the tooth load distribution. Each planet location relative to the instrumented ring tooth yields a different $K_{H\beta}$ value. A range of values can be observed for different planet pass locations. It is not known what experimental planet location corresponds to the extremes of $K_{H\beta}$ but these locations can be predicted using computational results.

$K_{H\beta}$ can also be examined using computational peak-to-peak strain across the ring gear facewidths. $K_{H\beta}$ is calculated using finite element/contact mechanics model results by taking the maximum peak-to-peak strain at a given strain gauge location when a planet tooth meshes with a ring tooth and dividing it by the average peak-to-peak strain for all eight gauges. In this chapter, comparisons will be made between experimental and computational $K_{H\beta}$ values for each gear train. The effects of eccentricity on $K_{H\beta}$ will also be discussed.

6.1.1 W3600 Tooth Load Distribution

Load distribution details and experimental relative root stress intensity plots showing $K_{H\beta}$ values for the W3600 system are given and discussed in [42]. The variation in strain across the stage 2 ring facewidth yields a range of $K_{H\beta}$ values and varying inclination of tooth load distribution. As discussed in [42], this type of behavior indicates that the mesh undergoes a rocking alignment transition with minimal displacement near the middle of the tooth and maximum displacement near each end. Figure 6.1 shows the load distribution across the stage 2 ring facewidth at both observed extremes of mesh inclination using experimental data. These extremes are labeled maximum tip to rotor and maximum tip to generator to indicate maximum mesh inclination towards the rear and front of the gear train, respectively. The largest $K_{H\beta}$ values occur when the mesh is inclined towards the generator. $K_{H\beta}$ values at this inclination range from 1.50 to 1.79 which is unfavorable. Experimental $K_{H\beta}$ values for maximum tip to rotor mesh inclination ranged from 1.07 to 1.13.

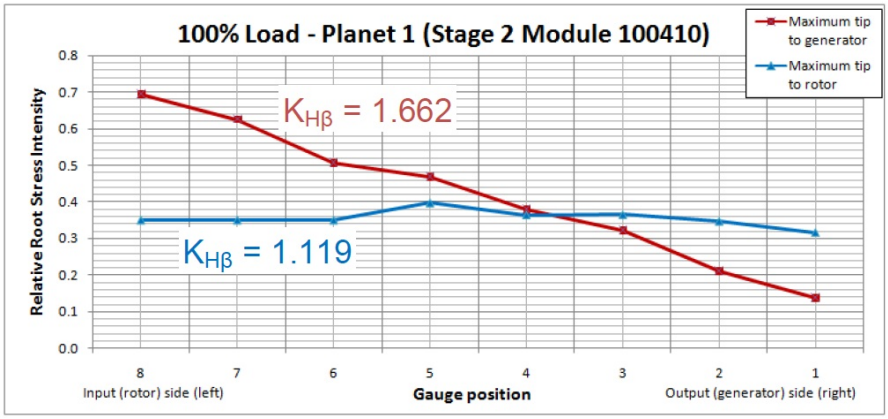

Figure 6.1: W3600 experimental relative root stress intensity across the stage 2 ring facewidth at extremes of mesh inclination [42].

Figure 6.2 shows the finite element calculation of load distribution across the stage 2 facewidth using peak-to-peak computational strain at planet locations 1 and 3 from the finite element model with no eccentricity. The corresponding $K_{H\beta}$ values are shown. It can be seen that the model with no eccentricity does not exhibit two drastically different extremes of mesh inclination as the experiments show. When investigating eccentricity in the system using unloaded bearing deformation as discussed in Chapter 5, the tooth load distributions and $K_{H\beta}$ values begin to resemble the experiments and the extremes of mesh inclination become apparent.

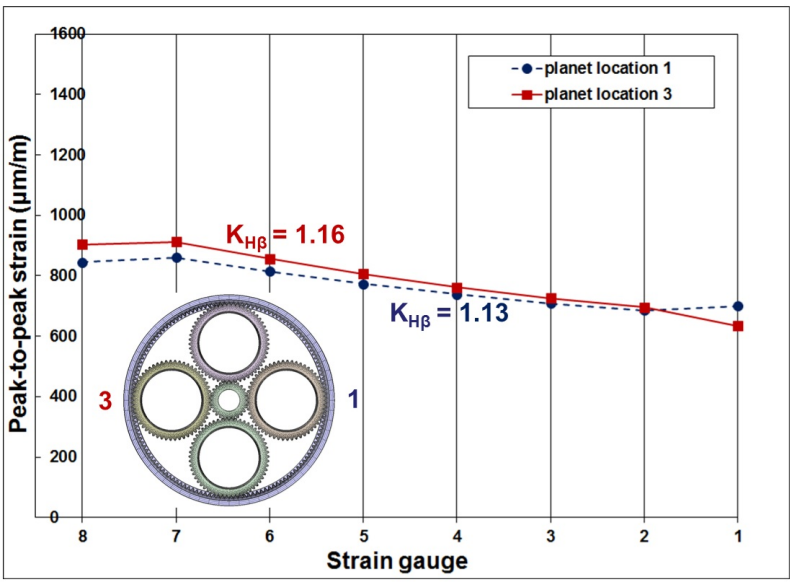

Figure 6.2: W3600 load distribution across the stage 2 ring facewidth determined from computational peak-to-peak strain at planet locations 1 and 3.

Figures 6.3(a) and 6.3(b) show the load distribution across the ring facewidth using peak-to-peak computational strain from the finite element model with 200 μm and 500 μm eccentricity in the direction opposite gravity, respectively. Increasing eccentricity increases mesh inclination with one extreme occurring at planet location 3 and the opposite inclination occurring at planet location 1. This behavior with two different mesh inclinations is consistent with experiments. The the maximum peak-to-peak strain at the constrained end of the ring occurs at planet location 3 and the maximum peak-to-peak strain at the free end of the ring occurs at planet location 1. This infers that extremes in mesh inclination very likely occur 180 degrees apart on either side of the ring near planet locations 1 and 3.

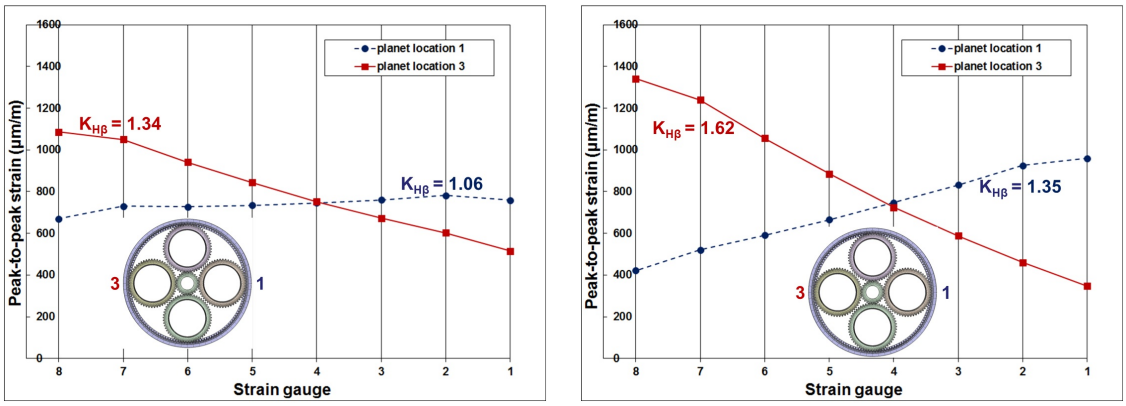

Figure 6.3: W3600 load distribution across the stage 2 ring facewidth determined from computational peak-to-peak strain at planet locations 1 and 3 for the model with: (a) 200 μm eccentricity, and (b) 500 μm eccentricity.

Figure 6.4(a) shows the relative load stress intensity across the stage 1 facewidth for different load cases using experimental data and the corresponding $K_{H\beta}$ value at nominal loading. Figure 6.4(b) shows load distribution across the stage 1 facewidth at planet locations 1 and 5, determined from computational strain data. In general, the load distributions and $K_{H\beta}$ values for stage 1 match experiments well. The rocking mesh alignment transition was not observed in stage 1. Experimental $K_{H\beta}$ values ranged from 1.07 to 1.14.

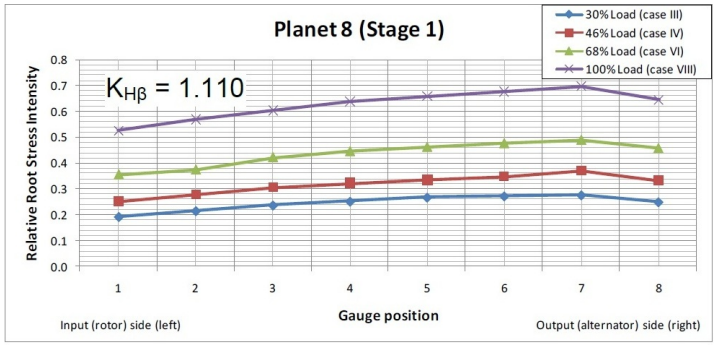

(a)

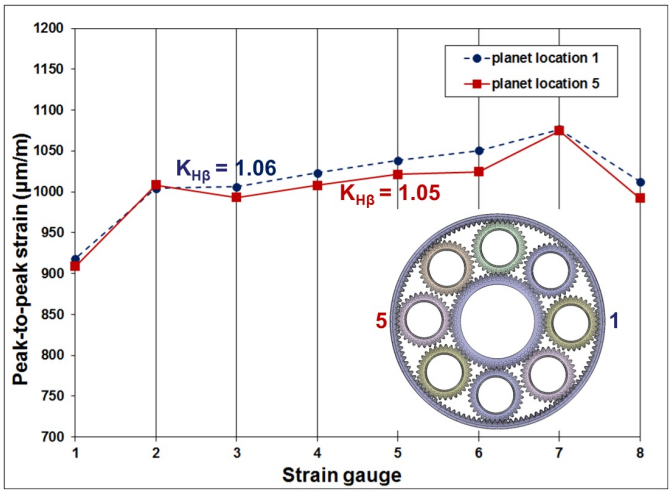

(b)

Figure 6.4: Load distribution across the W3600 stage 1 facewidth with $K_{H\beta}$ shown using: (a) experimental data [42], and (b) computational data at planet locations shown.

6.1.2 W2000 Tooth Load Distribution

Load distribution across the W2000 ring facewidths are compared to experiments in a similar manner as discussed for the W3600 system. Experimental load distributions and $K_{H\beta}$ values for the W2000 are discussed thoroughly in [47]. Figures 6.5(a) and 6.5(b) show the load distribution across the stage 2 ring facewidth using experimental data and computational peak-to-peak strain, respectively. Two slightly

different mesh inclinations can be observed in the experimental data, inferring that the planet-ring mesh undergoes a rocking alignment transition. This same phenomenon was observed in the W3600, but the W2000 exhibits more subtle changes in inclination. In Figure 6.5(a), the two different inclinations are labeled "rotor tip" and "gen tip", referring to mesh inclination towards the rotor and generator, respectively. Experimental $K_{H\beta}$ values range from 1.06 to 1.10 when the mesh is inclined towards the rotor and range from 1.16 to 1.20 when the mesh is inclined towards the generator.

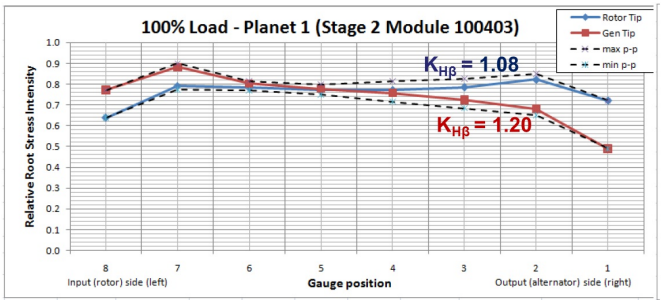

(a)

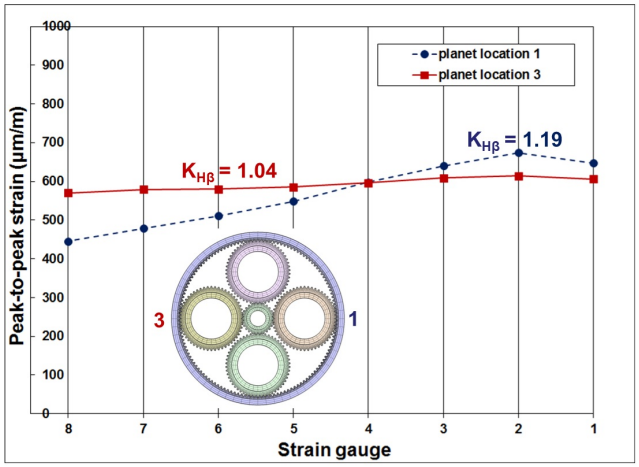

(b)

Figure 6.5: Load distribution across the W2000 stage 2 facewidth with $K_{H\beta}$ shown using: (a) experimental data [47], and (b) computational data at planet locations shown.

Figures 6.6(a) and 6.6(b) show the load distribution across the stage 1 ring facewidth using experimental data and computational peak-to-peak strain at each gauge location, respectively. Stage 1 does not exhibit different mesh inclinations so load distribution at a range of torques is shown in Figure 6.6(a). Experimental strain was unavailable at gauges 2 and 3 so the relative root stress intensity at these location was interpolated. This makes it more difficult to compare computational results to experiments. No explanation was available to explain the jump in experimental root strain between gauges 4 and 5 but possible error during data acquisition should be considered. Experimental $K_{H\beta}$ values at nominal loading ranged from 1.22 to 1.29.

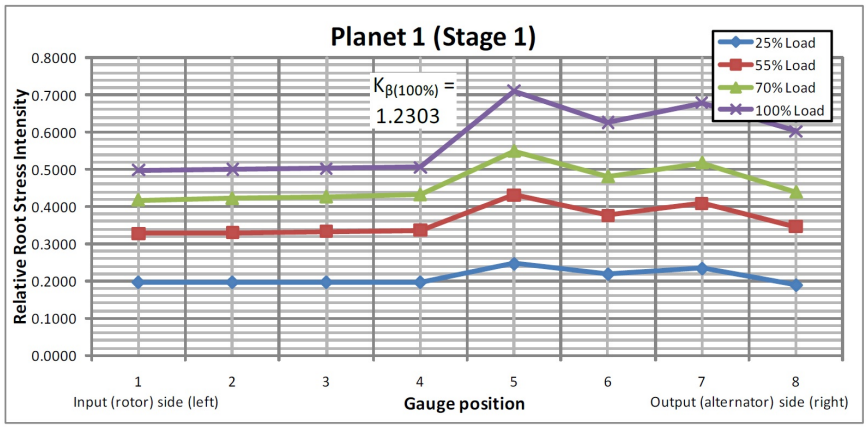

(a)

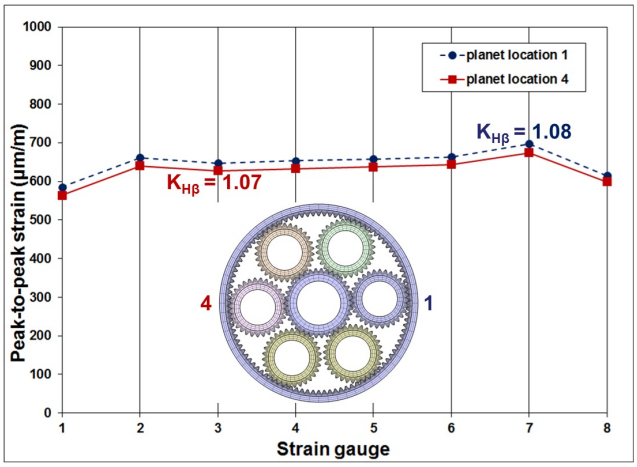

(b)

Figure 6.6: Load distribution across the W2000 stage 1 facewidth with $K_{H\beta}$ shown using: (a) experimental data [47], and (b) computational data at planet locations shown.

6.1.3 FC5500 Tooth Load Distribution

As discussed in Chapter 5, the stage 2 load distributions across the ring facewidth exhibit two different mesh inclinations that occur on either side of the ring (near three and nine o'clock). Figures 6.7(a) and 6.7(b) show the load distribution across the stage 2 ring facewidth using experimental data and computational peak-to-peak

strain. These plots are consistent with the instantaneous contact pressure shown in Figures 5.39(a) and 5.39(b) in Chapter 5. The two extremes of mesh inclination occur near planet locations 1 and 4. The stage 2 planet teeth have 20 μm of crowning and 50 μm edge relief on the side of the planet that meshes with the constrained end of the ring.

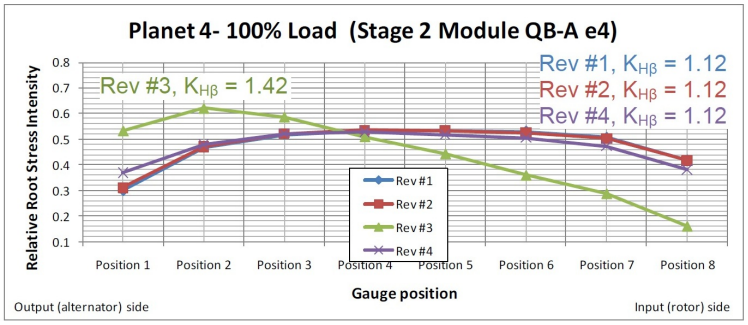

(a)

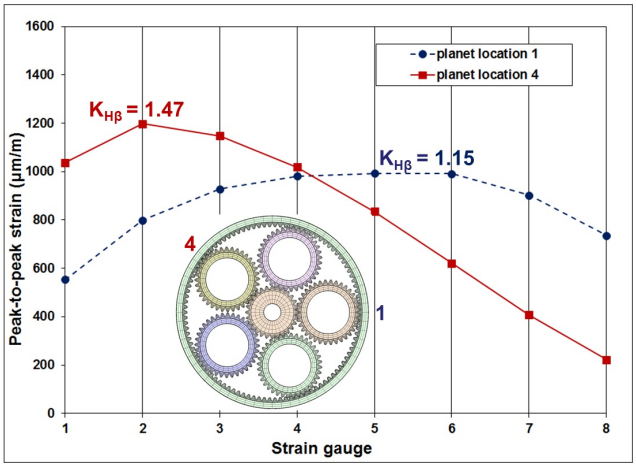

(b)

Figure 6.7: Load distribution across the FC5500 stage 2 facewidth with $K_{H\beta}$ shown using: (a) experimental data [48], and (b) computational data at planet locations shown.

The $K_{H\beta}$ values calculated from experimental data range from 1.12 to 1.42. $K_{H\beta}$ from the mesh inclination that is tilted towards the constrained end of the ring ranged from 1.12 to 1.21 and ranged from 1.18 to 1.42 at the other extreme of mesh inclination. Computational $K_{H\beta}$ was determined to be 1.15 and 1.47 at both extremes of mesh inclination (with 1.47 occurring with the load shifted towards the free end). These values are from the model with the eccentricity and pin tilting errors discussed in Chapter 5. Both eccentricity and pin tilting error contribute to the extremes in mesh inclination.

Figures 6.8(a) and 6.8(b) show the load distribution across the stage 1 ring facewidth using experimental data and computational peak-to-peak strain at each gauge location, respectively. As shown in Figure 5.41, the calculated load distribution from the finite element/contact mechanics model is shifted towards the constrained end of the ring. Gauge locations 1, 3, and 8 are interpolated in Figure 6.8(a) because experimental data was unavailable at these locations. Furthermore the finite element calculation of load distribution seems to overestimate the load near the center of the tooth facewidth with a slightly more rounded shape. The stage 1 planet teeth have 20 μm of crowning and 90 μm edge relief. $K_{H\beta}$ values calculated using experimental data ranged from 1.10 to 1.23. The finite element calculation of $K_{H\beta}$ yields results in this range of 1.17 and 1.18.

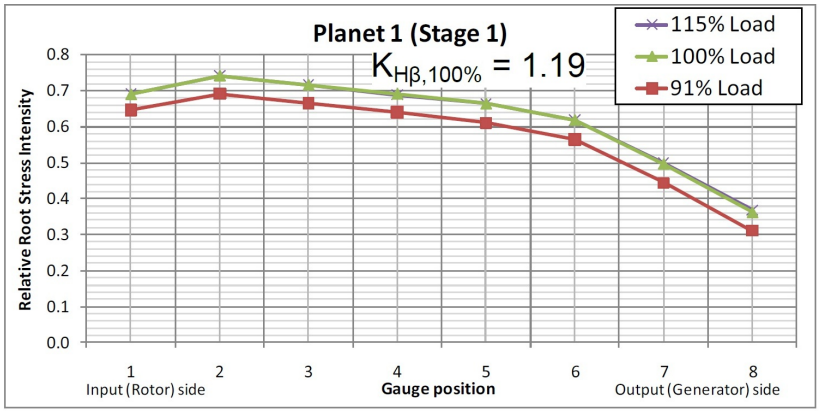

(a)

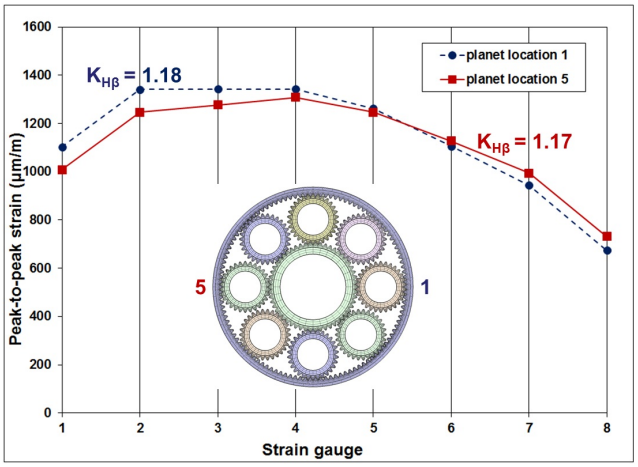

(b)

Figure 6.8: Load distribution across the FC5500 stage 1 facewidth with $K_{H\beta}$ shown using: (a) experimental data [48], and (b) computational data at planet locations shown.

6.2 Planet Load Sharing Factor (K_γ)

In general planet load sharing in the Orbital2 gear trains discussed herein is very good. In order to quantify planet load sharing in the experiments, a planet load sharing factor, K_γ, is derived from average peak-to-peak strain at given planet locations. K_γ is calculated using experimental strain data over a period of planet passes. For a certain planet configuration, peak-to-peak strain is averaged when a planet tooth meshes with a ring tooth at all eight strain gauge locations across the ring facewidth at each planet location. This value is then averaged over all planet locations during that period. K_γ is then determined by taking the planet location with the highest deviation from the average and dividing it by the average for all planet locations.

In cases where strong modulation is present, such as the constrained end of the stage 2 ring on the W3600 system, K_γ is calculated at both extremes of mesh inclination. Thus, load sharing factor is calculated using peak-to-peak strain when each planet-ring mesh is tilted towards the front and rear of the gearbox (likely near the same location relative to a fixed reference frame at either three or nine o'clock). This infers that strain peaks corresponding to each planet are observed over several cycles. This approach is not practical when determining K_γ using computational strain peaks because it would require running a simulation over many cycles. For example, K_γ is determined using computational peak-to-peak strain at the planet locations shown in Figures 5.2(a), 5.5(a), and 5.7(a) for stage 2 of the W3600, W2000, and FC5500 gear trains, respectively. Experimental planet load sharing for stage 2 of the FC5500 gear train was calculated using consecutive planet passes.

Unlike planet load sharing determined at extremes of mesh inclination (for stage 2 of the W3600 and W2000 gear trains), the computational strain peaks include

minimum and maximum peak-to-peak strain values (both inclinations of mesh alignment). Based on the computational results discussed hitherto, this implies that two of the planet locations correspond to the instrumented ring tooth meshing with planets 180 degrees apart at the three and nine o'clock positions. Even though a different planet arrangement relative to the instrumented ring tooth and gravity could yield different K_γ values, the inclusion of the largest and smallest strain peaks when large modulation is present ensures that the worst case scenario is evaluated.

When large modulation is not present, such as in stage 1 of each gear train, the load distribution across the ring facewidth does not exhibit extremes of mesh inclination. Therefore, K_γ is calculated using peak-to-peak strain for consecutive planet passes (not occurring at the same location relative to a fixed reference frame). This is analogous to the calculation using computational results. Load sharing factor for the epicyclic stages in each gear train will be discussed in the following sections.

6.2.1 W3600 Planet Load Sharing

The experimental planet load sharing factor for stage 2 in the W3600 system did not exceed 1.04. This K_γ value occurred at both extremes of mesh inclination. The computational peak-to-peak strain values used to determine K_γ correspond to the planet locations shown in Figure 5.2(a). Table 6.1 shows stage 2 planet load sharing factor determined using finite element results for the model without gravity and with gravity (containing no eccentricity and 200 and 500 μm eccentricity). Eccentricity in this case was applied in the direction opposite gravity using unloaded bearing deformation as discussed in Chapter 5. As expected, the model with no gravity exhibits perfect planet load sharing. Eccentricity increases K_γ. This is also expected

because the misalignment of the main rotor shaft and stage 2 carrier in the direction opposite gravity increases the planet mesh force at planet location 3 and reduces it at planet location 1.

Table 6.1: W3600 stage 2 planet load sharing factors

Model	Planet load sharing factor (K_γ)
Model without gravity	1.00
Model with gravity	1.01
Model with gravity and 200 μm eccentricity	1.04
Model with gravity and 500 μm eccentricity	1.07

Planet load sharing for stage 1 was determined to be 1.04. The value calculated using computational peak-to-peak strain at the planet locations shown in Figure 5.3(a) is 1.03. Overall for both planetary stages, planet load sharing factor was good.

6.2.2 W2000 Planet Load Sharing

Experimental planet load sharing factor (K_γ) for stage 1 in the W2000 system was determined to be 1.02. This is in good agreement with the finite element model which also yielded a load sharing factor of 1.02. Experimental planet load sharing factor for stage 2 was determined to be 1.01 and 1.02 for planet-ring mesh inclinations towards the generator and rotor, respectively. Table 6.2 shows stage 2 planet load sharing factors determined using computational strain for several different cases. Eccentricity in the direction of gravity increases K_γ only slightly. In general, planet load sharing factor was very good for both epicyclic stages. This is supported both experimentally and computationally.

Table 6.2: W2000 stage 2 planet load sharing factors

Model	Planet load sharing factor (K_γ)
Model without gravity	1.00
Model with gravity	1.01
Model with gravity and 400 μm eccentricity	1.02
Model with gravity and 1 mm eccentricity	1.03

6.2.3 FC5500 Planet Load Sharing

Planet load sharing factor (K_γ) calculated using experimental data for stage 1 on the FC5500 gear train was determined to be 1.06 [48]. Using peak-to-peak strain from the finite element/contact mechanics model with the eccentricity and pin tilting errors discussed in Chapter 5 yielded a value of 1.02. This calculation uses strain from the planet locations shown in Figure 5.6(a). There is error that must be considered in the experimental calculation because strain at gauges 1, 3, and 8 was unavailable.

For stage 2, the (K_γ) values calculated using experimental data ranged from 1.05 to 1.08 over several revolutions. The (K_γ) values calculated using peak-to-peak strain from each planet location in the finite element/contact mechanics model is 1.04 (using eccentricity and pin tilting error values given in Chapter 5). This calculation was performed using strain at the planet locations shown in Figure 5.7(a). In general, planet load sharing in both stages is good.

Chapter 7: USE OF FINITE ELEMENT/CONTACT MECHANICS MODELS TO EXAMINE SYSTEM DESIGN CHANGES

The advantage of using Calyx as a design tool is that different designs can be examined without requiring the physical manufacture and experimentation of the newly designed system. Investigating different designs this way is faster and cheaper than carrying out experiments and acquiring test data. Such different designs could range from changes in tooth micro-geometry such as tip and lead modifications to changes involving more complex system components such as carriers or drive flanges. The influence of additional bearings to certain locations can also be studied. In this chapter, a few such design change examples will be discussed.

7.1 W3600: Effects of a More Flexible Stage 2 Annulus

With the computational model validated against experiments, the design of certain components can be changed to understand how the change affects the mechanics. One design change that is examined applies to the stage 2 annulus. The uneven loading of the stage 2 ring during a planet pass results from the local deformation of the stage 2 ring. A proposed design adds holes around the annulus with the thought being that a more compliant annulus would yield better load distribution across the ring

facewidth. This added compliance would cause the ring to deflect more evenly in the radial direction during a planet pass. A smooth distribution of material is also added to the rim of the ring gear such that the radial thickness at the free end is greater than at the constrained end. Figure 7.1(a) shows the finite element model of the stage 2 ring and annulus as tested, while Figure 7.1(b) shows the new design.

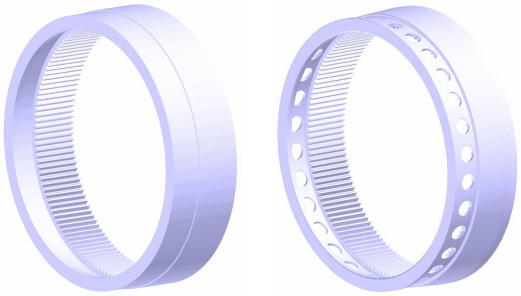

(a) (b)

Figure 7.1: (a) Finite element model of the stage 2 ring and annulus as tested, and (b) finite element model of a proposed design of a more flexible stage 2 annulus with holes.

When results from this proposed design for the stage 2 annulus are compared to the original model, a noticeable improvement in strain characteristics across the stage 2 ring gear occurs. Specifically, the sharp spike in strain that was observed near the constrained end of the ring during a planet pass for the original design is not present. Figures 7.2(a) and 7.2(b) show computational strain from the finite element model with the more flexible annulus at the free and constrained end of the stage 2 ring, respectively. The reason that the sharp spike in strain during a planet pass is not present in the model with the more flexible annulus is due to the local deflection of

the stage 2 ring. The more compliant annulus deflects more uniformly in the radial direction.

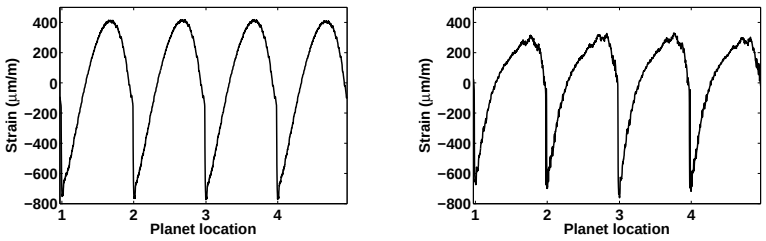

(a) (b)

Figure 7.2: Computational strain from the model with the more flexible stage 2 annulus from: (a) the gauge closest to the free end of the stage 2 ring, and (b) the gauge closest to the constrained end of the stage 2 ring.

Figure 7.3 further illustrates this by comparing ring rim deflections for both designs. Clearly, the more flexible annulus yields a more uniform ring deflection in the radial direction whereas the ring for the original design deflects more in the radial direction at the free end than at the constrained end. This deflection causes the constrained end of the ring to be loaded more for the original design, thus causing the sharp strain peak during a planet pass. The stage 2 annulus with holes around the circumference effectively improves load distribution across the facewidth of the stage 2 ring.

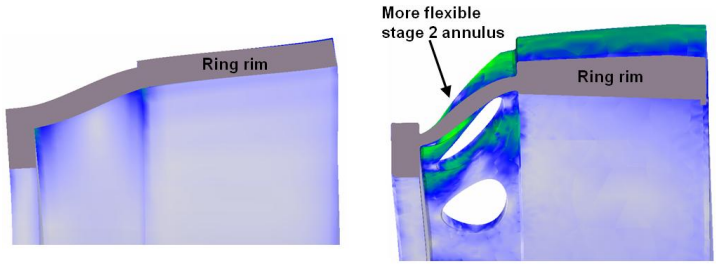

(a) (b)

Figure 7.3: (a) Deformation of the original stage 2 ring rim and annulus, and (b) deformation of the proposed design of the stage 2 ring rim with more flexible annulus.

7.2 W3600: Effects of Added Bearings

Another proposed design change examined for the W3600 gearbox is the addition of bearings to the stage 1 sun-drive flange 2 subassembly. Figure 7.4 shows the location of two bearings between the main rotor shaft and the stage 1 sun-drive flange 2 subassembly. These bearings are modeled using stiffness matrices and are discussed further in Appendix A. Simulations with these bearings added to the finite element model will be examined with and without eccentricity.

Figure 7.5(a) shows the load distribution across the stage 2 ring facewidth at planet locations 1 and 3 with corresponding $K_{H\beta}$ values for the model with the added bearings and the more flexible stage 2 annulus. These $K_{H\beta}$ values show an improvement over the ones given in Figure 6.2 which shows the stage 2 tooth load distribution for the original design. The improved load distribution can be attributed mainly to the more flexible annulus. Figure 7.5(b) shows the load distribution across the facewidth of the stage 2 ring for the model the added bearings and the more flexible annulus with 500 μm eccentricity in the direction opposite gravity. The noticeable difference between the load distribution and $K_{H\beta}$ values in this case and

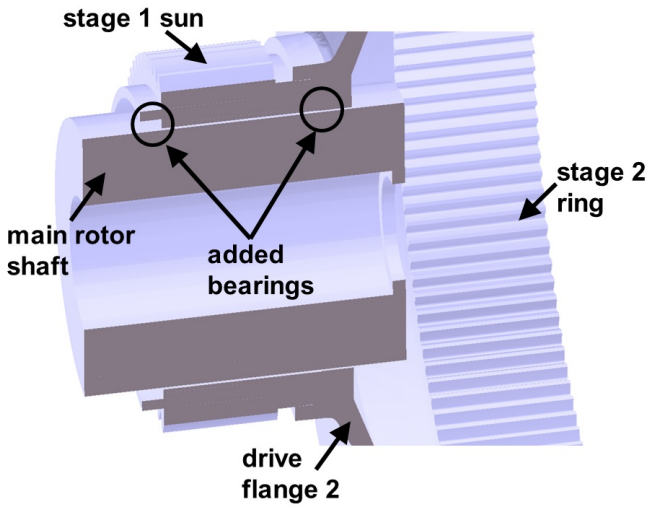

Figure 7.4: Added bearing locations to the stage 1 sun-drive flange 2 subassembly modeled with stiffness matrices.

the the results for the original design with the same amount of eccentricity (see Figure 6.3(b)) is that the modified design does not exhibit the extremes of mesh inclination at planet locations 1 and 3 as seen in the original design.

The lack of drastically different mesh inclinations is due to the added bearings supporting the stage 1 sun-drive flange 2 subassembly. The added stiffness at the bearing locations between the stage 1 sun and the main rotor shaft shown in Figure 7.4 supports the stage 1 sun-drive flange 2 subassembly and not only reduces its deflection in the downward direction due to gravity but also reduces strain modulation due to eccentricity. As the main rotor shaft becomes eccentric relative to the rest of the gear train, the stage 2 annulus and ring essentially move with it due to the added bearings. Tangential bearing reaction forces for this design support this further.

Figures 7.6(a) and 7.6(b) show the tangential bearing reaction forces for the modified design with no eccentricity and 500 μm eccentricity in the direction opposite

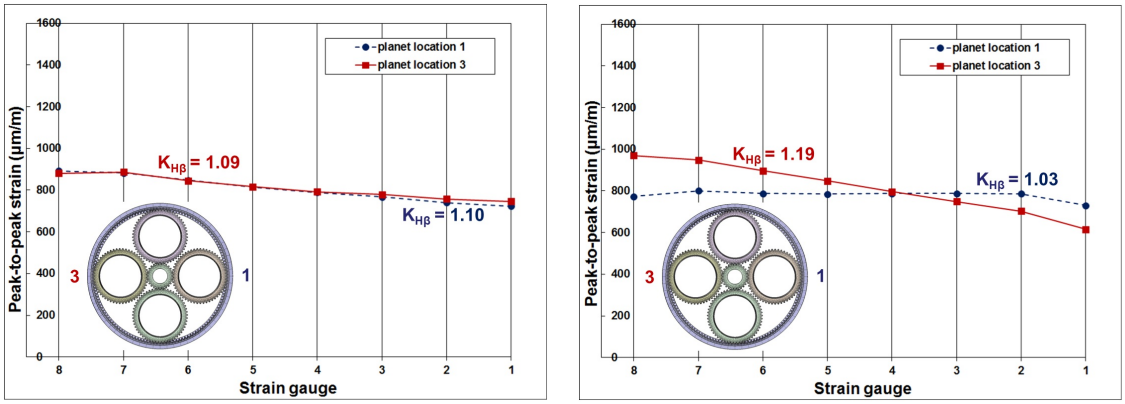

(a) (b)

Figure 7.5: Load distribution across the W3600 stage 2 facewidth with $K_{H\beta}$ shown for the design with added bearings and more flexible annulus with: (a) no eccentricity, and (b) 500 microns eccentricity in the direction opposite gravity.

gravity, respectively. When these figures are compared to the original design (Figures 5.14(b) and 5.20(b), respectively) it is evident that the modified design reduces the difference in bearing reaction forces at planet locations 1 and 3, thus reducing modulation and improving planet load sharing. Planet load sharing factor (K_γ) values for the models given in Figures 7.6(a) and 7.6(b) are 1.01 and 1.02, respectively.

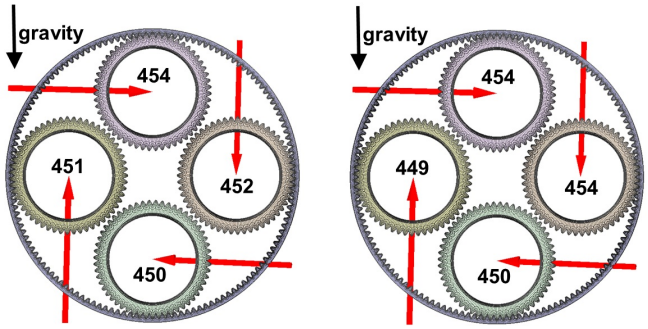

(a) (b)

Figure 7.6: W3600 tangential bearing reaction forces (kN) of the stage 2 planets for the modified design with added bearings and more flexible stage 2 annulus for: (a) the model with no eccentricity, and (b) the model with 500 μm eccentricity in the direction opposite gravity.

When examining this design, bearing clearances must be carefully considered. If the clearance of the bearing at the front of the gear train that connects the main rotor shaft to the housing is more than the clearance of the bearings between the stage 1 sun and the main rotor shaft, then the front bearing could potentially be unloaded during operation. This would be undesirable and could lead to premature failures.

7.3 W3600: Effects of Planet Lead Modifications

The effect of adding lead crowning and edge relief to the planet teeth of both epicyclic stages is investigated using Calyx. The lead modifications consist of 22 μm crowning and 80 μm edge relief on the stage 1 planets and 20 μm crowning and 50 μm edge relief on the stage 2 planets. The modifications are implemented in the finite element/contact mechanics model using the micro geometry capabilities of Calyx described in Chapter 2.

The removal of material near the edges of the planet teeth yields a ring tooth load distribution that is more concentrated towards the center of the tooth. Figures 7.7(a) and 7.7(b) demonstrate this by showing the stage 2 ring contact pattern over a mesh cycle for the model containing planets with no lead modifications and the model containing planets with 20 μm crowning and 50 μm of edge relief and the more flexible annulus, respectively. The design with no lead modifications shows a ring tooth load distribution more concentrated near the constrained end of the ring. Planet lead crowning and the more flexible annulus shift the load towards the tooth center.

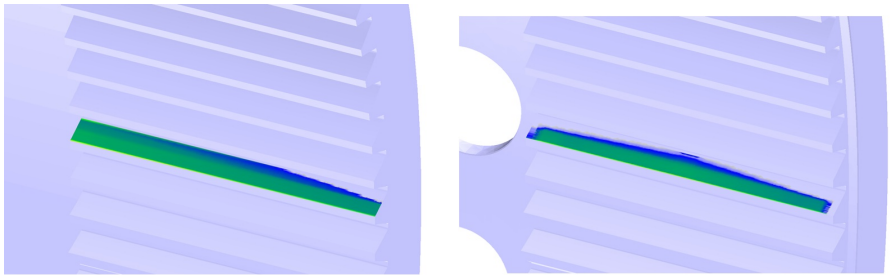

(a) (b)

Figure 7.7: Stage 2 ring contact pattern over a mesh cycle on the W3600 with: (a) no lead modifications, and (b) 20 μm lead crowning and 50 μm edge relief.

Another way to quantify the effects of planet lead modifications is to examine the load distribution across the ring tooth facewidths using peak-to-peak strain at each strain gauge location to calculate corresponding $K_{H\beta}$ values. Figures 7.8(a) and 7.8(b) show the load distribution and corresponding $K_{H\beta}$ values for stages 1 and 2, respectively. As expected, the higher peak-to-peak strain occurs near the tooth centers. The parabolic shape of the load distributions yields slightly higher $K_{H\beta}$

values than for the design with no lead modifications (Figures 6.4(b) and 7.5(a) for stages 1 and 2, respectively).

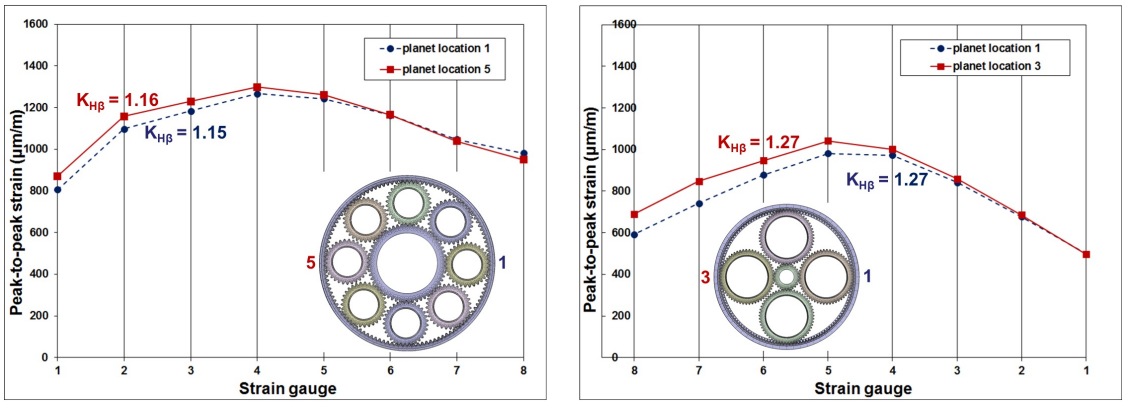

(a) (b)

Figure 7.8: Load distribution across the W3600 ring facewidths with $K_{H\beta}$ shown for the design with added bearings, more flexible annulus, and lead modifications for: (a) stage 1, and (b) stage 2.

7.4 W2000: Effects of Planet Lead Modifications

Planet lead modifications are investigated on both epicyclic stages of the W2000. The lead modifications consist of 20 μm crowning and 50 μm edge relief on the stage 1 planets and 15 μm crowning and 35 μm edge relief on the stage 2 planets. In order to compare the tooth load distributions to the original design, plots showing computational peak-to-peak strain across the stage 1 and 2 ring facewidths are given in Figures 7.9(a) and 7.9(b), respectively. Once again, the lead crowning shifts the contact pressure toeards the centers of the ring teeth and yields slightly higher $K_{H\beta}$ values than original design with no lead modifications (shown in Figures 6.6(b) and 6.5(b) for stages 1 and 2, respectively).

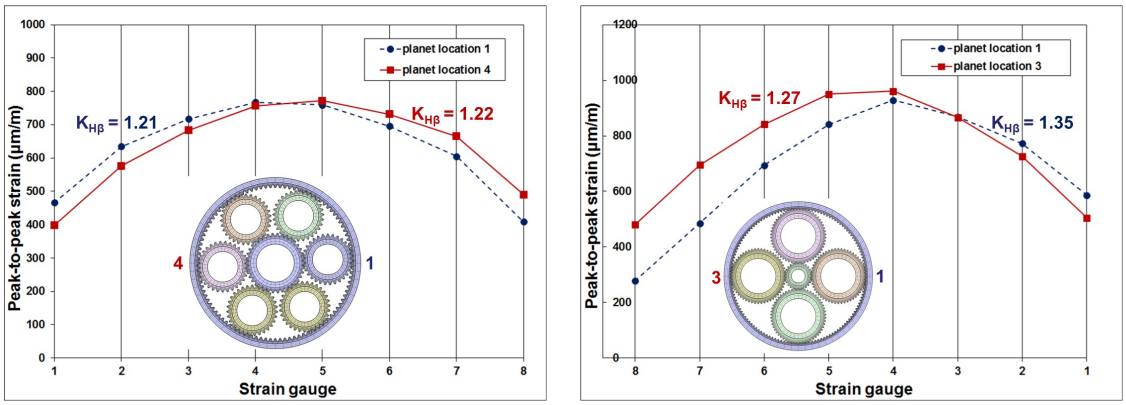

(a) (b)

Figure 7.9: Load distribution across the W2000 ring facewidths with $K_{H\beta}$ shown for the design with added lead modifications for: (a) stage 1 and (b) stage 2.

7.5 FC5500: Effects of Removing Pin Tilting Error and Reducing Eccentricity

As discussed in Chapter 5, the eccentricity of the main rotor shaft and pin tilting errors in both stages of the FC5500 gear train contribute to uneven tooth load distribution. In particular, radial deflection of the end of the pin shifts the load distribution towards the constrained end of the stage 1 ring and towards the free end of the stage 2 ring.

Simulations were run for both stages with no pin tilting error and half of the unloaded bearing deformation values discussed in Chapter 5. In theory, the eccentricity of the main rotor shaft could be reduced in the actual gear train by reducing bearing clearance values or by manufacturing the housing such that the bearings are mounted slightly upward (in the direction opposite gravity) to counteract the misalignment of the main rotor shaft.

Figures 7.10(a) and 7.10(b) show the tooth load distribution and $K_{H\beta}$ values for stages 1 and 2, respectively with no pin tilting error and half of the eccentricity discussed in Chapter 5. These figures can be compared to the computational results from the model with eccentricity and pin tilting errors in Figures 6.8(b) and 6.7(b), respectively.

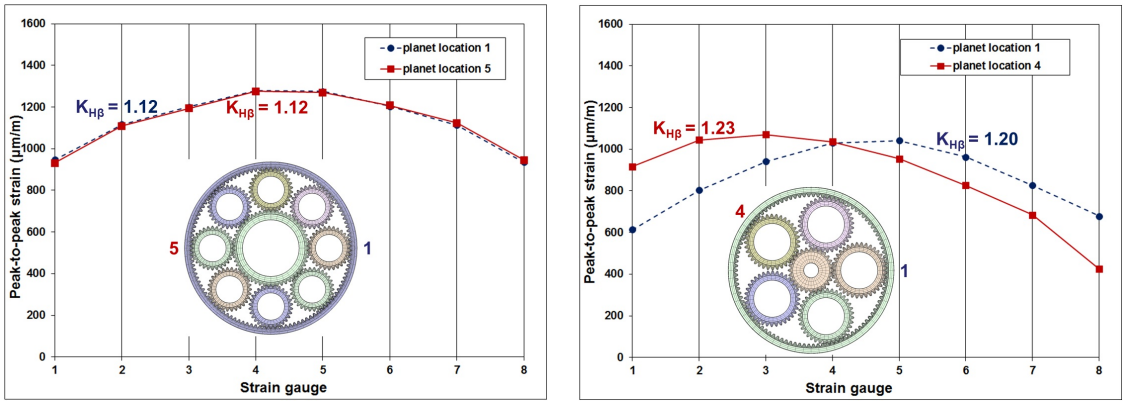

(a) (b)

Figure 7.10: Load distribution across the FC5500 ring facewidths with $K_{H\beta}$ shown for the design with reduced eccentricity and no pin tilting errors for: (a) stage 1 and (b) stage 2.

Eliminating pin tilting error improves the load distribution across the ring teeth of both stages. $K_{H\beta}$ for stage 1 improved from 1.17 and 1.18 to 1.12. $K_{H\beta}$ values for this design from stage 2 are 1.23 and 1.20. The elimination of pin tilting error improved the load distribution for the mesh inclination that is loaded more towards the free end. This is logical because the end of the pin opposite the carrier is no longer deflecting in the radial direction. Planet load sharing factor calculated from these simulation is 1.01 and 1.027 for stages 1 and 2, respectively. These results indicate that eliminating

pin tilting errors would likely improve the load distribution across the ring teeth of both stages. Reducing eccentricity in the finite element/contact mechanics model improves planet load sharing.

Chapter 8: CONCLUSIONS

In this thesis, complete three dimensional finite element/contact mechanics models of Orbital2 flexible pin, multi-stage, planetary wind turbine gear trains were constructed and compared to full system experiments. These models include finite element housings, finite element carriers and drive flanges, finite element models of flexpins implemented in both planetary stages, and accurate modeling of the contacting gear teeth using a multi-body contact solver. Root strain from the rings of both planetary stages in each gear train was compared to experimental root strain, and in general there was good agreement. Certain behavior observed in the experiments, such as the variation in strain characteristics across ring gear facewidths, was duplicated with the finite element models and discussed in detail. Modulation in strain observed in the experiments was also captured by the finite element/contact mechanics models and examined in depth. Manufacturing errors such as eccentricity and pin tilting errors were implemented in the computational models. Measures of system performance such as load distribution factor across ring tooth facewidths ($K_{H\beta}$) and planet load sharing factor (K_{γ}) were discussed and investigated experimentally and using root strain from the finite element/contact mechanics models. Planet load sharing in all systems was good. Design changes including component geometry changes,

the addition of bearings, and the effects of planet lead modifications were also investigated using the computational models.

Experimental and computational strain was evaluated at eight locations across the facewidth in the root of each ring tooth. A sensitivity study indicates that strain is very sensitive to gauge position in the profile direction. At each strain gauge location across the ring facewidth, root strain was averaged at three positions in the profile direction corresponding to the dimensions of the strain gauges. In the interest of computational efficiency, simulations for both planetary stages in each gear train were examined at 20 different configurations over a mesh cycle. Root strain was then extracted from each tooth using a Multyx script. This data was then processed to reconstruct a strain signal for given planet locations the entire way around the ring. This method is much more efficient than running each planetary stage for multiple mesh cycles and multiple planet passes. The use of these scripts was verified by running simulations over a ring revolution that yielded consistent behavior in root strain. In general, the shapes and peak-to-peak values of computational root strain are consistent with the experimental results.

The modulation observed in experimental strain signals was captured by the finite element/contact mechanics models. Spectra of experimental strain signals yields sidebands about the planet pass frequency (ω_{pp}) at plus and minus the speed of the ring gear ($\pm\omega_r$). This indicates that the modulation observed is related to the revolution of the instrumented ring tooth. The presence of similar sidebands was detected in the spectra of computational strain for simulations run over a ring revolution, confirming that the modulation is related to the rotation of the ring gear and that the computational models are behaving similarly to the actual systems. Finite element/contact

mechanics model simulations with no eccentricity show only a slight modulation due to gravity. While gravity contributes to modulation, carrier and main rotor shaft eccentricity enhance the modulation in strain observed over a ring revolution at the constrained end of the stage 2 ring in the W3600 and FC5500 gear trains. Adding eccentricity of the main rotor shaft to the computational models yields better correlation to the experiments for the W3600 and FC5500 gear trains. It is likely that this type of misalignment is present in the actual gear trains and could be caused by manufacturing errors or bearing clearances. Computational results indicate that the W2000 gear train is less sensitive to eccentricity in part due to system configuration and boundary conditions. Pin tilting errors were modeled in the FC5500 gear train and contribute to the uneven tooth load distribution observed in the experiments. Including pin tilting errors and eccentricity in this gear train gives good agreement with experiments.

Measures of system performance such as tooth load distribution factor ($K_{H\beta}$) and planet load sharing factor (K_{γ}) were examined using peak-to-peak strain from the finite element/contact mechanics models and compared to the experiments. Two extremes of planet-ring mesh inclination were observed in the experimental results for stage 2 in each gear train. The most extreme cases were exhibited for the W3600 and FC5500 gear trains. These different mesh inclinations became apparent in the finite element/contact mechanics models of the W3600 and FC5500 gear trains with the inclusion of eccentricity. The extremes occur in the computational models on opposite sides of the ring gear near three and nine o'clock.

Design changes were investigated for each gear train. It was determined that uneven loading of the W3600 stage 2 ring teeth when a planet tooth meshes with a

ring tooth was due in part to local deformation of the ring into a conical shape because of differing constraints on the two sides of the teeth. A more compliant design for the W3600 stage 2 annulus was investigated with holes added in the annulus. This design successfully reduces variation in strain characteristics across the facewidth of the ring because the annulus bends more than the original design when a planet tooth meshes with a ring tooth. Holes are included on the annuli of the W2000 and FC5500 gear trains. The addition of bearings to the stage 1 sun-drive flange 2 subassembly in the W3600 gear train was quantified and discussed for models with and without eccentricity. For this design bearing clearances must be carefully considered to avoid certain bearings being unloaded during operation. Simulations for the FC5500 were investigated with pin tilting errors removed and less eccentricity. Results from these simulations suggest that eliminating pin tilting errors and controlling eccentricity by possibly limiting bearing clearances improves tooth load distribution and planet load sharing. The effects of planet lead modifications were also examined in both the W3600 and W2000 systems.

The comprehensive engineering investigations contained herein show the complexity of Orbital2 gear train designs and showcase the advantages of using a sophisticated multi-body contact solver to understand system behavior and make comparisons to full system experiments. The complete, multi-stage three dimensional models examined capture system behavior such as component deflections due to gravity and eccentricity and variation in gear tooth contact force across tooth facecwidths. Computational models, such as the ones investigated herein, are extremely valuable design tools when attempting to understand and improve complex gear train designs such as the ones designed by Orbital2.

8.1 Future Work

Future work pertaining to the gear trains discussed herein might involve modeling the rolling element bearings to accurately capture the contact at the rollers. Investigating system behavior with actual bearing clearance values implemented could lead to a better understanding of how bearing clearances effect misalignments in a gear train. Modeling rolling element bearings would increase computation times and would require careful selection of contact parameters on the rollers in order to make simulations feasible.

Studying different ways to model the connection at the pin-carrier interface in the finite element/contact mechanics models might also provide valuable insight into the behavior of flexpins. Studying the behavior of press-fit connections at the pin-carrier interface would be feasible using the finite element/contact mechanics software used herein by combining a Fourier surface connection with a defined contact pair. At a press-fit connection, deformations in axial and circumferential directions could be calculated using Fourier surface displacement interpolation. Radial deflections could be calculated using a contact definitions that would consider pre-tension and surface penetration.

Investigating the dynamics of each gear train using lumped parameter models might also be considered. System natural frequencies and mode shapes could be investigated. Finite element/contact mechanics models could be analyzed dynamically using frequency domain calculation methods as discussed by Cooley, Parker, and Vijayakar in a recent study [50]. This formulation could make dynamic analyses of gear

trains with multiple active meshes computationally feasible and could potentially decrease simulation time by two orders of magnitude when compared to numerically integrated dynamic response calculations [50].

Appendix A: APPROXIMATE BEARING STIFFNESSES

Bearing connections in each gear train are defined by specifying radial (K_r), axial (K_z), and tilting stiffness ($K_{\theta r}$) values. These locations include the planet bearings and the bearings that connect the main rotor shaft to the housing. Each model contains an additional bearing at the stage 2 sun shaft-stage 3 wheel shaft interface to simulate a spline connection at this location. While Calyx has the ability to model true spline connections, in the interest of simplicity and computational efficiency it was determined that simply defining appropriate stiffness values was sufficient. Implementation of a true spline connection would require contact at each spline tooth and would increase simulation time. In order to replicate the behavior of the spline connection, large torsional and radial stiffness values were used at this location with very little bending and axial stiffness. Figure A.1(a) shows a cutaway view of the stage 2 sun shaft and the stage 3 wheel and the location of the bearing connection in the W3600 model. Figure A.1(b) shows the same cutaway view with exaggerated deformation.

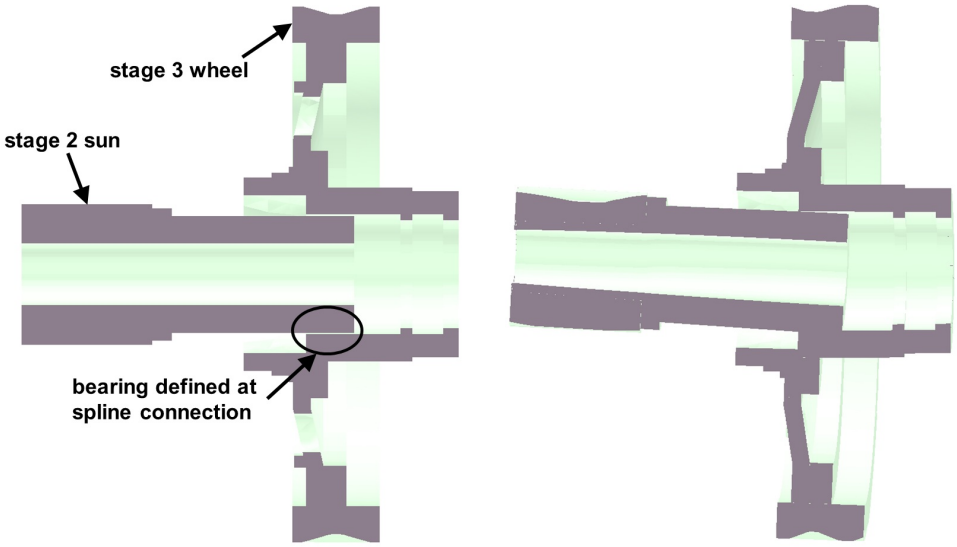

Figure A.1: Cutaway view of the stage 2 sun and stage 3 wheel on the W3600 connected by a bearing that simulates the spline connection: (a) undeformed, and (b) with exaggerated deformation.

The low stiffness in the bending direction allows the two shafts to tilt almost independent of one another. The connection decouples the tilting motion of the shafts and simulates the behavior of the spline. Capturing this type of behavior is important when gravity and system eccentricities are considered. The same spline modeling is used for the W2000 and the FC5500 models.

When defining large bearing stiffness values in certain degrees of freedom relative to other stiffnesses in the system, it is sometimes necessary to adjust a parameter in Calyx known as the free mode threshold. In order to determine if a deformation mode of a multibody system is a free mode or a stiff mode, Calyx compares the stiffness matrix eigenvalue of that mode to the largest system stiffness matrix eigenvalue. If it is less than the free mode threshold value times the largest eigenvalue, then it is

considered a free mode. When the bearing at the spline connection was introduced to each model, the free mode threshold needed to be adjusted so the contact solver could properly equilibrate rigid body modes. Figures A.2(a) and A.2(b) show the location of the spline connection in the W2000 and FC5500 respectively.

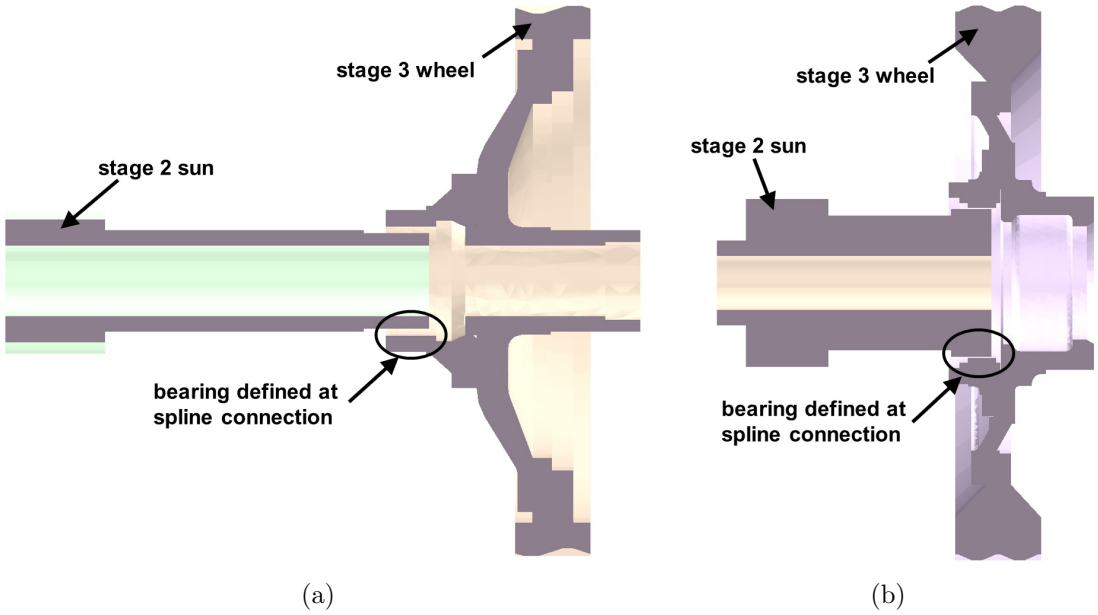

(a) (b)

Figure A.2: Cutaway view of the stage 2 sun and stage 3 wheel connected by a bearing that simulates the spline connection for: (a) the W2000, and (b) the FC5500.

Appendix B: TOOTH MODIFICATIONS

B.1 Tip Modifications

In Calyx, both linear and quadratic tip modifications can be implemented by simply defining the magnitude and starting roll angle of the modification. The starting roll angle (SRA) is calculated using Equation B.1 as given in [7]. d_b denotes the base diameter and d_{mod} represents the diameter to the start of the modification. The starting roll angle is measured in degrees.

$$SRA = tan\left[cos^{-1}\left(\frac{d_b}{d_{mod}}\right)\right]\left(\frac{180}{\pi}\right) \tag{B.1}$$

B.2 Lead Modifications

Lead crowning and tabular lead modifications can be successfully implemented in Calyx as shown in Figures 2.10(c) and 2.10(d). To define parabolic crowning it is only necessary to define the amount of material that is removed at the tooth edges. When defining non-symmetric lead modifications, the material removed must be defined in a tabular manner. This means that a distance across the tooth facewidth (zeta) and and the corresponding amount of material removed (magnitude) must be specified.

Appendix C: MATERIAL PROPERTIES

The system material properties defined in the computational models discussed in this thesis are elastic modulus (E), Poisson's ratio (ν), and density (ρ). Each model consists of either steel or cast iron components. The material properties for these two materials are given in Table C.1. Elastic modulus is given in MPa. This unit is appropriate to use in Calyx because it equals N/mm^2. Poisson's ratio is dimensionless. The units assigned to density must be manipulated before including them in each model. I order to maintain consistency with the system units of Newtons (N), millimeters (mm), and seconds (s), density must be converted to Ns^2/mm^4. This conversion can be accomplished by simply multiplying density in Kg/m^3, as shown in the fourth column of Table C.1, by 1E-12.

Table C.1: System material properties

Material	Elastic Modulus (MPa)	Poisson's Ratio	Density (Kg/m^3)
Steel	206000	0.3	7850
Cast Iron	169000	0.275	7100

In each model, all of the gears, shafts, flexible pins, carriers and ring rims are made of steel. The drive flanges, support plates, and housings are made of cast iron.

Material properties are either defined in Calyx for internally meshed components or assigned to the appropriate elements in Patran for externally meshed components.

Appendix D: EXPERIMENTAL STRAIN PLOTS

D.1 W3600 Experimental Strain

D.1.1 Stage 1 Strain

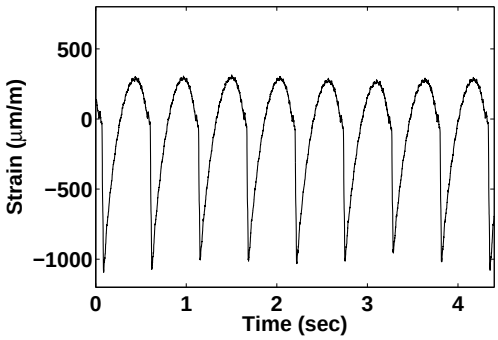

Figure D.1: W3600 stage 1: experimental strain from gauge 1.

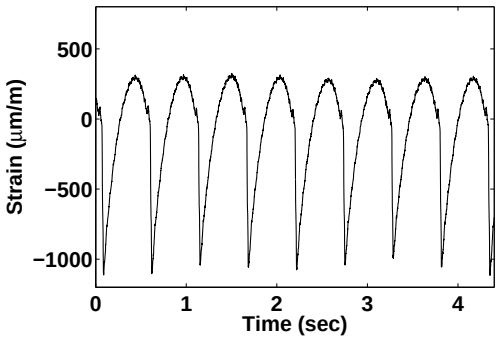

Figure D.2: W3600 stage 1: experimental strain from gauge 2.

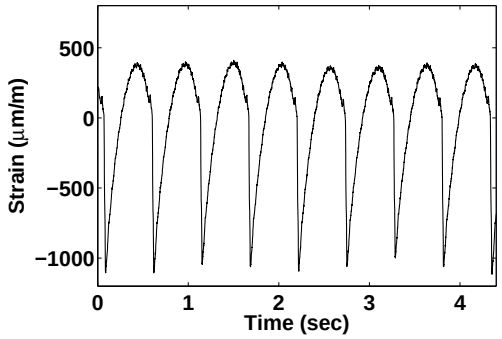

Figure D.3: W3600 stage 1: experimental strain from gauge 3.

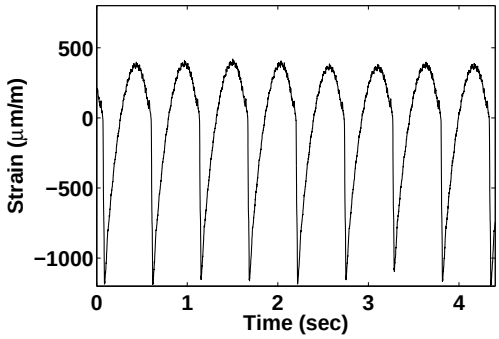

Figure D.4: W3600 stage 1: experimental strain from gauge 4.

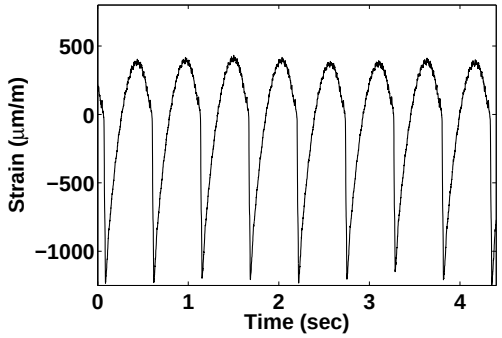

Figure D.5: W3600 stage 1: experimental strain from gauge 5.

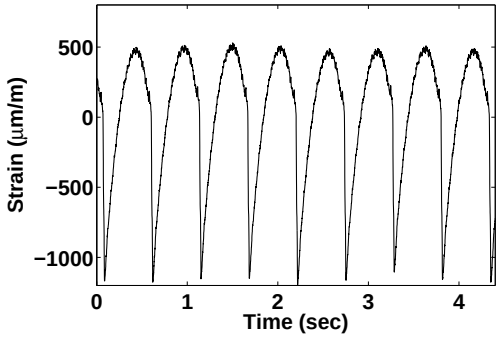

Figure D.6: W3600 stage 1: experimental strain from gauge 6.

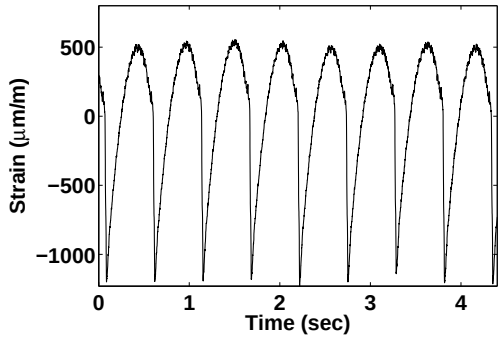

Figure D.7: W3600 stage 1: experimental strain from gauge 7.

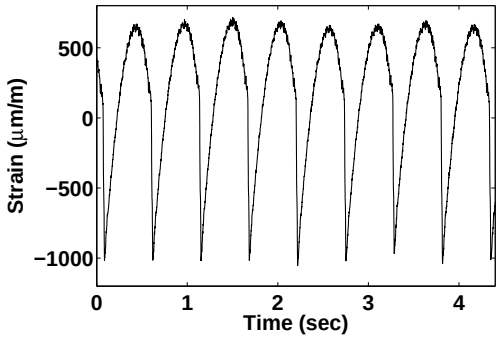

Figure D.8: W3600 stage 1: experimental strain from gauge 8.

D.1.2 Stage 2 Strain

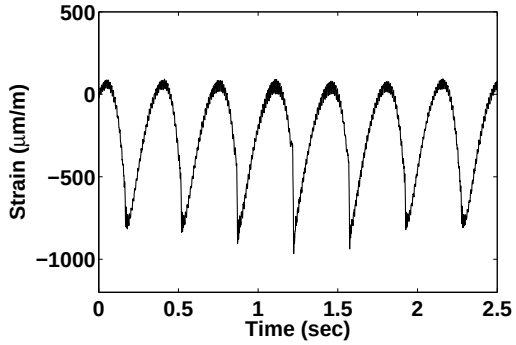

Figure D.9: W3600 stage 2: experimental strain from gauge 1.

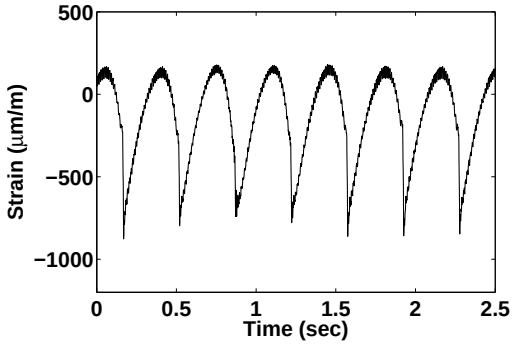

Figure D.10: W3600 stage 2: experimental strain from gauge 2.

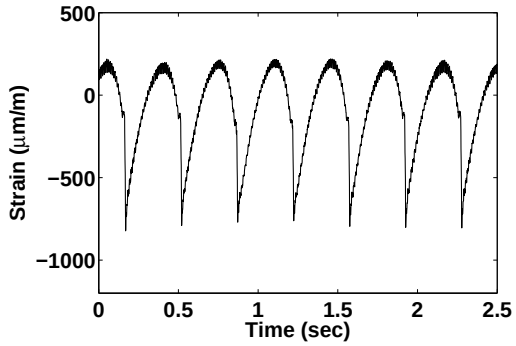

Figure D.11: W3600 stage 2: experimental strain from gauge 3.

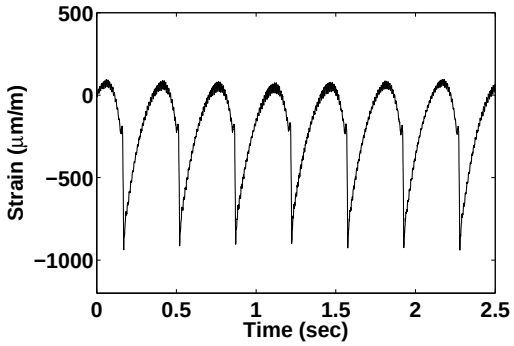

Figure D.12: W3600 stage 2: experimental strain from gauge 4.

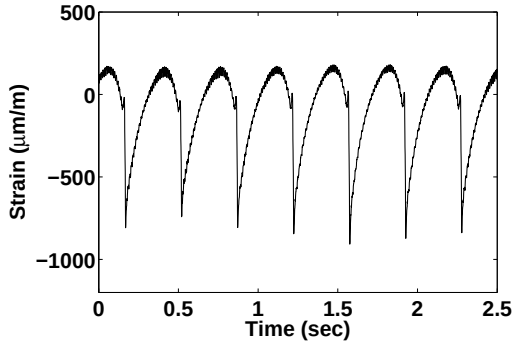

Figure D.13: W3600 stage 2: experimental strain from gauge 5.

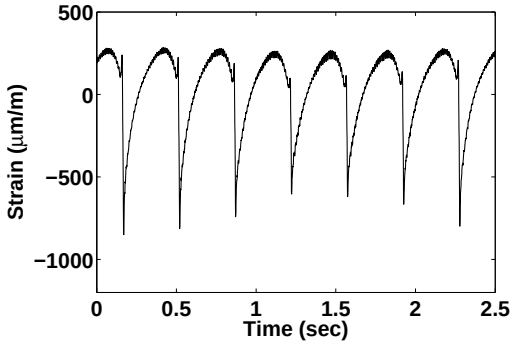

Figure D.14: W3600 stage 2: experimental strain from gauge 6.

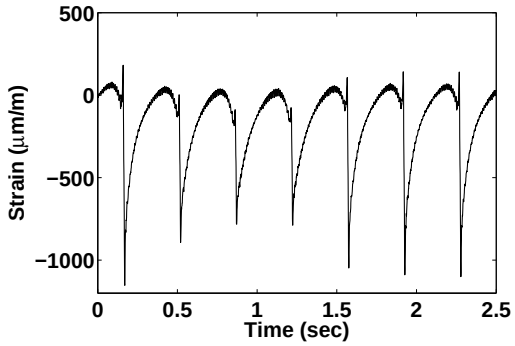

Figure D.15: W3600 stage 2: experimental strain from gauge 7.

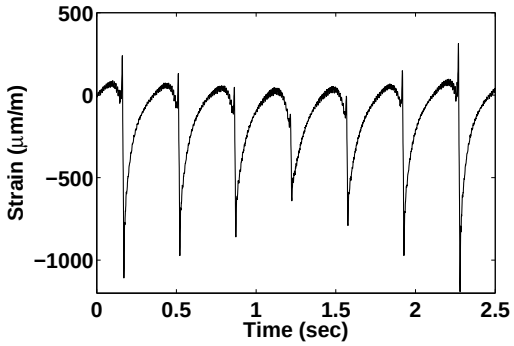

Figure D.16: W3600 stage 2: experimental strain from gauge 8.

D.2 W2000 Experimental Strain

D.2.1 Stage 1 Strain

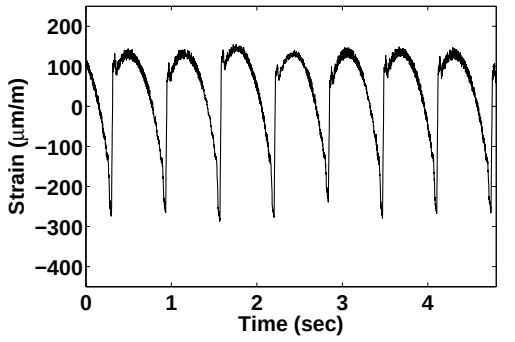

Figure D.17: W2000 stage 1: experimental strain from gauge 1.

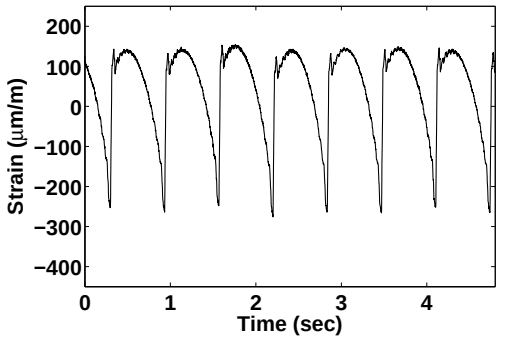

Figure D.18: W2000 stage 1: experimental strain from gauge 4.

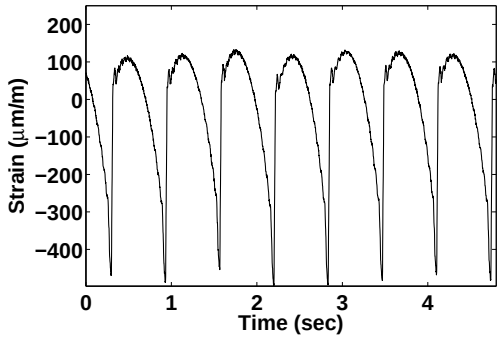

Figure D.19: W2000 stage 1: experimental strain from gauge 5.

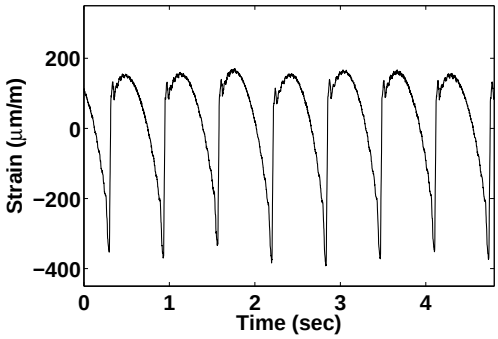

Figure D.20: W2000 stage 1: experimental strain from gauge 6.

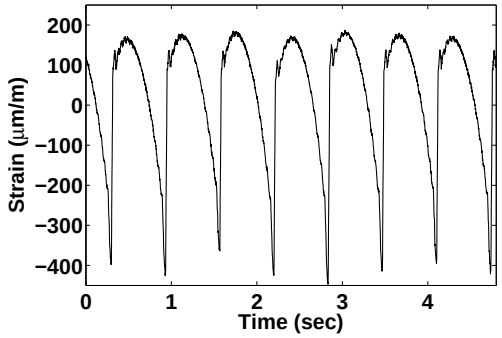

Figure D.21: W2000 stage 1: experimental strain from gauge 7.

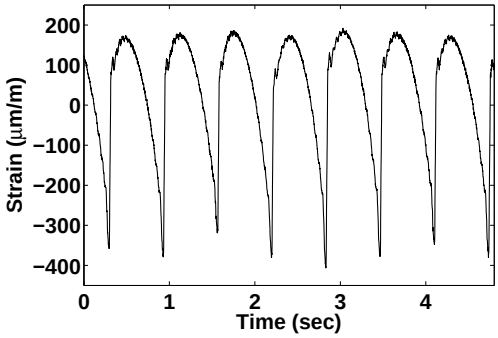

Figure D.22: W2000 stage 1: experimental strain from gauge 8.

D.2.2 Stage 2 Strain

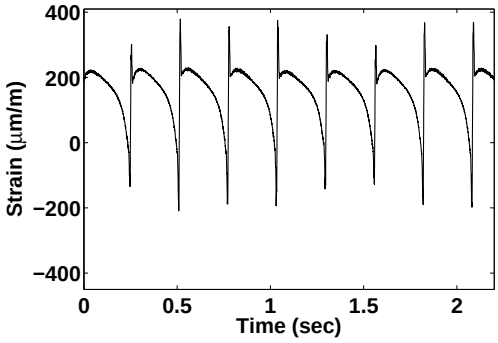

Figure D.23: W2000 stage 2: experimental strain from gauge 1.

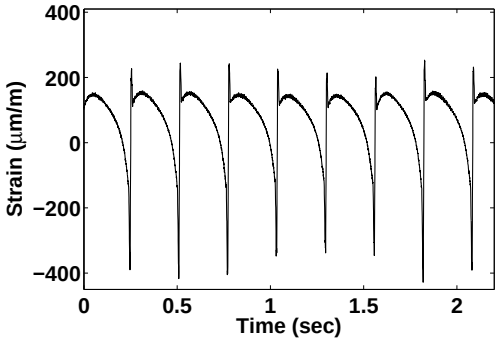

Figure D.24: W2000 stage 2: experimental strain from gauge 2.

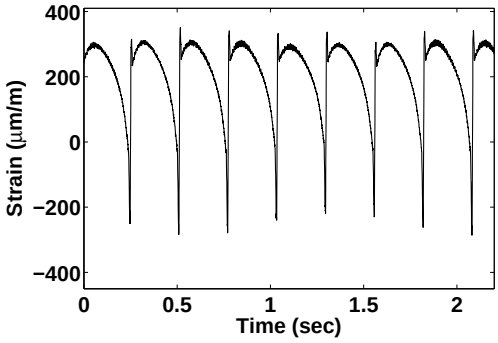

Figure D.25: W2000 stage 2: experimental strain from gauge 3.

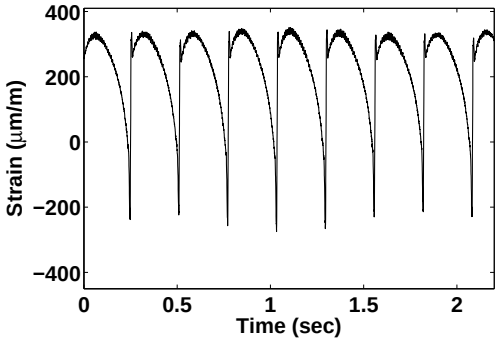

Figure D.26: W2000 stage 2: experimental strain from gauge 4.

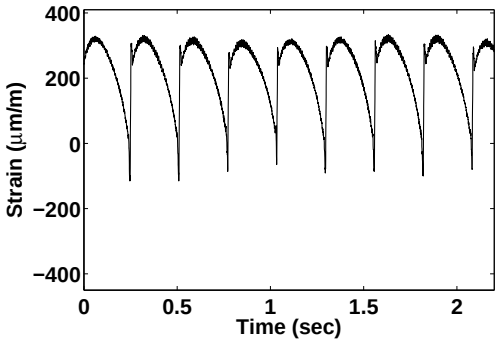

Figure D.27: W2000 stage 2: experimental strain from gauge 5.

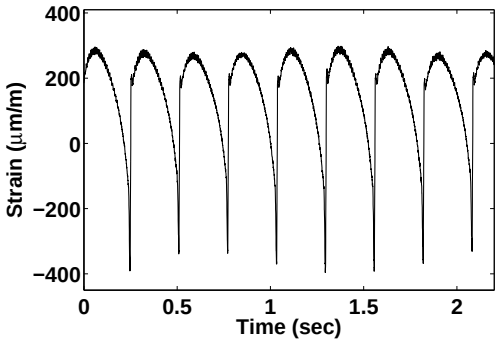

Figure D.28: W2000 stage 2: experimental strain from gauge 6.

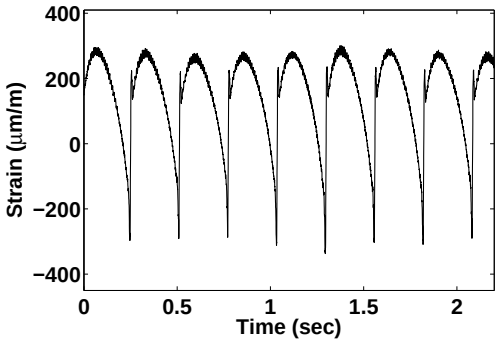

Figure D.29: W2000 stage 2: experimental strain from gauge 7.

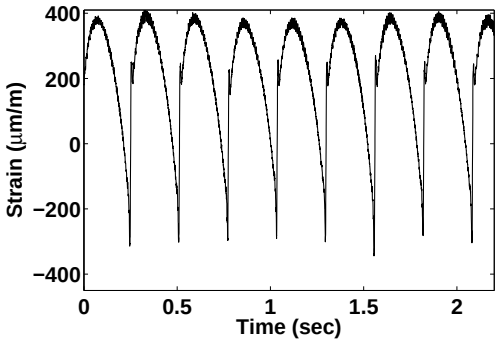

Figure D.30: W2000 stage 2: experimental strain from gauge 8.

D.3 FC5500 Experimental Strain

D.3.1 Stage 1 Strain

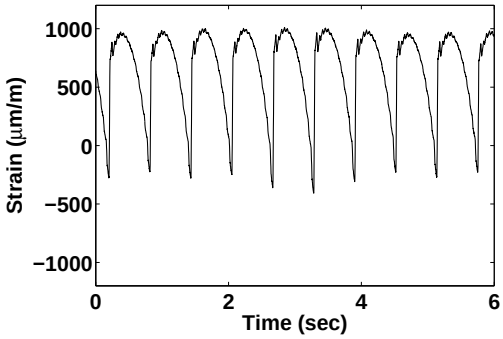

Figure D.31: FC5500 stage 1: experimental strain from gauge 1.

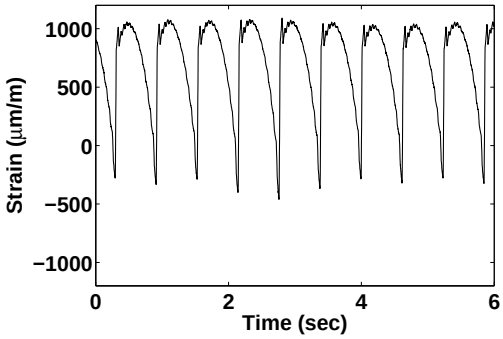

Figure D.32: FC5500 stage 1: experimental strain from gauge 2.

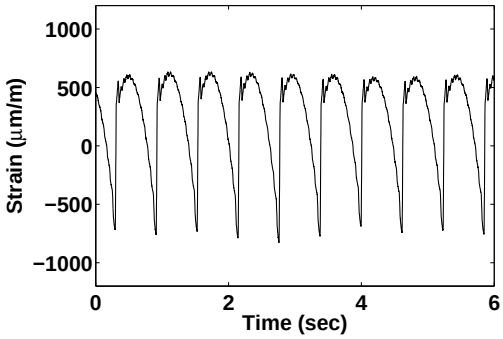

Figure D.33: FC5500 stage 1: experimental strain from gauge 4.

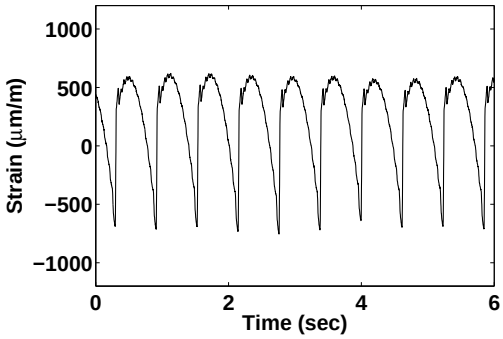

Figure D.34: FC5500 stage 1: experimental strain from gauge 5.

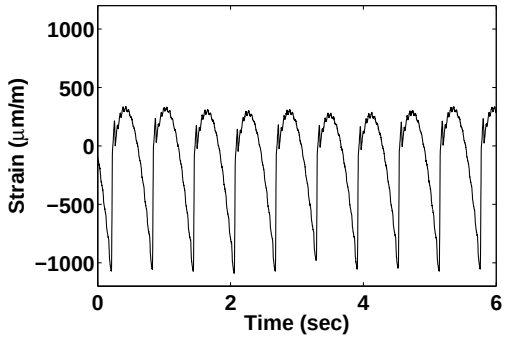

Figure D.35: FC5500 stage 1: experimental strain from gauge 6.

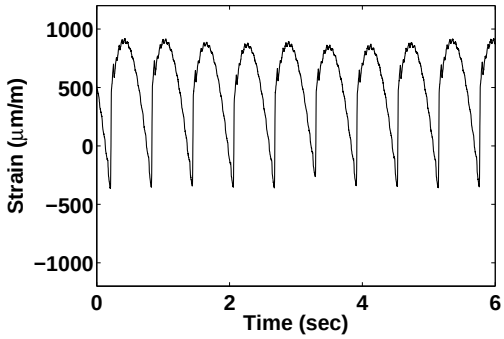

Figure D.36: FC5500 stage 1: experimental strain from gauge 7.

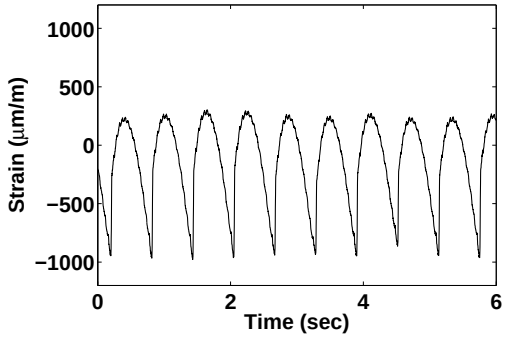

Figure D.37: FC5500 stage 1: experimental strain from gauge 8.

D.3.2 Stage 2 Strain

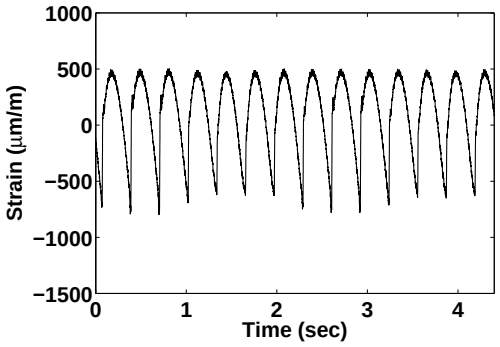

Figure D.38: FC5500 stage 2: experimental strain from gauge 1.

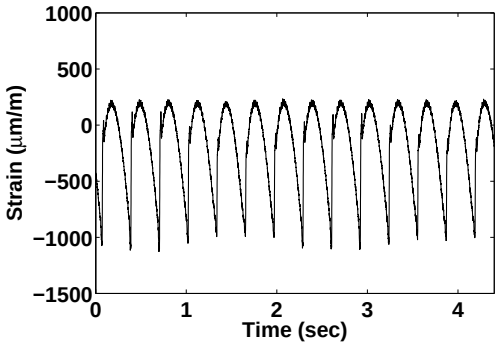

Figure D.39: FC5500 stage 2: experimental strain from gauge 2.

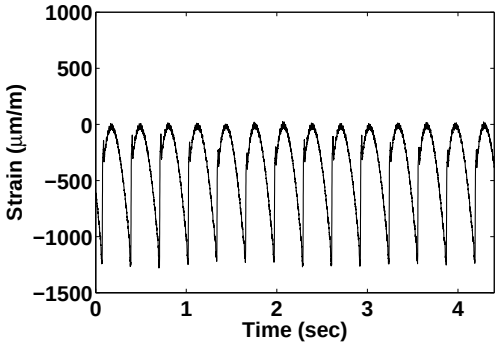

Figure D.40: FC5500 stage 2: experimental strain from gauge 3.

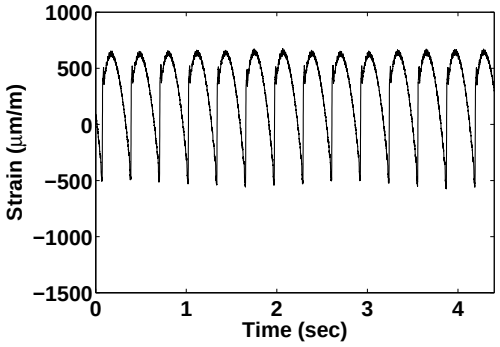

Figure D.41: FC5500 stage 2: experimental strain from gauge 4.

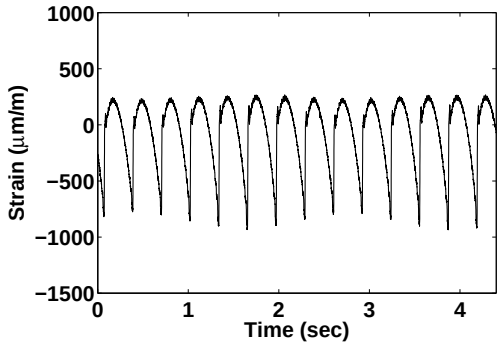

Figure D.42: FC5500 stage 2: experimental strain from gauge 5.

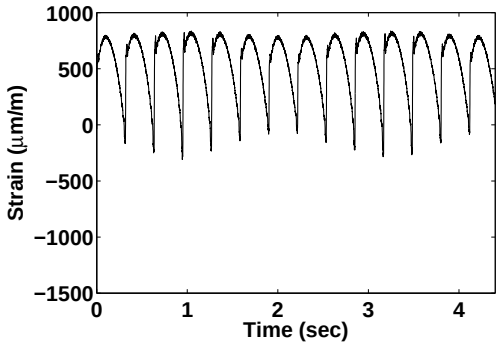

Figure D.43: FC5500 stage 2: experimental strain from gauge 6.

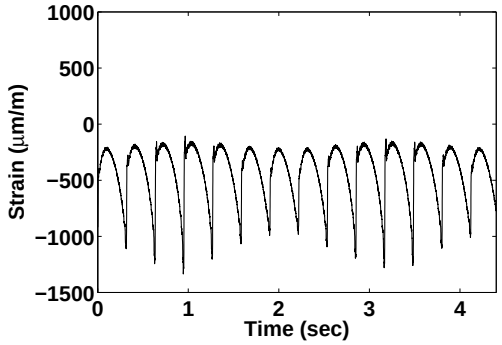

Figure D.44: FC5500 stage 2: experimental strain from gauge 7.

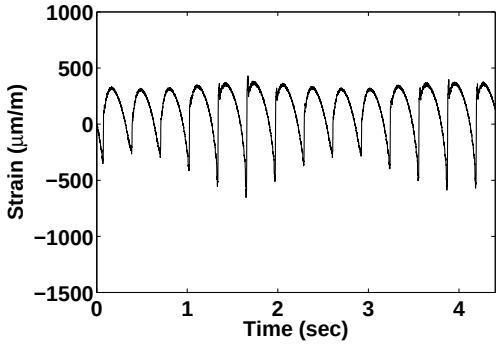

Figure D.45: FC5500 stage 2: experimental strain from gauge 8.

Appendix E: MULTYX MENUS IN THE GUIDE USER INTERFACE

This appendix documents the Multyx menus in the Guide user interface. Understanding how to use these menus is essential when constructing large three dimensional models in Calyx. Gear, shaft, bearing, and general system parameters are all specified using these menus. Figure E.1 shows the main menu in Guide and the first menu that appears when opening the program.

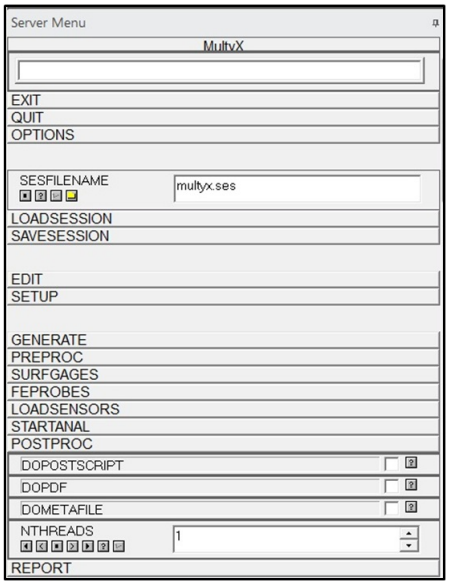

Figure E.1: View of the main menu in Guide.

Here, the session file can be specified (SESFILENAME), loaded (LOADSESSION), and saved (SAVESESSION). There are buttons that lead to the setup and edit menu and buttons to pre-process (PREPROC), start an analysis (STARTANAL), and post-process (POSTPROC) the model. The number of threads used in the analysis (NTHREADS) can also be specified. The QUIT command terminates the program and does not save data to the session file. The exit command writes data to the session file and then terminates the program. Every menu in Guide has the QUIT and EXIT command at the top. Selecting quit will bring the user back to the previous menu and will not save any changes. Selecting EXIT saves any changes and then brings the user back to the previous menu.

Figure E.2 shows the setup menu. This menu gives the user control over general model parameters. Here, the initial time (INITIALTIME), delta time (DELTATIME), and the number of time steps (NTIMESTEPS) can be specified as well as the solution method (SOLMETHOD). The analyses discussed herein are all static. The post-process file name (POSTFILENAME) can be specified. The FREEMODETHRESHOLD (discussed in Appendix A) is specified in the setup menu. The Calyx verbosity can also be defined (a number between one and five). This parameter dictates the amount of information that Calyx gives to the user during a simulation. A value of one gives the least amount of information and a value of five gives the most. Increasing the verbosity level is useful when debugging a model because it gives more information about the calculations taking place, thus making it easier for the user to pinpoint potential errors.

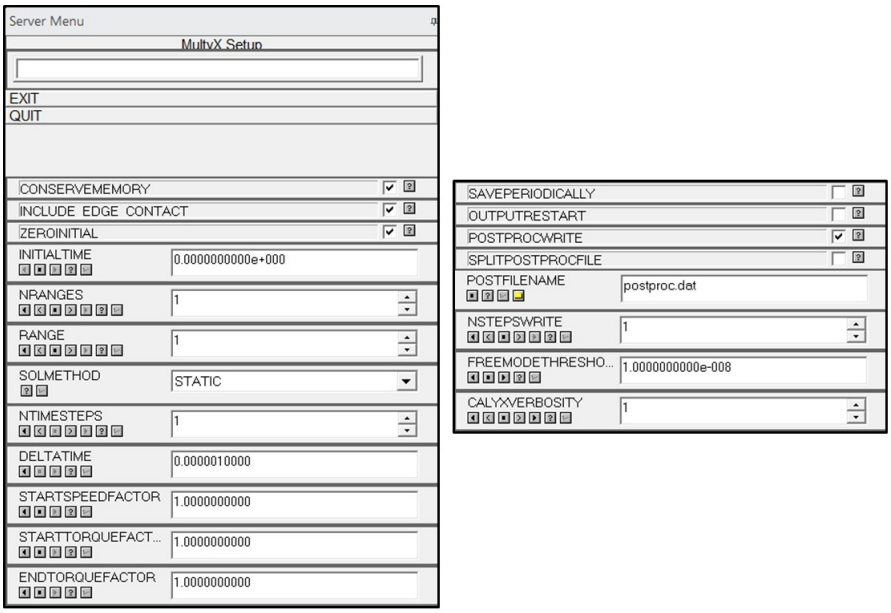

Figure E.2: View of the setup menu in Guide.

Figure E.3 shows the edit menu. The number of rotors (NROTORS), housings (NHOUSINGS), and connectors (NCONNECTORS) can be specified in this menu. There are also buttons that lead to the pairs, housing, connector and rotor menus. At the bottom of the edit menu a body force can be specified. The body force is defined by specifying a magnitude times $e1$, $e2$, or $e3$. This infers that the force is applied in the x, y, or z direction relative to the global reference frame, respectively. If the USEMODULE box is checked at the bottom of the edit menu, then the module is defined in the gear tooth menus for the entire system in stead of the pitch diameter. A system description can also be entered for user convenience.

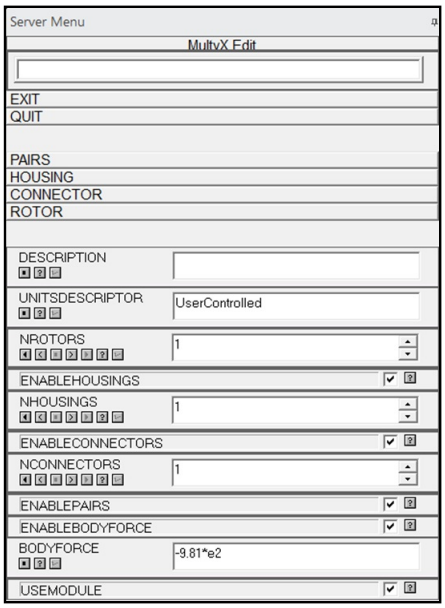

Figure E.3: View of the edit menu in Guide.

The pairs menu is shown in Figure E.4. All contact parameter definitions for each contact pair are prescribed in this menu. All possible combinations of contact pairs are shown in the TYPE drop-down menu. The separation tolerance (SEPTOL), number of grid cells in the profile direction (NPROFDIVS), the length of each cell in the profile direction (DSPROF), and the number of grid cells in the facewidth direction (NFACEDIVS) are specified here for each contact pair. The rotor number and gear for each respective gear body is defined at the bottom of the menu. A coefficient of Coulomb friction (MU) can be specified and contact on the back side of the teeth can be turned on using the BACKCONTACT command.

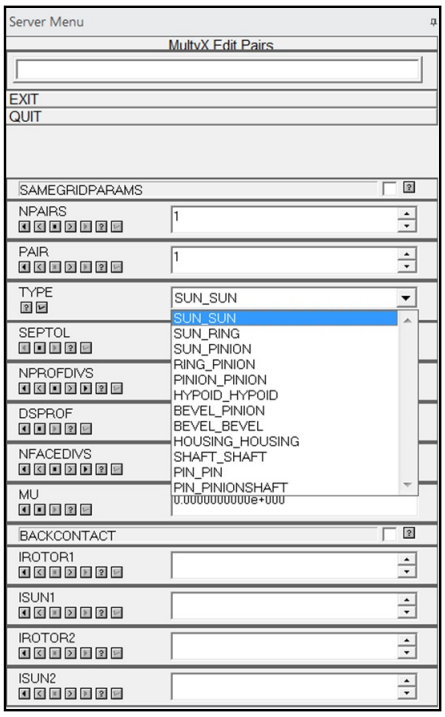

Figure E.4: View of the pairs menu in Guide.

Figure E.5 shows the connector menu. The type of member for the inner and outer races (MEMBER1TYPE and MEMBER2TYPE) is defined in this menu. The choices for member type are rotor, housing, or ground. The diameter of each race (DIARACE1 and DIARACE2) is specified as well as the axial position of the back and front of the race (AXPOSN1RACE and AXPOSN2RACE). These axial positions are measured from relative to the origin of the connector defined using the XPOS, YPOS, and ZPOS commands. The AX, AY, and AZ commands define the components of the vector that defines the orientation of the connector axis. This vector must be a unit vector. The REFERENCE_RACE command allows the user to select the reference race as the inner or outer. Bearing deflections, reactions forces, unloaded

deformations, and undeformed loads will be defined in the reference frame of this race. For example, if the outer race is the reference race, unloaded bearing deformations are applied to the inner race relative to the outer race, in the outer race's reference frame.

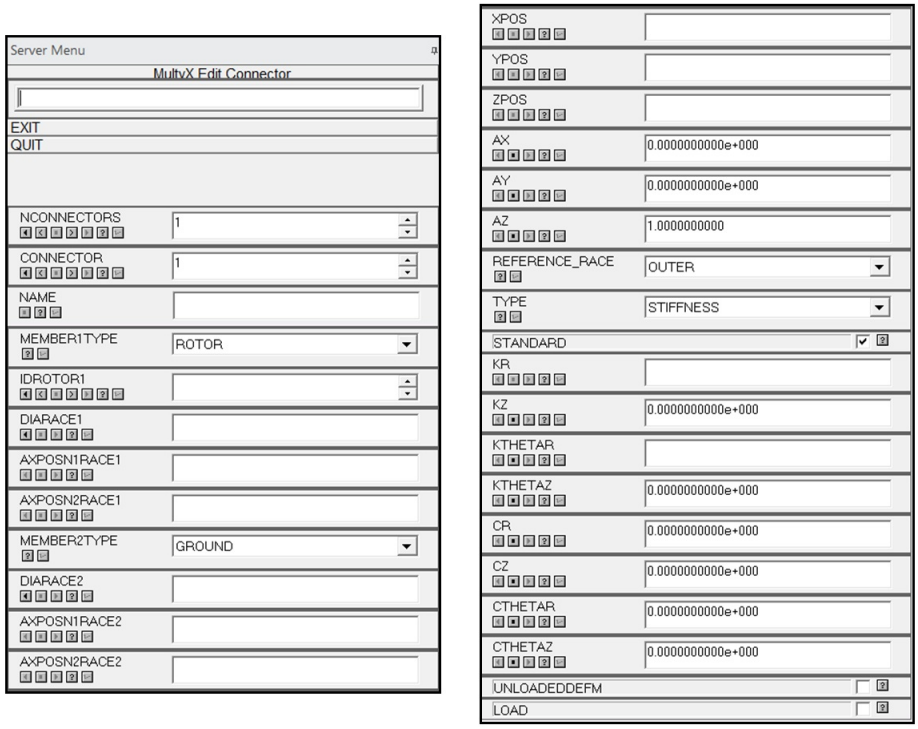

Figure E.5: View of the connector menu in Guide.

The type of connector (TYPE) is specified as a stiffness matrix (STIFFNESS), an internal spline with contact (INTERNALSPLINED), an external spline with contact (EXTERNALSPLINED), a roller bearing with contact at the rolling elements (ROLLERS), a journal bearing with surface contact (JOURNAL), or a socket joint

(TRIPOD). Figure E.5 shows the required parameters for a stiffness matrix. As discussed in Appendix A, the radial (KR), axial (KZ), tilting stiffness (KTHETAR), and torsional stiffness (KTHETAZ) values can be specified. Damping values in the same degrees of freedom can be assigned also.

The rotor menu is shown in Figure E.6. The carrier, ring gear, sun gear, bevel gear, hypoid gear and shaft menus can all be accesed at the top of the rotor menu. The origin of a rotor is defined using the XPOSN, YPOSN, and ZPOSN commands. The AX, AY, and AZ inputs define a unit vector in the direction of the z axis of the rotor relative to the global reference frame. As discussed in Chapter 3, a rotor can be of five types (INPUT, OUTPUT, IDLER, INACTIVE, or ATTACHEDTOHOUSING). At the bottom of the rotor menu, constraints are specified in the x, y, z, θ_x, and θ_y directions. For input rotors an initial rotation (THETAZ) can also be defined.

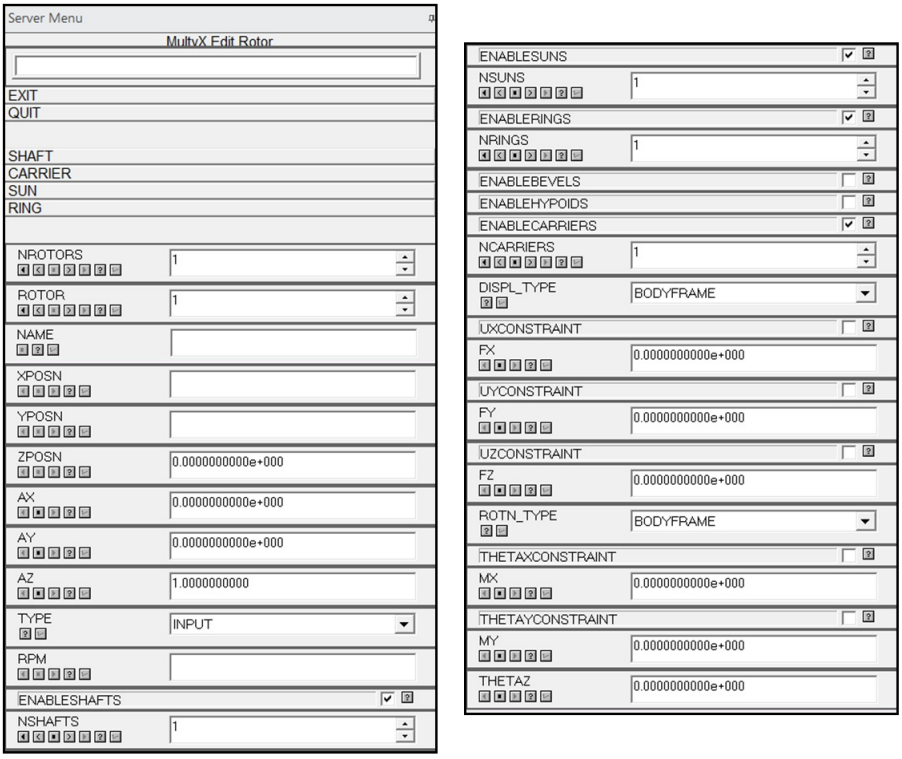

Figure E.6: View of the rotor menu in Guide.

Figure E.7 shows the shaft menu. Here, the number of shafts (NSHAFTS) can be specified for a given rotor. The type of shaft is defined by defining geometry (DEFINEGEOMETRY), or by importing a mesh file, command file, or a stiffness matrix file. All shafts used in the gear train models discussed herein were constructed by defining their geometry. The AXIALPOSNSHAFT command defines the location of the front of the first shaft segment relative to the origin of the rotor. The UNIFORMMATERIAL option controls whether or not each shaft segment is made of the same material. Material properties such as Young's modulus, Poisson's ratio, and density are defined in the shaft menu as well as the α and β values used in the Raleigh damping model

(RALEIGHALPHA and RALEIGHBETA respectively). The Raleigh damping model assumes that a damping matrix C for a element follows $C = \alpha * \mathbf{M} + \beta * \mathbf{K}$ where $\mathbf{M}$ and $\mathbf{K}$ are the mass and stiffness matrix respectively. The default values are shown in Figure E.7.

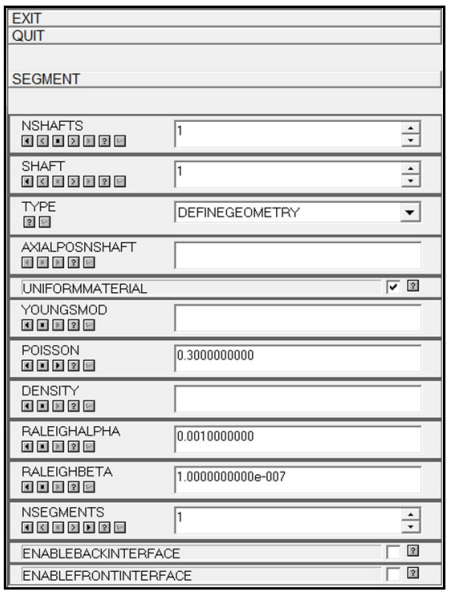

Figure E.7: View of the shaft menu in Guide.

The ENABLEBACKINTERFACE and ENABLEFRONTINTERFACE options give the user the ability to define a Fourier surface on the front of the first shaft segment or the back of the last shaft segment. If either of these options are selected, a radial and circular order must be defined. The segment menu is accessible through the button at the top of the shaft menu and is shown in Figure E.8. For a given segment, the length and outer and inner shapes must be defined. The inside or outside surface of a segment can be conical or cylindrical. The element type (ELEMTYPE)

is selected in this menu as quadratic or cubic. The number of elements in the radial (NRADIAL), axial (NAXIAL), and circular (NCIRC) direction must also be specified.

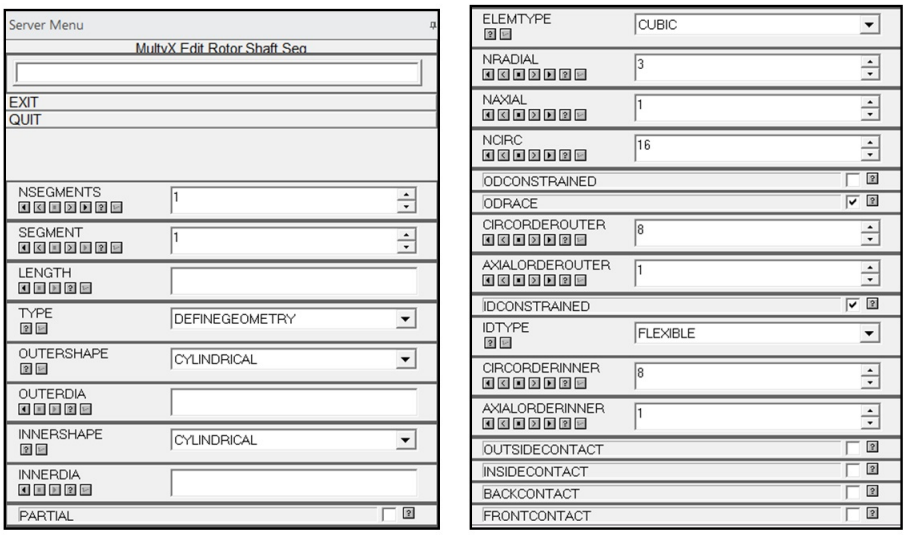

Figure E.8: View of the shaft segment menu in Guide.

At the bottom of the segment menu, constraints on the inner or outer diameter can be defined as either rigid or flexible. A rigid constraint does not allow the surface to deform. A flexible constraint allows the diameter to deform using a Fourier series in the circular direction and a polynomial series in the axial direction. A Fourier surface can be specified using the IDRACE and ODRACE commands and contact on the inner or outer diameter can be defined using the INSIDECONTACT and OUTSIDECONTACT commands respectively.

Figure E.9 shows the sun tooth menu. Gear parameters such as the number of teeth (NTEETH), and diametral pitch, pressure angle, thickness, facewidth, helix

angle, and rack tip radius are defined in either the transverse or normal plane. Gear geometry such as the outer diameter, root diameter, and inner diameter are specified in the tooth menu. Material properties and the mesh template are defined at the bottom of the menu. The number of elements in the facewidth (NFACEELEMS) and the order of coordinates (COORDORDER) and displacement interpolation (DISPLORDER) of element axnodes must also be selected.

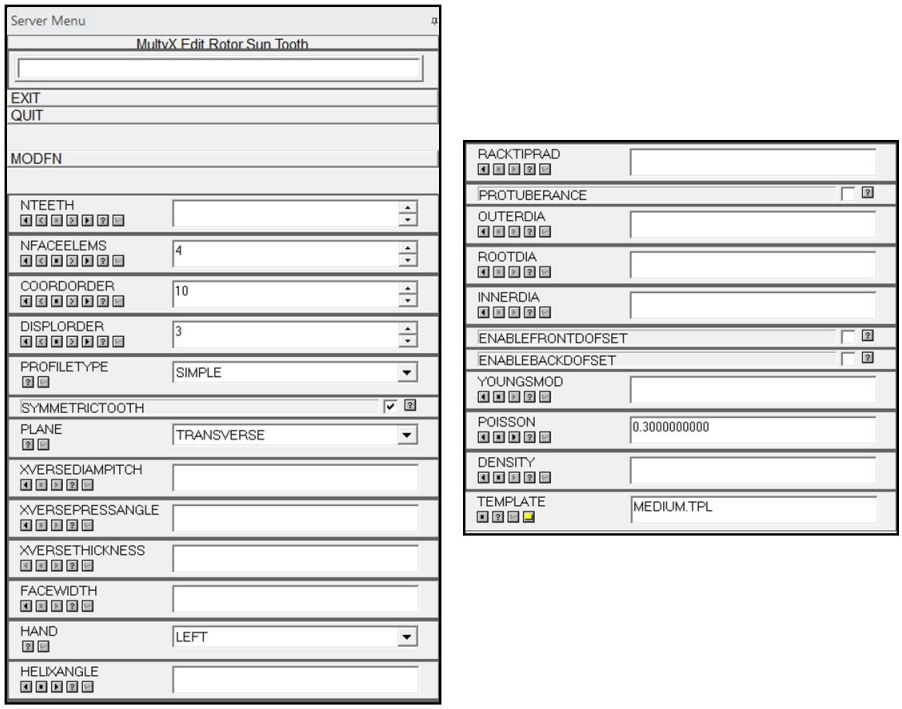

Figure E.9: View of the sun tooth menu in Guide.

The MODFN button at the top of the tooth menu leads to the tooth modification menu (shown in Figure E.10). Here, linear or quadratic root or tip modifications are defined by specifying a magnitude and starting roll angle. Lead modifications are

defined using lead crowning or by defining tabular modifications in the lead table menu.

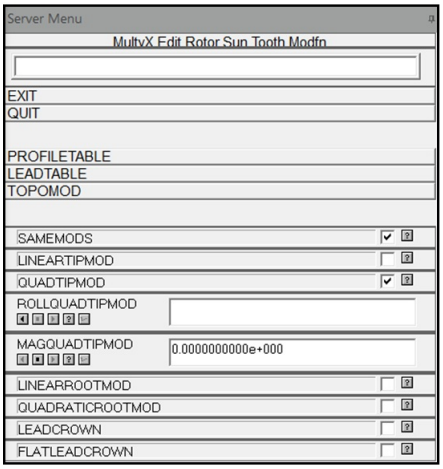

Figure E.10: View of the tooth modification menu in Guide.

Finite element carriers are defined by specifying the command (CFG) file in the carrier menu. The only user defined command is the axial shaft of the carrier measured relative to the rotor origin. From the carrier menu, the group menu and the pinion menu can be accessed. The group menu is shown in Figure E.11. The number of groups (NGROUPS), the axial position of the group (AXPOSN), and the angle of the group measured counter-clockwise about the z axis of the carrier in degrees (THETA). The purpose of this menu is to enable the user to define planet gear, pin, and bearing parameters only once and then replicate each planet (rotated about the z axis) for a given carrier.

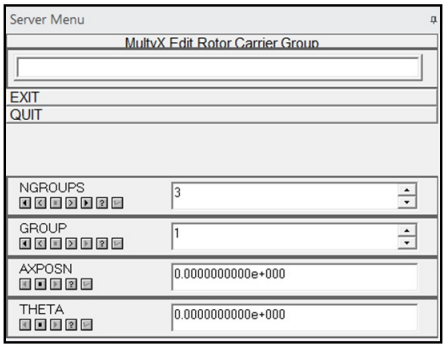

Figure E.11: View of the group menu in Guide.

Figure E.12 shows the carrier pinion menu. The type of pinion (helical or bevel) is specified here. The radial position (RADPOSN) and angular position (THETAPOSN) of the pinion must be defined. The pin and pinion shaft type is defined as simple or compound (flexpins are compound). A lumped mass (LUMPMASS), lumped polar moment of inertia (LUMPMOMINERTIA), and lumped α in the Raleigh damping model (LUMPALPHA) can also be defined at the center of each pinion. At the top of the pinion menu, there are buttons that lead to menus to define pin position error, the pin, the pinion shaft, any pressfit options, bearings, and the deck definitions.

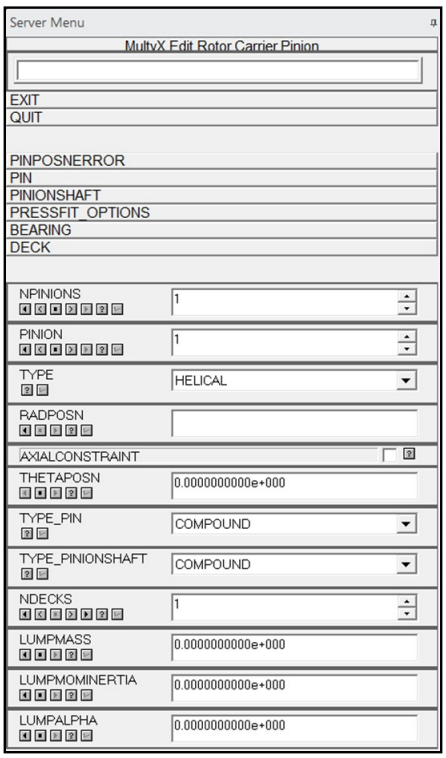

Figure E.12: View of the carrier pinion menu in Guide.

The geometry of flexpins is defined in the PIN menu following the same conventions as discussed in the shaft menu. The PINIONSHAFT menu follows the same convention as the shaft menu and is where the shaft connected to the base of the planet teeth is defined. The BEARING menu is where the connector between the outer diameter of the flexpin spindle and the inner diameter of the planet is defined (following the definitions discussed for the connector menu). The DECK menu leads to the planet tooth and rim menus.

The PINPOSNERROR menu (shown in Figure E.12) is where planet radial and angular misalignments are applied. The IGROUP command defines which planet pin

the errors are applied to (following the definition given in the GROUP menu). The MAGPINERR command governs the amount of radial misalignment applied to the planet pin. An ANGPINERR value of zero degrees infers that the planet pin misalignment is in the radial (outward) direction. A nonzero value is measured counterclockwise in degrees from the radial direction. For example, an ANGPINERR of 180 degrees would translate the planet pin in the inward direction. MISALNMT_RAD and MISALNMT_TANG refer to the angular misalignment of the pin about the radial and tangential axis of the planet. These values are measured in degrees and measured about the center of the planet gear facewidth.

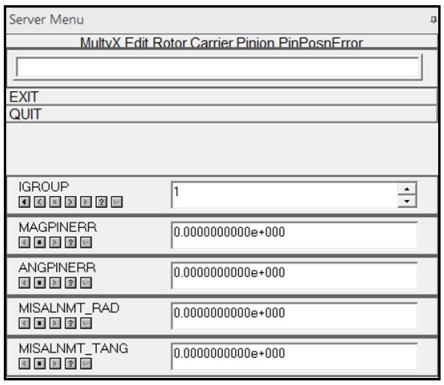

Figure E.13: View of the pin position error menu in Guide.

Bibliography

[1] Lynwander, P., 1983. *Gear Drive Systems Design and Application*. Marcel-Dekker, Inc., New York.

[2] Jain, P., 2011. *Wind Energy Engineering*. The McGraw-Hill Companies, Inc., New York.

[3] Manwell, J., McGowan, J., and Rogers, A., 2009. *Wind Energy Explained: Theory, Design, and Applications*, second ed. John Wiley and Sons Ltd., Hoboken, New Jersey.

[4] WWEA, 2011. World wind energy report 2010. Tech. rep., Bonn, Germany, Apr. World Wind Energy Association.

[5] Bansal, R., Bhatti, T., and Kothari, D., 2002. "On some of the design aspects of wind energy conversion systems". *Journal of Energy Conversion and Management,* **43**, pp. 2175–2187.

[6] Burton, T., Sharpe, D., Jenkins, N., and Bossanyi, E., 2001. *Wind Energy Handbook*. John Wiley and Sons Ltd., Hoboken, New Jersey.

[7] Dudley, D., 1994. *Handbook of Practical Gear Design*. CRC Press, Boca Raton, Florida.

[8] Valco, M., 1992. "Planetary gear train ring gear and support structure investigation". PhD thesis, Cleveland State University.

[9] Kahraman, A., Ligata, H., and Singh, A., 2010. "Influence of ring gear rim thickness on planetary gear set behavior". *Journal of Mechanical Design,* **132**, Feb., pp. 021002–1–021002–8.

[10] Singh, A., Kahraman, A., and Ligata, H., 2007. "Internal gear strains and load sharing in planetary transmissions - model and experiments". In ASME Design Engineering Technical Conferences. DETC2007-35047.

[11] Ligata, H., Kahraman, A., and Singh, A., 2008. "An experimental study of the influence of manufacturing errors on the planetary gear stresses and planet load sharing". *Journal of Mechanical Design,* **130**, Apr., pp. 041701–1–041701–9.

[12] Cheon, G.-J., and Parker, R., 2004. "Influence of manufacturing errors on the dynamic characteristics of planetary gear systems". *The Korean Society of Mechanical Engineers International Journal,* **18**(4), pp. 606–621.

[13] Cheon, G.-J., and Parker, R., 2004. "Influence of bearing stiffness on the static properties of a planetary gear system with manufacturing errors". *The Korean Society of Mechanical Engineers International Journal,* **18**(11), pp. 1978–1988.

[14] James, B., and Harris, O., 2002. "Predicting unequal planetary load sharing due to manufacturing errors and system deflections, with validation against experiments". In SAE Transmission and Driveline Systems Symposium. 2002-01-0699.

[15] Singh, A., 2005. "Application of a system level model to study the planetary load sharing behavior". *Journal of Mechanical Design,* **127**, May, pp. 469–476.

[16] Kahraman, A., and Vijayakar, S. M., 2001. "Effect of internal gear flexibility on the quasi-static behavior of a planetary gear set". *Journal of Mechanical Design,* **123**(3), Sept., pp. 408–415.

[17] Bodas, A., and Kahraman, A., 2004. "Influence of carrier and gear manufacturing errors on the static load sharing behavior of planetary gear sets". *The Japanese Society of Mechanical Engineers International Journal,* **47**(3), pp. 908–915.

[18] Parker, R. G., Agashe, V., and Vijayakar, S. M., 2000. "Dynamic response of a planetary gear system using a finite element/contact mechanics model". *Journal of Mechanical Design,* **122**(3), Sept., pp. 304–310.

[19] Poore, R., and Lettenmaier, T., 2003. Alternative design study report: Windpact advanced wind turbine drive train designs study. Tech. rep., Golden, Colorado, Aug. Subcontractor report for the National Renewable Energy Laboratory (NREL/SR-500-33196).

[20] Smolders, K., Long, H., Feng, Y., and Tavner, P., 2010. "Reliability analysis and prediction of wind turbine gearboxes". In European Wind Energy Conference.

[21] Musial, W., Butterfield, S., and McNiff, B., 2007. "Improving wind turbine gearbox reliability". In European Wind Energy Conference. NREL/CP-500-41548.

[22] DOE, 2010. Advanced wind turbine drivetrain concepts: Workshop report. Tech. rep., Broomfield, Colorado, June. Findings from the U.S. Department of Energy's Advanced Drivetrain Workshop, held June 29-30, 2010.

[23] Ragheb, A., and Ragheb, M., 2010. "Wind turbine gearbox technologies". In 1st International Nuclear and Renewable Energy Conference.

[24] Rasmussen, F., Thomsen, K., and Larsen, T., 2004. The gearbox problem revisited. Tech. rep., Roskilde, Denmark, Mar. Riso Fact Sheet AED-RB-17(EN): Riso National Laboratory.

[25] Peeters, J., and Vandepitte, P., 2004. "Flexible multibody model of a three-stage planetary gearbox in a wind turbine". In International Conference on Noise and Vibration Engineering.

[26] Helsen, J., Vanhollebeke, F., Marrant, B., Vandepitte, D., and Desmet, W., 2011. "Multibody modelling of varying complexity for modal behaviour analysis of wind turbine gearboxes". *Journal of Renewable Energy*. Article in press.

[27] Musial, W., and McNiff, B., 2000. "Wind turbine testing in the nrel dynamometer test bed". In American Wind Energy Assiociation WindPower 2000 Conference. NREL/CP-500-28411.

[28] Helsen, J., Vanhollebeke, F., De Coninck, F., Vandepitte, D., and Desmet, W., 2011. "Insights in wind turbine drive train dynamics gathered by validating advanced models on a newly developed 13.2 mw dynamically controlled test-rig". *Journal of Mechatronics,* **21**, pp. 737–752.

[29] Vijayakar, S., Gunda, R., and Abad, S., 2003. *Transmission3D User's Manual*. Advanced Numerical Solutions.

[30] Vijayakar, S., 2003. *Calyx User's Manual*. Advanced Numerical Solutions.

[31] Vijayakar, S. M., 1991. "A combined surface integral and finite-element solution for a three-dimensional contact problem". *International Journal for Numerical Methods in Engineering,* **31**(3), Mar., pp. 525–545.

[32] Vijayakar, S. M., Busby, H. R., and Houser, D. R., 1988. "Linearization of multi-body frictional contact problems". *Computers and Structures,* **29**(4), pp. 569–576.

[33] Parker, R. G., Vijayakar, S. M., and Imajo, T., 2000. "Non-linear dynamic response of a spur gear pair: Modelling and experimental comparisons". *Journal of Sound and Vibration,* **237**(3), Oct., pp. 435–455.

[34] Hau, E., 2006. *Wind Turbines: Fundamentals, Technologies, Application, Economics*, 2nd ed. Springer-Verlag, Germany.

[35] Uicker, J., Pennock, G., and Shigley, J., 2003. *Theory of Machines and Mechanisms*, 3rd ed. Oxford University Press, New York.

[36] Fox, G., and Jallet, E. Use of the Integrated Flexpin Bearing for Improving the Performance of Epicyclical Gear Systems. Technical Paper by the Timken Company.

[37] Hicks, R., 1967. Load Equalizing Means for Planetary Pinions. U.S. Patent No. 3,303,713.

[38] Hicks, R., Cunliffe, F., and Giger, U., 2004. Optimised Gearbox Design For Modern Wind Turbines. Technical Paper by Orbital2 Ltd.

[39] Hicks, R., 1969-70. "Experience with compact orbital gears in service". *Proceedings Institution of Mechanical Engineers,* **184 Pt 30**.

[40] Montestruc, A., 2011. "Influence of planet pin stiffness on load sharing in planetary gear drives". *Journal of Mechanical Design,* **133**, Jan., pp. 014501–1–014501–7.

[41] Doebelin, E., 2004. *Measurement Systems Application and Design*, 5th ed. The McGraw-Hill Companies, Inc., New York.

[42] Smurthwaite, D., and Rosinski, J., 2010. Orbital2 S3600 Planet Gear Load Sharing. Transmission Dynamics Technical Report No. TD-10-2130-01.

[43] McFadden, P., and Smith, J., 1985. "An explanation for the asymmetry of the modulation sidebands about the tooth meshing frequency in epicyclic gear vibration". *Proceedings Institution of Mechanical Engineers,* **199**(C1).

[44] Inalpolat, M., and Kahraman, A., 2009. "A theoretical and experimental investigation of modulation sidebands of planetary gear sets". *Journal of Sound and Vibration,* **323**, pp. 677–696.

[45] McNames, J., 2002. "Fourier series analysis of epicyclic gearbox vibration". *Journal of Vibration and Acoustics,* **124**, pp. 150–157. Technical Brief.

[46] Randall, R., 1982. "A new method of modeling gear faults". *Journal of Mechanical Design,* **104**, Apr, pp. 259–267.

[47] Smurthwaite, D., and Rosinski, J., 2010. Orbital2 W2000DF Planet Gear Load Sharing. Transmission Dynamics Technical Report No. TD-10-2129-01.

[48] Smurthwaite, D., and Rosinski, J., 2011. Orbital2 FC5500 Wind Turbine Gearbox - Gear Alignment and Planet Gear Load Sharing. Transmission Dynamics Technical Report No. TD-11-2157-01.

[49] ISO 6336-1, 2006. Calculation of load capacity of spur and helical gears - Part 1: Basic principles, introduction, and general influence factors.

[50] Cooley, C., Parker, R., and Vijayakar, S., 2011. "A frequency domain finite element approach for three-dimensional gear dynamics". *Journal of Vibration and Acoustics,* **133**, Aug.